

AD-A268 745

AFOSR-TR-93-0654



Final Report
Grant No. AFOSR-90-0143-B

2

January 2, 1990 - January 1, 1993

**FUNDAMENTAL CONCEPTS RELATING LOCAL ATOMIC
ARRANGEMENTS, DEFORMATION, AND FRACTURE
OF INTERMETALLIC ALLOYS**

Submitted to:

Air Force Office of Scientific Research
Building 410
Bolling Air Force Base
Washington, DC 20332

Attention:

Dr. Alan H. Rosenstein/NE
Directorate of Chemistry and Materials Science

Submitted by:

John A. Wert
Professor

This document has been approved
for public release and sale; its
distribution is unlimited.

SEAS Report No. UVA/525725/MSE93/101
June 1993

DEPARTMENT OF MATERIALS SCIENCE AND ENGINEERING

SCHOOL OF
ENGINEERING 
& APPLIED SCIENCE

University of Virginia
Thornton Hall
Charlottesville, VA 22903

93-20275



171P8

Approved for public release;
distribution unlimited.

UNIVERSITY OF VIRGINIA
School of Engineering and Applied Science

The University of Virginia's School of Engineering and Applied Science has an undergraduate enrollment of approximately 1,500 students with a graduate enrollment of approximately 600. There are 160 faculty members, a majority of whom conduct research in addition to teaching.

Research is a vital part of the educational program and interests parallel academic specialties. These range from the classical engineering disciplines of Chemical, Civil, Electrical, and Mechanical and Aerospace to newer, more specialized fields of Applied Mechanics, Biomedical Engineering, Systems Engineering, Materials Science, Nuclear Engineering and Engineering Physics, Applied Mathematics and Computer Science. Within these disciplines there are well equipped laboratories for conducting highly specialized research. All departments offer the doctorate; Biomedical and Materials Science grant only graduate degrees. In addition, courses in the humanities are offered within the School.

The University of Virginia (which includes approximately 2,000 faculty and a total of full-time student enrollment of about 17,000), also offers professional degrees under the schools of Architecture, Law, Medicine, Nursing, Commerce, Business Administration, and Education. In addition, the College of Arts and Sciences houses departments of Mathematics, Physics, Chemistry and others relevant to the engineering research program. The School of Engineering and Applied Science is an integral part of this University community which provides opportunities for interdisciplinary work in pursuit of the basic goals of education, research, and public service.

Final Report
Grant No. AFOSR-90-0143-B

January 2, 1990 - January 1, 1993

FUNDAMENTAL CONCEPTS RELATING LOCAL ATOMIC
ARRANGEMENTS, DEFORMATION, AND FRACTURE
OF INTERMETALLIC ALLOYS

Submitted to:

Air Force Office of Scientific Research
Building 410
Bolling Air Force Base
Washington, DC 20332

Attention:

Dr. Alan H. Rosenstein/NE
Directorate of Chemistry and Materials Science

Submitted by:

John A. Wert
Professor

Department of Materials Science and Engineering
School of Engineering and Applied Science
University of Virginia
Thornton Hall
Charlottesville, VA 22903-2442

Accession For	
NTIS CRA&I	<input checked="" type="checkbox"/>
DTIC TAB	<input type="checkbox"/>
Unannounced Justification	<input type="checkbox"/>
By	
Distribution /	
Availability Codes	
Dist	Avail and/or Special
A-1	

DTIC QUALITY INSPECTED 3

REPORT DOCUMENTATION PAGE			Form Approved OMB No. 0704-0188	
<small>Public reporting burden for this collection of information is estimated to average 1 hour per response, including the time for reviewing instructions, searching existing data sources, gathering and maintaining the data needed, and completing and reviewing the collection of information. Send comments regarding this burden estimate or any other aspect of this collection of information, including suggestions for reducing this burden, to Washington Headquarters Services, Directorate for Information Operations and Reports, 1215 Jefferson Davis Highway, Suite 1204, Arlington, VA 22202-4302, and to the Office of Management and Budget, Paperwork Reduction Project (0704-0188), Washington, DC 20503.</small>				
1. AGENCY USE ONLY (Leave blank)		2. REPORT DATE June 1993		3. REPORT TYPE AND DATES COVERED Final Report 1/2/90 - 1/1/93
4. TITLE AND SUBTITLE Fundamental Concepts Relating Local Atomic Arrangements, Deformation, and Fracture of Intermetallic Alloys			5. FUNDING NUMBERS 61125 AFOSR-90-0143-B 2304/171	
6. AUTHOR(S) J. A. Wert, Professor				
7. PERFORMING ORGANIZATION NAME(S) AND ADDRESS(ES) Department of Materials Science and Engineering School of Engineering and Applied Science University of Virginia, Thornton Hall Charlottesville, VA 22903-2442			8. PERFORMING ORGANIZATION REPORT NUMBER UVA/525725/MSE93/101	
9. SPONSORING/MONITORING AGENCY NAME(S) AND ADDRESS(ES) Air Force Office of Scientific Research Building 410 Bolling Air Force Base Washington, DC 20332			10. SPONSORING/MONITORING AGENCY REPORT NUMBER AFOSR-90-0143-B	
11. SUPPLEMENTARY NOTES				
12a. DISTRIBUTION/AVAILABILITY STATEMENT Unlimited Distribution			12b. DISTRIBUTION CODE	
<p>This final contract report describes research activities on two topics of fundamental importance for application of intermetallic alloys as elevated temperature engineering materials: brittle fracture and creep resistance. On the topic of brittle fracture, the process of crack tip plasticity has been investigated by extending the Rice-Thomson model to treat the case of crack tip emission of dissociated superlattice dislocations that commonly occur in intermetallic alloys. The model shows that superlattice dislocation emission from crack tips can be inhibited in intermetallic alloys, and predicts the occurrence of cleavage fracture in particular intermetallic alloys. The fracture mode predictions can be compared with experimentally observed fracture modes; such comparisons for intermetallic alloys with the L1₂ and B2 crystal structures show that the model predictions match the experimental observations for every intermetallic alloy where sufficient data are available to perform the model calculations (about 25 alloys in all). A novel result of the dislocation emission modeling work is the finding that the antiphase boundary energy plays a central role in determining whether a particular intermetallic alloy will exhibit cleavage fracture or not. A second major research topic is creep of TiAl/Ti₃Al alloys with lamellar microstructures. Creep test results revealed that the two-phase TiAl/Ti₃Al constituent phases, over the stress and temperature ranges investigated. Additionally, the TiAl/Ti₃Al lamellar alloy exhibits very little primary creep strain, a desirable characteristic for engineering applications. Using the results of creep experiments and detailed observations of the creep behavior of each phase in the two-phase alloy, a constitutive model of creep of materials with a lamellar microstructures have been formulated. The creep model predictions compare favorable with experimentally observed creep rates for the TiAl/Ti₃Al lamellar alloy.</p>				
14. SUBJECT TERMS Intermetallic Alloys, TiAl, Ti ₃ Al, Fracture, Creep			15. NUMBER OF PAGES 165	
			16. PRICE CODE	
17. SECURITY CLASSIFICATION OF REPORT Unclassified	18. SECURITY CLASSIFICATION OF THIS PAGE Unclassified	19. SECURITY CLASSIFICATION OF ABSTRACT Unclassified	20. LIMITATION OF ABSTRACT Unlimited	

Table Of Contents

1. Introduction	2
1.1 Fracture of Intermetallic Alloys	3
1.2 Creep of Intermetallic Alloys	10
1.3 Organization of Report	20
1.4 References for Introduction	20
2. Fracture of Intermetallic Alloys	25
2.1 Effect of Dislocation Dissociation on Crack Tip Plasticity in L1 ₂ Intermetallic Alloys	26
2.2 Modeling of Crack Tip Dislocation Emission in B2 Intermetallic Alloys	51
2.3 The Effect of Dislocation Dissociation on Crack Tip Plasticity in L1 ₂ and B2 Intermetallic Alloys	71
2.4 Experimental Assessment of Crack Tip Dislocation Emission Models for an Al ₆₇ Cr ₈ Ti ₂₅ Intermetallic Alloy	83
3. Creep of TiAl/Ti ₃ Al Alloys with Lamellar Microstructures	117
3.1 Creep Deformation of a Two-Phase TiAl/Ti ₃ Al Lamellar Alloy and the Individual TiAl and Ti ₃ Al Constituent Phases	119
3.2 Modeling the Creep Deformation of a Two-Phase TiAl/Ti ₃ Al Lamellar Alloy	130
4. Publications and Presentations	165

Abstract

This final contract report describes research activities on two topics of fundamental importance for application of intermetallic alloys as elevated temperature engineering materials: brittle fracture and creep resistance. On the topic of brittle fracture, the process of crack tip plasticity has been investigated by extending the Rice-Thomson model to treat the case of crack tip emission of dissociated superlattice dislocations that commonly occur in intermetallic alloys. The model shows that superlattice dislocation emission from crack tips can be inhibited in intermetallic alloys, and predicts the occurrence of cleavage fracture in particular intermetallic alloys. The fracture mode predictions can be compared with experimentally observed fracture modes; such comparisons for intermetallic alloys with the $L1_2$ and B2 crystal structures show that the model predictions match the experimental observations for every intermetallic alloy where sufficient data are available to perform the model calculations (about 25 alloys in all). A novel result of the dislocation emission modeling work is the finding that the antiphase boundary energy plays a central role in determining whether a particular intermetallic alloy will exhibit cleavage fracture or not. A second major research topic is creep of TiAl/Ti₃Al alloys with lamellar microstructures. Creep test results revealed that the two-phase TiAl/Ti₃Al lamellar alloy has substantially lower creep rates than the TiAl and Ti₃Al constituent phases, over the stress and temperature ranges investigated. Additionally, the TiAl/Ti₃Al lamellar alloy exhibits very little primary creep strain, a desirable characteristic for engineering applications. Using the results of creep experiments and detailed observations of the creep behavior of each phase in the two-phase alloy, a constitutive model of creep of materials with a lamellar microstructures has been formulated. The creep model predictions compare favorably with experimentally observed creep rates for the TiAl/Ti₃Al lamellar alloy.

1. Introduction

The idea that ordered intermetallic alloys could be developed as engineering materials for elevated temperature applications is not new. The atomic bonding characteristics that favor formation of an ordered crystal structure often produce an alloy with a considerably higher melting temperature than the pure metal components, suggesting improved elevated temperature strength and creep resistance. In the 1950's and early 1960's, a substantial research effort was devoted to synthesis of ordered intermetallic alloys in an attempt to develop new engineering materials for elevated temperature applications. These research efforts greatly expanded our fundamental knowledge of ordered intermetallic alloys. Unfortunately, the expansion of fundamental knowledge did not lead to successful development of ordered intermetallic alloys as engineering materials. This is primarily because the brittle character of most ordered intermetallic alloys could not be remedied. Thus, interest in ordered intermetallic alloys as engineering materials waned in the latter part of the 1960's. However, interest in the superconducting properties of ordered intermetallic alloys continued and there is now a robust market for intermetallic superconducting magnets in magnetic resonance imaging equipment for medical applications.

The potential benefits of successful development of ordered intermetallic alloys as elevated temperature materials for aerospace applications prompted a modest number of investigators to continue research on these materials, leading to several notable discoveries during the 1970's. In particular, Lipsitt and coworkers [1-3] showed that the brittle nature of TiAl and Ti₃Al could be ameliorated, and researchers at Oak Ridge National Laboratory and in Japan discovered composition variations that permitted the normally brittle ordered intermetallic alloys Co₃V and Ni₃Al to exhibit extensive ductility [4-6]. These discoveries, along with a renewed interest in supersonic and hypersonic flight vehicles, led to the current surge of research on ordered intermetallic alloys as elevated-temperature engineering materials.

Over the past 15 years, tremendous resources have been focused on development of ordered intermetallic alloys as elevated-temperature engineering materials. Many avenues of research have been pursued and our knowledge of the properties and characteristics of ordered intermetallic alloys has greatly expanded. Despite these efforts, there remain several fundamental barriers to engineering application of ordered intermetallic alloys as elevated-temperature materials. The

research described in this final contract report addresses two of the key issues: brittle fracture and creep resistance.

1.1 Fracture of Intermetallic Alloys

The brittleness of ordered intermetallic alloys was a primary cause for declining interest in these materials in the early 1960's and it remains today as an obstacle to successful development of ordered intermetallic alloys as engineering materials. During the present cycle of research and development of ordered intermetallic alloys, a greater understanding of the causes of brittle fracture is emerging. As described previously, it is now known that brittle fracture can be remedied in some ordered intermetallic alloys. The objectives of Section 1.1 of this report are to briefly summarize the important causes of brittle fracture in ordered intermetallic alloys and to describe some of the methods that have been devised to circumvent brittle fracture in these materials. Since this is one of the topics of critical importance to development of ordered intermetallic alloys as engineering materials, it has been extensively reviewed by previous authors [7-14].

1.1.1 High Critical Resolved Shear Stress

In crystals characterized by strong covalent bonding the shear stress required for slip can approach the theoretical value of about $G/10$, where G is the shear modulus. In such materials, slip cannot readily occur to relieve stress concentrations at internal or external defects or at grain boundaries. During loading, cracks initiate at stress concentration sites and propagate rapidly in a brittle manner. The only general method known for suppressing brittle fracture of materials with high CRSS is reducing the CRSS. In particle-strengthened alloys, for example, it is possible to reduce the strengthening contribution from the particle dispersion by decreasing the volume fraction or by coarsening the particles [15,16]. In materials such as ceramics where the high CRSS is an intrinsic characteristic of the material, brittle fracture difficult to avoid. However, the CRSS is below $G/100$ in most ordered intermetallic alloys, suggesting that high CRSS is not the prevalent cause of brittle fracture in these materials.

One method for suppressing brittle fracture in materials with high CRSS is superposition of hydrostatic compressive stress on the shear stress that produces plastic deformation [17-19]. This method of suppressing brittle fracture can be used in

the laboratory for characterizing the plastic flow properties of brittle materials, and it can be used in materials processing operations (such as hydrostatic extrusion) to prevent brittle fracture during processing. A recent publication has described plastic flow of a normally-brittle ordered intermetallic alloy through the use of superposed hydrostatic pressure [20].

Transformation toughening has been used to increase the toughness of some ceramic materials with high CRSS. Metastable phases introduced during processing undergo martensitic transformations in the stress field near a crack tip, thereby reducing the stress concentration at the crack tip [21,22]. Models of the transformation toughening mechanism suggest that the increased toughness derives from the volume expansion associated with some martensitic transformations, rather than from the shear components of the transformation strain [22]. Martensitic transformations occur in some ordered intermetallic alloys but there have been no reports of transformation toughening in these materials. A practical difficulty that limits use of this toughening mechanism for materials intended for elevated temperature service is that the toughening mechanism only operates over a restricted temperature range where the transforming phase exists in metastable equilibrium.

1.1.2 Insufficient Number of Slip Systems

As originally proposed by von Mises [23] and subsequently discussed by other investigators [24-30], the compatibility requirement for deformation of a polycrystalline aggregate requires operation of 5 independent slip systems (deformation modes) in each grain. This ensures that each grain can undergo an arbitrary shape change with constant volume, thus maintaining compatibility with neighboring grains. If the compatibility requirement is not met, grain boundary separation occurs at small plastic strains, usually leading to intergranular fracture with very limited macroscopic ductility.

The most straightforward solution to the compatibility problem is to change the crystal structure of an ordered intermetallic alloy to a crystal structure with more equivalent slip systems. This can be done by alloying, as described by Liu for $(\text{Fe,Co,Ni})_3\text{V}$ alloys [4,5,31]. In this case, partial substitution of Fe for Ni in Ni_3V (tetragonal, D_{022}) or for Co in Co_3V (six layer hexagonal ordered crystal structure) changes the stable crystal structure to L_{12} , a higher-symmetry crystal structure with more independent slip systems. The increased tensile elongation exhibited by

(Fe,Co,Ni)₃V alloys with the L1₂ crystal structure is attributed to the increased number of independent slip systems. The main limitation to application of this method is that substitution of new elements in most ordered intermetallic alloys produces new, ternary or multinary phases with lower-symmetry crystal structures, which only exacerbates the compatibility problem. However, in a limited number of cases, crystal structure changes can solve the compatibility problem and can provide the desired improvement in tensile elongation.

An alternate method of avoiding brittle fracture is to change the operative slip systems by substituting new elements in ordered intermetallic alloys. An example of this approach is addition of Nb to Ti₃Al. Room temperature plastic deformation of Ti₃Al is associated with glide of APB-coupled pairs of $1/6\langle 11\bar{2}0 \rangle$ superlattice partial dislocations on {1100}, which provide only 3 independent slip systems [32,33]. Limited activity is also observed on other slip systems at room temperature, but the CRSS for these alternate systems is thought to be high and their contribution to the overall strain is small. Increasing the deformation temperature to 923 K allows more extensive slip on alternate slip systems; for example, glide of fault-coupled pairs with $b = 1/6\langle 11\bar{2}6 \rangle$ on {11 $\bar{2}$ 1} has been reported [32,33]. The increased ductility of Ti₃Al at 923 K is thought to be associated with the increased number of independent slip systems. Additions of Nb have been shown to promote operation of several additional slip systems at room temperature and the increased room temperature ductility afforded by Nb additions to Ti₃Al has been attributed to this factor [33].

A similar situation occurs in NiAl where the brittle behavior of NiAl polycrystals at room temperature has been attributed to an insufficient number of active slip systems [34-37]. Unlike other ordered intermetallic alloys that have the B2 crystal structure (e.g., CuZn and AgMg), the active slip system in NiAl is $\langle 100 \rangle \{011\}$ which provides only 3 independent slip systems [34,35,37,38]. Alloying with Cr and Mn has been found to change the slip vector from $\langle 100 \rangle$ to $\langle 111 \rangle$ but room temperature tensile elongation was not significantly increased by this change [3], suggesting that other factors contribute to brittle fracture of NiAl. Many investigators have speculated about the mechanism of brittle fracture in NiAl alloys modified to promote $\langle 111 \rangle$ slip, but limited evidence is available to support the proposed mechanisms. This topic was examined within the scope of the present research contract, as discussed in Section 2.2. Energy calculations described in Section 2.2 show that emission of $\langle 111 \rangle$

dislocations from crack tips in NiAl is inhibited, with the result that brittle fracture occurs instead of plastic crack blunting.

A different approach to the problem of brittle fracture of NiAl has been described by Schulson and coworkers [39-41] who reduced the grain size of NiAl by thermomechanical processing. The brittle-to-ductile transition temperature is reduced for grain sizes smaller than approximately 20 μm . Hahn and Vedula [42] reported significant room temperature tensile elongation for stoichiometric NiAl with a grain size near 15 μm and a low level of O and C impurities. However, alloys deviating slightly from the stoichiometric composition exhibited brittle intergranular fracture at room temperature with little tensile elongation. The mechanism providing enhanced tensile elongation for the stoichiometric alloy has not yet been reported.

1.1.3 Intergranular Fracture

Much of our detailed knowledge of intergranular fracture in ordered intermetallic alloys is the result of very intensive investigations of Ni_3Al . Single crystals of Ni_3Al [43] and $\text{Ni}_3(\text{Al},\text{Ti})$ [44] are ductile at low temperatures in all orientations, but brittle intergranular fracture is observed in polycrystalline Ni_3Al (for example, Refs. [45,46]). Many experimental investigations have sought to identify the cause of brittle intergranular fracture of Ni_3Al , and to discover methods for altering this undesirable characteristic.

In disordered alloys, intergranular fracture is often associated with impurity segregation at grain boundaries. Application of surface microchemical analysis methods to Ni_3Al fracture surfaces has shown that no segregant is present at grain boundaries in high-purity, polycrystalline Ni_3Al which exhibits intergranular fracture [45-47]. Grain boundary misorientation, which is determined by the relative lattice orientations of the adjoining grains, has been shown to have an effect on intergranular fracture of Ni_3Al [48]. Low angle and Σ boundaries were found to be resistant to intergranular fracture whereas higher Σ boundaries were found to offer less resistance. Stoichiometric variations and alloying to reduce the ordering temperature (T_o) below the melting temperature (T_m) allowed Cahn and coworkers [49,50] to investigate the effect of antiphase domain (APD) structures on intergranular fracture of Ni_3Al . They reported that formation of an APD structure in sequentially-ordered Ni_3Al alloys is associated with enhanced tensile ductility, but the suggestion that the APD structure is

the cause of improved resistance to intergranular fracture has not yet gained wide acceptance.

The discovery [6] that small additions of boron to Ni_3Al change the fracture mechanism from completely intergranular to predominantly transgranular, and increase room temperature tensile elongation from 0 to several tens of percent, is largely responsible for the widespread interest in Ni_3Al over the last decade. The boron effect is due to segregation of boron to grain boundaries in Ni_3Al where it acts to change the fracture mode, thereby remarkably improving tensile ductility [45,51]. The beneficial effect of boron is pronounced in hypostoichiometric Ni_3Al compositions, but boron has essentially no effect in hyperstoichiometric compositions [45,51]. These observations are consistent with measurements of boron segregation to grain boundaries which have shown that the B/Ni ratio at grain boundaries decreases with increasing Al content [45,51]. The effect of alloy stoichiometry may be associated with constitutional defects in hyperstoichiometric Ni_3Al which prevent boron segregation to grain boundaries.

Several explanations for the boron effect in Ni_3Al have been advanced. The idea that boron increases grain boundary cohesion has been proposed by Liu and others [11-13,45,50,52-54]. The increase in boundary cohesion is thought to be an electronic effect in which boron acts as an electron donor, altering the character of bonding in the vicinity of the grain boundaries. An alternate explanation holds that the improved tensile ductility imparted by boron additions arises from formation of a disordered region at the grain boundary [55,56], analogous to the glassy grain boundary phases found in some ceramic materials. If this explanation is correct, one would expect the disordered grain boundary film to have a deleterious effect on strength at elevated temperatures, much as in the case of the glassy phase in ceramic materials [57,58]. However, experimental observations show that boron additions to Ni_3Al increase strength at elevated temperatures [59], contrary to the observations for glassy phases in ceramics. Finally, boron has been suggested to ease slip transmission across grain boundaries [60,61]. This explanation could be accommodated within the framework of either of the mechanisms described previously.

The remarkable effect of small boron additions to Ni_3Al on tensile elongation has led to evaluation of a wide variety of other additions to Ni_3Al , as recently summarized by Liu [12] and by Stoloff [7]. No other element has been found which produces an

effect of the same magnitude as boron, although modest improvements in ductility have been obtained with additions of Be, Mn, Fe, Cr, and Hf.

Since the original discovery of the boron effect in Ni_3Al , boron has been added to a vast number of other ordered intermetallic alloys, with very limited success. Boron additions have been found to improve the tensile elongation of Ni_3Ga , Ni_3Si [11,54,62] and $\text{Ni}_3(\text{Si,Ti})$ [63], all of which have the same crystal structure as Ni_3Al and fracture intergranularly without boron additions. Although the boron effect in Ni_3Ga , Ni_3Si and $\text{Ni}_3(\text{Si,Ti})$ has not been as exhaustively studied as in Ni_3Al , similarities among these alloys suggest that the boron effect may be produced by the same mechanism in all 4 cases. The only other ordered intermetallic alloy in which boron additions have been found to appreciably change the brittle fracture behavior is FeAl . Crimp and Vedula [64] reported a change in fracture mode from intergranular to transgranular with boron additions to FeAl . However, Baker and Munroe [14] suggested the effect observed by Crimp and Vedula [64] may have been associated with variations in the Al content of the FeAl alloys in which the effect was observed. The observations needed to clarify the effect of boron in FeAl have not been reported.

1.1.4 Activation Barrier for Crack Tip Plasticity

Rice and Thomson [65] first proposed that plastic crack blunting could be inhibited, even in materials with low CRSS, due to an activation barrier for emission of dislocations from the free surface at a crack tip. They considered the blunting process to occur by emission of dislocation half loops from crack tips. By considering the energy of the dislocation half loop as a function of loop radius, they found that some materials exhibit an activation barrier to dislocation emission, while others exhibit spontaneous dislocation emission (i.e., no activation barrier). By considering average values of geometrical parameters, Rice and Thomson were able to show that a barrier to dislocation emission is present if the parameter Gb/γ_f is greater than about 10, where G is the shear modulus, b is the slip vector and γ_f is the true fracture surface energy. The analysis has been applied to a wide variety of materials [65,66] and excellent correlation has been found between the parameter Gb/γ_f and fracture mode. Cleavage fracture is usually observed for materials with values of $Gb/\gamma_f > 10$, whereas ductile fracture is normally found for materials with $Gb/\gamma_f < 10$. Since this mechanism of brittle fracture is independent of CRSS, it is able to account for cleavage fracture in materials with low or modest CRSS which are expected to be ductile from all other

considerations. Numerous refinements of the original model have been published [67-73].

This brittle fracture criterion has only recently been applied to ordered intermetallic alloys [74]. However, simple consideration of the form of the critical parameter, Gb/γ_f , suggests that this mechanism of brittle fracture may be of importance for some ordered intermetallic alloys. The shear modulus of intermetallic phases is often somewhat higher than the shear moduli of the constituent elements. In addition, the slip vector associated with superlattice dislocations is larger than the slip vector of a disordered crystal. Thus, the factor (Gb) can be significantly increased by formation of an ordered phase. While experimental values have not been reported for the true fracture surface energy or the free surface energy of any ordered intermetallic alloy, empirical estimates for a variety of ordered intermetallic alloys [74] and atomistic calculations for Ni_3Al [75] suggest that the factor γ_f is not increased to the same extent as the factor (Gb).

Turner, Powers and Wert [74] performed an approximate analysis of the parameter Gb/γ_f for ordered intermetallic alloys with the $L1_2$ crystal structure, and compared model predictions with the observed fracture mode. The values of Gb/γ_f were calculated using the slip vector of the superlattice partial dislocations determined from the appropriate dislocation dissociation schemes (this is equivalent to assuming a fault energy of 0). Correlation between the criterion proposed by Rice and Thomson and the observed fracture mode is only fair, suggesting that the approximations involved for dissociated superlattice dislocations are inappropriate. More sophisticated crack tip dislocation emission calculations that properly account for the dissociated superlattice dislocation configurations observed $L1_2$ and B2 ordered intermetallic alloys have been performed within the scope of the present contract. The revised model predictions are in excellent accord with experimental results in all cases where sufficient experimental data are available to apply the model. Details of these calculations are contained in Sections 2.1 and 2.2 of the present report.

1.2 Creep

Considering that the primary, long-range goal of much current research on the topic of ordered intermetallic alloys for aerospace applications is to produce alloys that are strong at elevated temperatures, creep data are remarkably limited. Fortunately, several of the investigations of creep of ordered intermetallic alloys that have been reported are systematic and provide useful insight.

1.2.1 Creep Mechanisms in Ordered Intermetallic Alloys

The primary mechanisms of creep in all crystalline materials can be categorized as diffusional mechanisms and dislocation mechanisms [76]. Diffusional mechanisms rely on mass transport by diffusion to produce plastic strain and are characterized by constitutive relationships of the form [76]:

$$\dot{\epsilon}_{HN} = 14 \left(\frac{\Omega D_L}{k_B T d^2} \right) \sigma \quad (1)$$

$$\dot{\epsilon}_C = 14\pi \left(\frac{\Omega \delta D_B}{k_B T d^3} \right) \sigma \quad (2)$$

where $\dot{\epsilon}_{HN}$ is the uniaxial strain rate due to the Herring-Nabarro creep mechanism, $\dot{\epsilon}_C$ is the uniaxial strain rate due to the Coble creep mechanism, Ω is the atomic volume, d is the grain size, δ is the grain boundary width, D_L is the lattice diffusivity, D_B is the grain boundary diffusivity and σ is the uniaxial tensile or compressive stress. When mass transport occurs predominately through the grains (Herring-Nabarro creep), the lattice diffusivity (D_L) appears in the constitutive equation and the grain size exponent is 2. When mass transport occurs primarily along grain boundaries (Coble creep), the grain boundary diffusivity (D_B) appears in the constitutive equation in combination with the grain boundary thickness and the grain size exponent is 3. The values of the numerical constants depend on the grain geometry selected for modeling and on other factors; the values shown in Equations (1) and (2) are those proposed by Raj and Ashby [77].

The constitutive relationships for creep by dislocation glide/climb mechanisms (often referred-to as "power law creep mechanisms") are similar to Equations (1) and (2), but the grain size dependence is absent and the stress exponent is no longer 1. While several mechanisms of power-law creep are known, glide/climb mechanisms are most commonly observed. The constitutive relationships appropriate to these mechanisms are [76]:

$$\dot{\epsilon}_{\text{HTD}} = \frac{AD_L G b}{k_B T} \left| \frac{\sigma}{G} \right|^n \quad (3)$$

$$\dot{\epsilon}_{\text{LTD}} = \frac{10Aa_c D_c G}{bk_B T} \left| \frac{\sigma}{G} \right|^{n+2} \quad (4)$$

where $\dot{\epsilon}_{\text{HT}}$ is the uniaxial strain rate due to the high-temperature dislocation climb/glide mechanism, $\dot{\epsilon}_{\text{LTD}}$ is the uniaxial strain rate due to the low- temperature dislocation glide/climb mechanism, A is the power law creep constant, G is the shear modulus, D_c is the dislocation core diffusivity, a_c is the cross-sectional area of the dislocation core region where fast diffusion occurs, and n is the power-law creep stress exponent.

For the purpose of analyzing experimental creep data, the Dorn equation is often used:

$$\dot{\epsilon} = \frac{A_d D_{\text{eff}} G b}{k_B T} \left| \frac{\sigma}{G} \right|^n \quad (5)$$

where A_d is a dimensionless constant, n is the stress exponent, and D_{eff} is the effective diffusion coefficient. Experimentally, it is found that when dislocation climb is the rate-controlling creep process and glide is comparatively rapid, the stress exponent is typically 4 or 5 and D_{eff} is the diffusivity associated with dislocation climb. In this case, the Dorn equation is equivalent to the constitutive equations for power law creep, Equations (3) and (4). Alternatively, when viscous glide of dislocations is the rate controlling creep process, the stress exponent is smaller (usually near 3) and the

activation energy in the D_{eff} term is that associated with thermally-activated dislocation glide.

The mechanisms listed above are exhibited by all crystalline materials during slow strain rate deformation at elevated temperatures. Additional creep mechanisms that occur in some circumstances include grain boundary sliding, dislocation climb (Harper-Dorn creep) and power-law breakdown [76]. Models of each of these processes have been developed and constitutive relationships have been formulated. The constitutive relationships all have the general form of the Dorn equation in which the values of A_d , n and D_{eff} depend on the details of the mechanism. While these additional mechanisms are important in some situations, the diffusional and dislocation glide/climb mechanisms described previously are frequently of greatest importance.

Considering creep of ordered intermetallic alloys, it is useful to establish whether any new creep mechanisms are introduced as a consequence of the ordered crystal structure or other characteristics of these materials. Sauthoff and coworkers [78-81] have reported results of creep experiments on a series of B2 (Ni,Fe)Al alloys; some of their experimental data for creep at 1173 K are reproduced in Figure 1. The creep data and the associated microstructural observations show that the (Fe,Ni)Al alloys deform by dislocation creep mechanisms for the range of test parameters represented in Figure 1. Sauthoff and coworkers [78] have shown that the greatest creep resistance for (Fe,Ni)Al of the stoichiometric composition is found for $(\text{Ni}_{0.8}\text{Fe}_{0.2})\text{Al}$, which corresponds with the minimum diffusivity calculated from results reported by Moyer and Doyananda [82]. The stress exponents obtained from the experimental results are between 4 and 4.5 for Ni-rich alloys, and are between 3 and 3.6 for Fe-rich alloys, suggesting a shift from climb control to viscous glide control as the Fe concentration increases. At 1023 K, experimental creep data for the $(\text{Ni}_{0.8}\text{Fe}_{0.2})\text{Al}$ composition show that the stress exponent changes to 1 at low stresses, indicative of a change to a diffusional creep mechanism. Sauthoff and coworkers [78] also observed grain boundary sliding in the $(\text{Ni}_{0.8}\text{Fe}_{0.2})\text{Al}$ alloy.

The creep characteristics of Ni_3Al have been extensively investigated and have been recently summarized by Stoloff [7]. Dislocation creep mechanisms have been deduced from the stress exponent and activation energy values for an $\text{Ni}_{67}\text{Al}_{23}\text{Fe}_{10}$ alloy and a boron-doped $\text{Ni}_{76}\text{Al}_{23.5}\text{Hf}_{0.5}$ alloy tested at relatively high stresses in the temperature range 873 to 1203 K [83,84]. At lower stresses [84] and in a similar

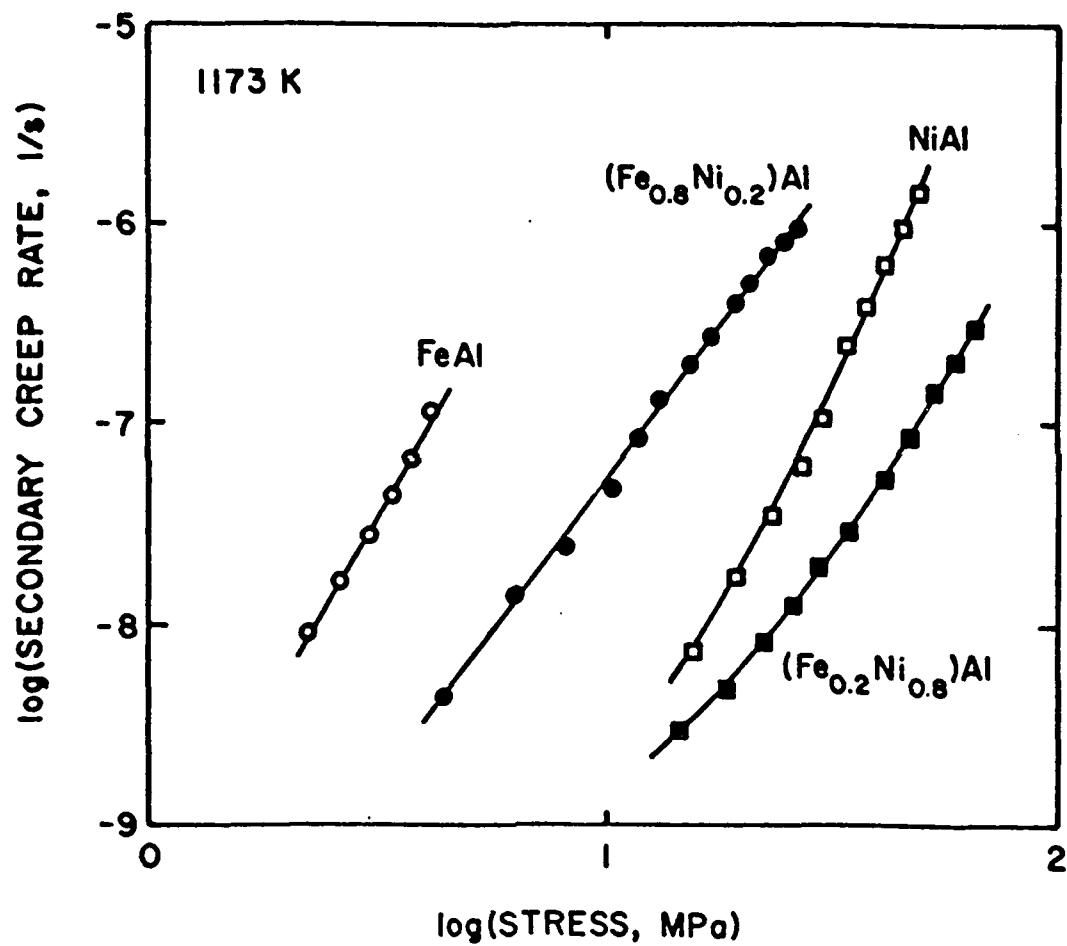


Figure 1. Strain rate as a function of applied stress for several (Fe,Ni)Al alloys crept at 1173 K. (After Jung et al. [80])

Ni-Al-Hf-B alloy processed to obtain finer grain size, the stress exponent and activation energy characteristic of diffusional creep mechanisms were observed [85].

As noted by Stoloff [7], the creep resistance of unalloyed Ni_3Al is unexpectedly low. The creep resistance is highest for the stoichiometric composition, an effect attributed to constitutional defects increasing the diffusion rate for off-stoichiometric compositions [86]. A wide variety of solutes have been added to Ni_3Al in attempts to ameliorate the low creep resistance and some success has been achieved. Additions of Hf and Cr + Zr were effective in increasing the creep resistance over a broad temperature range [87,88]; Ta increases creep resistance at 1255 K but lowers it at temperatures below 1144 K [89]. These effects have been observed by various investigators using alloys processed by different methods and undoubtedly containing different impurities. In the absence of systematic investigations over broad ranges of stress, temperature and material parameters, it is difficult to formulate general conclusions.

Creep data have been reported for a variety of other intermetallic alloys including TiAl [90], Ti_3Al [91], Ni_2AlTi [92], CoAl [80], and Al_3Nb [80]. Stress exponents in the range of 4-6 have been observed in nearly all of these studies and the activation energy values for creep in several of these ordered intermetallic alloys are somewhat higher than values found for creep of conventional alloys. Unfortunately, the broad lack of diffusion and dislocation data for ordered intermetallic alloys makes identification of the operative creep mechanisms difficult. Little systematic progress is being made toward resolving this problem: many studies of creep properties produce only engineering creep data (i.e., rupture time as a function of stress and temperature) and few investigations of diffusion are being conducted. The lack of systematic creep measurements provided a driving force for a portion of the present investigation in which the creep properties of a TiAl/ Ti_3Al alloy with a lamellar microstructure are investigated, along with the creep properties of the TiAl and Ti_3Al constituent phases. The results and analyses on this topic are contained in Sections 3.1 and 3.2 of the present report.

In the small number of cases where creep mechanisms have been established for ordered intermetallic alloys, no new creep mechanisms have been identified. Operation of the same creep mechanisms in ordered intermetallic alloys as in disordered alloys suggests that the methods used to impart creep resistance to

disordered alloys will also be effective in ordered intermetallic alloys. Unfortunately, some of the most useful methods known for improving creep resistance are likely to exacerbate the low temperature ductility/toughness problem encountered with many ordered intermetallic alloys. For example, processing to develop coarse grain size is the most effective strengthening method known to counter diffusional creep [76], whereas fine grain size has been observed to increase tensile elongation in NiAl [39-42].

1.2.2 Deformation Mechanism Maps

Graphical representation of the constitutive relationships for creep in the form of deformation mechanism maps, as originally described by Ashby and Frost [76,93], is a conceptually useful tool for understanding the creep properties of materials. The fundamental material parameters needed to construct a deformation mechanism map are the parameters appearing in the constitutive equations described in the preceding section. The material parameters are sufficiently well known for a broad variety of metals and alloys, some ceramics, and some ionic solids to allow construction of deformation mechanism maps for representative materials from each of these classes [76]. In contrast, the only ordered intermetallic alloy for which a deformation mechanism map has been published is (Ni,Fe)Al [80,81]. The material parameters needed to construct deformation mechanism maps are simply not known for most ordered intermetallic alloys being developed as elevated temperature engineering materials.

Deformation mechanism maps for pure Ni, MAR M200, and NiAl are shown in Figure 2 (these maps were computed using the data listed in Table 1). Refinements such as rate effects associated with dislocation glide at low temperatures are not included in these maps because the data needed for the constitutive equations are not available for NiAl. In addition, the variation of shear modulus with temperature has been omitted for simplicity. Despite these simplifications, the deformation mechanism maps shown in Figure 2 can be used to compare the creep characteristics of these three materials. Comparing the maps for Ni and MAR M200 reveals the remarkable creep resistance imparted by the large volume fraction of ordered γ' precipitates in MAR M200. As noted by Frost and Ashby [76], the ordered γ' precipitates provide tremendous resistance to dislocation motion, resulting in contraction of the dislocation creep regime for MAR M200 compared with pure Ni. Diffusional creep can be

Table 1

Data Used to Construct Deformation Mechanism Maps

Material:	Ni(\$)	MAR M200(\$)	NiAl	Ref.
Crystallographic and thermal data				
Atomic volume (m ³)	1.1x10 ⁻²⁹	1.1x10 ⁻²⁹	1.2x10 ⁻²⁹	[94]
Burgers vector (m)	2.5x10 ⁻¹⁰	2.5x10 ⁻¹⁰	2.9x10 ⁻¹⁰	[38]
Melting temperature (K)	1726	1600	1913	[95]
Modulus				
Shear modulus at 300K (MPa)	7.9x10 ⁴	8.0x10 ⁴	8.1x10 ⁴	[96]
Lattice Diffusion				
D _{Lo} (m ² /s)	1.9x10 ⁻⁴	1.6x10 ⁻⁴	4.5x10 ⁻⁴	[97]
Q _L (kJ/mol)	284	285	308	[97]
Boundary Diffusion				
δD _{B0} (m ² /s)	3.5x10 ⁻¹⁵	2.8x10 ⁻¹⁵	1.3x10 ⁻¹³	(*)
Q _B (kJ/mol)	115	115	203	(*)
Core Diffusion				
a _C D _{Co} (m ² /s)	3.1x10 ⁻²³	--	--	
Q _C (kJ/mol)	170	--	--	
Dislocation Creep(#)				
n	4.6	7.7	4.6	[78]
A	3.0x10 ⁶	--	--	
Q _{PLC}	--	556	350	[78]
A _{PLC}	--	5.3x10 ³⁴	2.4x10 ²⁴	[78]
Glide				
Yield strength at 300K (MPa)	200	840	240	[98]

(\$): Data for Ni and MAR M200 from Ref. [76].

(*): Grain boundary diffusion constants estimated from volume diffusion constants using factors appropriate to bcc metals [76]: $\delta D_{B0} = b \cdot D_{Lo}$, $Q_B = 0.66 \cdot Q_L$.

(#): For MAR M200 and NiAl, the activation energy for dislocation creep exceeds Q_L. For these materials, the constitutive equation for power law creep takes the following form [76]:

$$\epsilon_{PLC} = A_{PLC} \left(\frac{\sigma}{G} \right)^n \exp \left(- \frac{Q_{PLC}}{RT} \right)$$

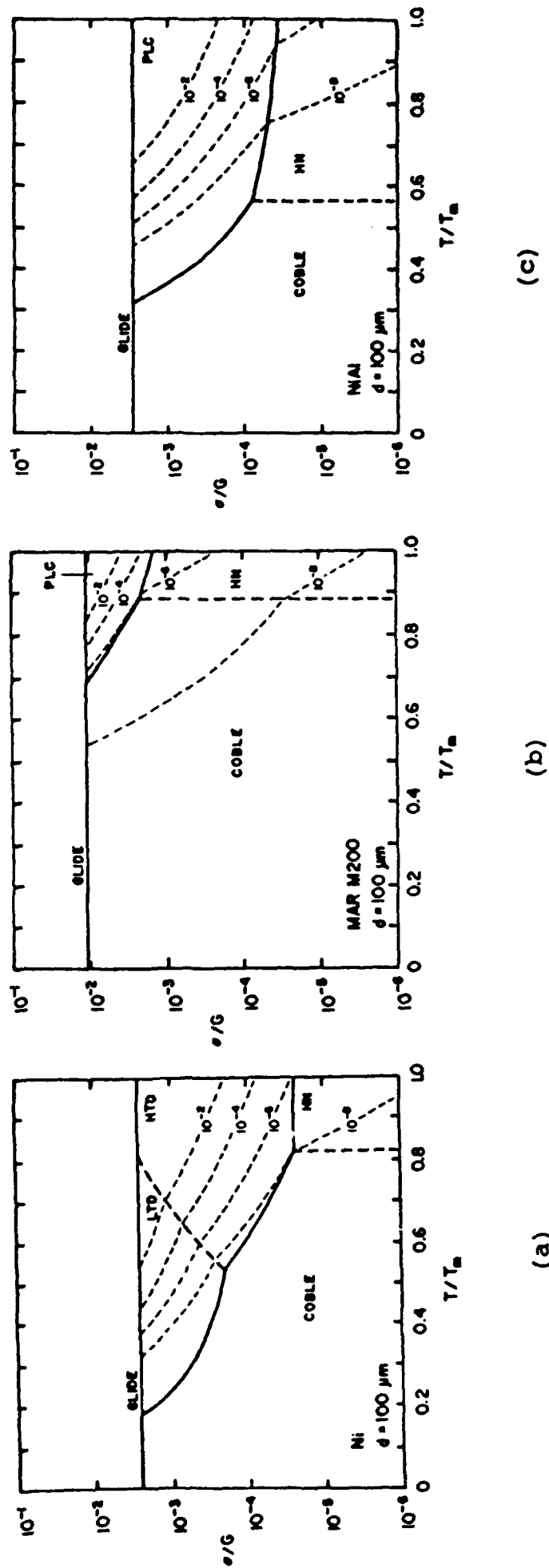


Figure 2. Deformation mechanism maps for (a) Ni, (b) MAR M200, and (c) NiAl. Small numbers designating narrow dashed lines are uniaxial tensile strain rate values (1/s) for the constant strain rate lines. LTD: low temperature dislocation creep mechanism. HTD: high temperature dislocation creep mechanism. PLC: power law creep mechanism (see footnote to Table 1). HN: Herring-Nabarro creep mechanism. (After Frost and Ashby [76] and Jung and Sauthoff [81]).

controlled by increasing the grain size, an effect which has driven development of directionally-solidified and single crystal superalloy turbine blades.

Comparison of the deformation mechanism map for NiAl with those for pure Ni and MAR M200 reveals that the creep characteristics of NiAl are similar to those pure Ni with the same grain size. These results indicate that significant strengthening of NiAl will be necessary to provide creep properties approaching those found for modern superalloys. One approach to increasing the elevated temperature strength and creep resistance of NiAl is addition of hard reinforcing particles. For example, Whittenberger and coworkers [99,100] have reported improvements in the creep resistance of NiAl through addition of TiB_2 particulate reinforcements. Such conventional approaches to strengthening can improve creep properties, but are likely to exacerbate the ductility problems characteristic of NiAl. In contrast, Sauthoff and coworkers [81] have reported modest strengthening of (Ni,Fe)Al by precipitation of α -Fe particles in the ordered intermetallic alloy, an approach which may simultaneously benefit toughness.

Even though deformation mechanism maps cannot be drawn for other intermetallic alloys because the physical and kinetic property data are lacking, it is possible to represent measured creep rates in the same format used for deformation mechanism maps. Figure 3 shows an example of this representation for 2 conventional creep-resistant Ti alloys and for several ordered intermetallic alloys based on Ti. To make this plot, values of stress required to produce a selected strain rate were interpolated from the original creep data and are represented on normalized stress and temperature scales. (Room temperature values of G were used for normalization of stress and T_m for α -Ti and Ti_3Al were estimated from Ref. [101].) While the normalized stress and temperature regimes for the conventional Ti alloys and for the ordered intermetallic alloys do not overlap, the data suggest that the normalized creep properties of Ti_3Al and 6242Si are similar near a homologous temperature of 0.45. Extrapolation of the IMI685 and 6242Si data to higher temperatures suggests that the normalized creep properties of Ti_3Al and TiAl are somewhat superior to those of conventional creep-resistant Ti alloys in the homologous temperature range 0.45 to 0.6. Since changes in the primary creep mechanism can invalidate such extrapolations, it would be preferable to compare the creep properties for similar ranges of normalized stress and temperature. Unfortunately, many investigations of creep properties provide only rupture life data that cannot be used for the type of comparison illustrated in Figure 3.

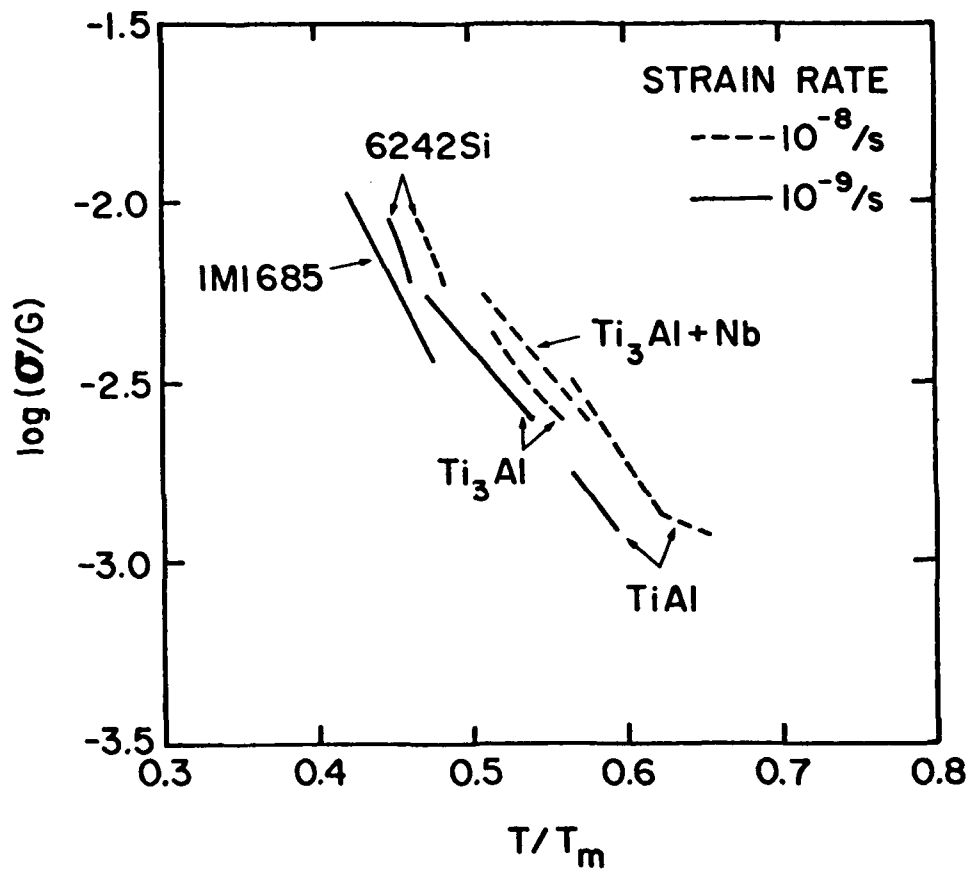


Figure 3. Normalized stress - homologous temperature combinations corresponding to minimum creep rates of 10^{-8} and 10^{-9} /s for conventional Ti alloys and Ti-base ordered intermetallic alloys. Creep data are from the following sources: 6242Si [101], IMI685 [102], Ti_3Al and $Ti_3Al + Nb$ [91], $TiAl$ [90].

The deformation mechanism maps for NiAl and Ni₃Al, and the normalized creep properties of Ti₃Al, TiAl and conventional creep-resistant Ti alloys are consistent with the conclusion that increases in G and T_m largely account for the improved creep resistance of NiAl, Ti₃Al and TiAl compared to conventional alloys. Additional comparisons of normalized creep properties need to be performed to establish the broad applicability of this conclusion. However, the data and analyses presented above suggest that ordered intermetallic alloys having values of G and T_m similar to those of conventional alloys are unlikely to exhibit creep properties significantly different from those of conventional alloys. Exceptions to this conclusion undoubtedly exist, but their discovery appears to depend more on serendipity than on materials science principles. An excellent example is described in Sections 3.1 and 3.2 where it is shown that the creep resistance of the TiAl/Ti₃Al alloy with the lamellar microstructure, investigated within the scope of the present contract, are considerably superior to the creep resistance of the individual phases. The mechanism producing the enhanced creep resistance of the lamellar alloy has been identified as enhanced dislocation density associated with the interphase interfaces in the duplex microstructure.

1.3 Organization of This Report

The contract report is organized in two parts (Sections 2 and 3) which cover the principal topics of research activity. Each part begins with a short synopsis of the findings, followed by papers that describe the research results in detail. Tables, figures and references are numbered separately within each paper.

1.4 References for Introduction

1. Lipsitt, H.A., in High-Temperature Ordered Intermetallic Alloys, Koch, C.C., Liu, C.T., and Stoloff, N.S. (eds), Materials Research Society, Pittsburgh, 1985, pp. 351-364.
2. Lipsitt, H.A., in Advanced High-Temperature Alloys: Processing and Properties, Allen, S.M., Pelloux, R.M., and Widmer, R. (eds), ASM, Metals Park, 1986, pp. 157-164.
3. Fleischer, R.L., Dimiduk, D.M., and Lipsitt, H.A., Annual Review of Materials Science, **19** (1989) 231-263.
4. Liu, C.T., Metall. Trans., **4** (1973) 1743-1753.

5. Liu, C.T., J. Nuclear Materials, 85-86 (1979) 907-911.
6. Aoki, K. and Izumi, O., J. Japan Institute of Metals, 43 (1979) 1190-1196.
7. Stoloff, N.S., Inter. Materials Reviews, 34 (1989) 153-183.
8. Stoloff, N.S., Inter. Metals Reviews, 29 (1984) 123-135.
9. Stoloff, N.S., in High-Temperature Ordered Intermetallic Alloys, Koch, C.C., Liu, C.T., and Stoloff, N.S. (eds), Materials Research Society, Pittsburgh, 1985, pp. 3-27.
10. Stoloff, N.S. and Davies, R.G., in Progress in Materials Science, Vol. 13, Chalmers, B. and Hume-Rothery, W. (eds), Pergamon Press, Oxford, 1966, pp. 1- 84.
11. Taub, A.I. and Briant, C.L., in High-Temperature Ordered Intermetallic Alloys II, Stoloff, N.S., Koch, C.C., Liu, C.T., and Izumi, O. (eds), Materials Research Society, Pittsburgh, 1987, pp. 343-353.
12. Liu, C.T., in High-Temperature Ordered Intermetallic Alloys II, Stoloff, N.S., Koch, C.C., Liu, C.T., and Izumi, O. (eds), Materials Research Society, Pittsburgh, 1987, pp. 355-367.
13. Takasugi, T. and Izumi, O., Materials Forum, 12 (1988) 8-25.
14. Baker, I. and Munroe, P.R., J. Metals, 40 (2) (1988) 28-31.
15. Gerold, V., in Dislocations in Solids, Nabarro, F.R.N. (ed), North Holland Publishing, 1979, pp. 221-259.
16. Humphreys, F.J., in Dislocations and Properties of Real Materials, The Institute of Metals, London, 1985, pp. 175-204.
17. Nicolas, A. and Poirier, J.P., Crystalline Plasticity and Solid State Flow in Metamorphic Rocks, John Wiley & Sons, London, 1976.
18. Paterson, M.S., in Dislocations and Properties of Real Materials, The Institute of Metals, London, 1985, pp. 359-377.
19. Bridgman, P.W., Studies in Large Plastic Flow and Fracture, McGraw-Hill, New York, 1952, pp. 279-291.
20. Zok, F., Embury, J.D., Vasudevan, A.K., Richmond, O., and Hack, J., Scripta Metall., 23 (1989) 1893-1899.
21. Advanced Structural Ceramics, Becher, P.F., Swain, M.V., and Somiya, S. (eds), Materials Research Society, Pittsburgh, 1987.
22. Evans, A.G. and Cannon, R.M., Acta Metall., 34 (1986) 761-800.
23. von Mises, R., Zeit. ange. Math. Mech., 8 (1928) 161-185.
24. Bishop, J.F.W., Phil. Mag., 44 (1953) 51-64.
25. Groves, G.W. and Kelley, A., Phil. Mag., 8 (1963) 877-887.
26. Kocks, U.F. and Westlake, D.G., Trans. AIME, 239 (1967) 1107-1109.
27. Hutchinson, J.W., Metall. Trans., 8A (1977) 1465-1469.
28. Fleischer, R.L., Acta Metall., 35 (1987) 2129-2136.
29. Jayaram, V., Scripta Metall., 22 (1988) 741-742.
30. Fleischer, R.L., Scripta Metall., 22 (1988) 743-744.
31. Liu, C.T., Inter. Metals Reviews, 29 (1984) 168-194.
32. Court, S.A., Lofvander, J.P.A., Loretto, M.H., and Fraser, H.L., Phil. Mag. A, 59 (1989) 379-399.
33. Court, S.A., Lofvander, J.P.A., Loretto, M.H., and Fraser, H.L., Phil. Mag. A, 61 (1990) 109-139.

34. Wasilewski, R.J., Butler, S.R., and Hanlon, J.E., Trans. AIME, 239 (1967) 1357-1364.
35. Fraser, H.L., Loretto, M.H., and Smallman, R.E., Phil Mag., 28 (1973) 667-677.
36. Fraser, H.L., Smallman, R.E., and Loretto, M.H., Phil. Mag., 28 (1973) 651-665.
37. Schulson, E.M. and Barker, D.R., Scripta Metall., 17 (1983) 519-522.
38. Ball, A. and Smallman, R.A., Acta Metall., 14 (1966) 1517-1526.
39. Schulson, E.M., in High-Temperature Ordered Intermetallic Alloys, Koch, C.C., Liu, C.T., and Stoloff, N.S. (eds), Materials Research Society, Pittsburgh, 1985, pp. 193-204.
40. Schulson, E.M., Baker, I., and Frost, H.J., in High-Temperature Ordered Intermetallic Alloys II, Stoloff, N.S., Koch, C.C., Liu, C.T., and Izumi, O. (eds), Materials Research Society, Pittsburgh, 1987, pp. 195-205.
41. Baker, I. and Munroe, P.R., J. Metals, 40 (2) (1988) 28-31.
42. Hahn, K.H. and Vedula, K., Scripta Metall., 23 (1989) 7-12.
43. Aoki, K. and Izumi, O., Trans. Japan Inst. Metals, 19 (1978) 203-210.
44. Aoki, K. and Izumi, O., Acta Metall., 26 (1978) 1257-1263.
45. Liu, C.T., White, C.L., and Horton, J.A., Acta Metall., 33 (1985) 213-229.
46. Ogura, T., Hanada, S., Masumoto, T., and Izumi, O., Metall. Trans., 16A (1985) 441-443.
47. Takasugi, T., George, E.P., Pope, D.P., and Izumi, O., Scripta Metall., 19 (1985) 551-556.
48. Hanada, S., Ogura, T., Watanabe, S., Izumi, O., and Masumoto, T., Acta Metall., 34 (1986) 13-22.
49. Cahn, R.W., Siemers, P.A., Geiger, J.E., and Bardhan, P., Acta Metall., 35 (1987) 2737-2751.
50. Cahn, R.W., Siemers, P.A., and Hall, E.L., Acta Metall., 35 (1987) 2753-2764.
51. Liu, C.T. and White, C.L., in High-Temperature Ordered Intermetallic Alloys, Koch, C.C., Liu, C.T., and Stoloff, N.S. (eds), Materials Research Society, Pittsburgh, 1985, pp. 365-380.
52. Takasagi, T. and Izumi, O., Acta Metall., 33 (1985) 1247-1258.
53. Takasagi, T., Izumi, O., and Masahashi, N., Acta Metall., 33 (1985) 1259-1269.
54. Taub, A.I. and Briant, C.L., Acta Metall., 35 (1987) 1597-1603.
55. Horton, J.A. and Miller, M.K., Acta Metall., 35 (1987) 133-141.
56. Baker, I., Schulson, E.M., and Michael, J.R., Phil. Mag. B, 57 (1988) 379-385.
57. Lange, F.F., American Ceramic Soc. Bull., 62 (1983) 1369-1374.
58. Thouless, M.D. and Evans, A.G., Acta Metall., 34 (1986) 23-31.
59. Weihs, T.P., Zinoviev, V., Viens, D.V., and Schulson, E.M., Acta Metall., 35 (1987) 1109-1118.
60. Schulson, E.M., Weihs, T.P., Baker, I., Frost, H.J., and Horton, J.A., Scripta Metall., 19 (1985) 1497-1498.
61. Schulson, E.M., Weihs, T.P., Baker, I., Frost, H.J., and Horton, J.A., Acta Metall., 34 (1986) 1395-1399.
62. Schulson, E.M., Briggs, L.J., and Baker, I., Acta Metall., 38 (1990) 207-213.

63. Oliver, W.C. and White, C.L., in High-Temperature Ordered Intermetallic Alloys II, Stoloff, N.S., Koch, C.C., Liu, C.T., and Izumi, O. (eds), Materials Research Society, Pittsburgh, 1987, pp. 241-246.
64. Crimp, M.A. and Vedula, K., *Mat. Sci. Eng.*, 78 (1986) 193-200.
65. Rice, J.R. and Thomson, R., *Phil. Mag.*, 29 (1974) 73-97.
66. Hecker, S.S., Rohr, D.C., and Stein, D.F., *Metall. Trans.*, 9A (1978) 481- 488.
67. Thomson, R., in Atomistics of Fracture, Latanision, R.M. and Pickens, J. (eds), Plenum Press, New York, 1983, pp. 167-207.
68. Ashby, M.F. and Embury, J.D., *Scripta Metall.*, 19 (1985) 557-562.
69. Ohr, S.M., *Mat. Sci. Eng.*, 72 (1985) 1-35.
70. Anderson, P.M. and Rice, J.R., *Scripta Metall.*, 20 (1986) 1467-1472.
71. Lin, I.-H. and Thomson, R., *Acta Metall.*, 34 (1986) 187-206.
72. Wang, J.-S., Anderson, P.M., and Rice, J.R., in Mechanical Behavior of Materials - V, Yan, M.G., Zhang, S.H., and Zheng, Z.M. (eds), Pergamon Press, Oxford, 1987, pp. 191-198.
73. Rice, J.R., in Chemistry and Physics of Fracture, Latanision, R.M. and Jones, R.H. (eds), Martinus Nijhoff Pub., Dordrecht, 1987, pp. 23-43.
74. Turner, C.D., Powers, W.O., and Wert, J.A., *Acta Metall.*, 37 (1989) 2635- 2643.
75. Foiles, S.M., in High-Temperature Ordered Intermetallic Alloys II, Stoloff, N.S., Koch, C.C., Liu, C.T., and Izumi, O. (eds), Materials Research Society, Pittsburgh, 1987, pp. 51-56.
76. Frost, H.J. and Ashby, M.F., Deformation-Mechanism Maps, Pergamon Press, Oxford, 1982.
77. Raj, R. and Ashby, M.F., *Metall. Trans.*, 2 (1971) 1113-1127.
78. Rudy, M. and Sauthoff, G., in High-Temperature Ordered Intermetallic Alloys, Koch, C.C., Liu, C.T., and Stoloff, N.S. (eds), Materials Research Society, Pittsburgh, 1985, pp. 327-333.
79. Rudy, M. and Sauthoff, G., *Mat. Sci. Eng.*, 81 (1986) 525-530.
80. Jung, I., Rudy, M., and Sauthoff, G., in High-Temperature Ordered Intermetallic Alloys II, Stoloff, N.S., Koch, C.C., Liu, C.T., and Izumi, O. (eds), Materials Research Society, Pittsburgh, 1987, pp. 263-274.
81. Jung, I. and Sauthoff, G., *Zeit. Metallk.*, 80 (1989) 484-489.
82. Moyer, T.D. and Doyananda, M.A., *Metall. Trans.*, 7A (1976) 1035-1040.
83. Nicholls, J.R. and Rawlings R.D., *J. Materials Science*, 12 (1977) 2456- 464.
84. Schneibel, J.H., Peterson, G.F., and Liu, C.T., *J. Materials Research*, 1 (1986) 68-72.
85. Schneibel, J.H. and Porter W.D., *J. Materials Research*, 3 (1988) 403-406.
86. Shah, D.M. and Duhi, D.N., in High-Temperature Ordered Intermetallic Alloys II, Stoloff, N.S., Koch, C.C., Liu, C.T., and Izumi, O. (eds), Materials Research Society, Pittsburgh, 1987, pp. 411-417.
87. Schneibel, J.H. and Martinez, L., in High-Temperature Ordered Intermetallic Alloys II, Stoloff, N.S., Koch, C.C., Liu, C.T., and Izumi, O. (eds), Materials Research Society, Pittsburgh, 1987, pp. 297-308.

88. Hsu, S.E., Hsu, N.N., Tong, C.H., Ma, C.Y., and Lee, S.Y., in High-Temperature Ordered Intermetallic Alloys II, Stoloff, N.S., Koch, C.C., Liu, C.T., and Izumi, O. (eds), Materials Research Society, Pittsburgh, 1987, pp. 507-512.
89. Anton, D.L., Pearson, D.D., and Snow, D.B., in High-Temperature Ordered Intermetallic Alloys II, Stoloff, N.S., Koch, C.C., Liu, C.T., and Izumi, O. (eds), Materials Research Society, Pittsburgh, 1987, pp. 287-295.
90. Martin, P.L., Mendiratta, M.G., and Lipsitt, H.A., Metall. Trans., 14A (1983) 2170-2174.
91. Mendiratta, M.G. and Lipsitt, H.A., J. Materials Science, 15 (1980) 2985- 2990.
92. Strutt, P.R., Polvani, R.S., and Ingram, J.C., Metall. Trans., 7A (1976) 23-31.
93. Ashby, M.F., Acta Metall., 20 (1972) 887-897.
94. Helfrich, W.J. and Dodd, R.A., Acta Metall., 11 (1963) 982-986.
95. Binary Alloy Phase Diagrams, Vols. 1 and 2, Massalski, T.B. (ed), ASM, Metals Park, 1986.
96. Wasilewski, R.J., Trans. AIME, 236 (1966) 455-457.
97. Wasilewski, R.J., Trans. AIME, 236 (1966) 455-457.
98. Vedula, K., in Space Age Metals Technology, Froes, F.H. and Cull, R.A. (eds), Society for the Advancement of Material and Process Engineering, Covina, 1988, pp. 49-61.
99. Whittenberger, J.D., Kumar, S., Mannan, S.K., and Viswanadham, R.K., J. Materials Science Letters, 9 (1990) 326-328.
100. Whittenberger, J.D., Viswanadham, R.K., Mannan, S.K., and Sprissler, B., J. Mat. Sci., 25 (1990) 35-44.
101. Bania, P.J. and Hall, J.A., in Titanium Science and Technology, Lutjering, G., Swicker, V., and Bunk, W. (eds.), Deutsche Gesellschaft fur Metallkunde, Oberursel, West Germany, 1985, pp. 2371-2378.
102. Assadi, A.T.K., Flower, H.M., and West, O.R.F., Metals Technology, 6 (1979) 16-23.

2. Fracture of Intermetallic Alloys

Summary: A potential explanation for cleavage fracture of intermetallic alloys with low or moderate CRSS is the existence of an energy barrier for crack tip dislocation emission, as first proposed by Rice and Thomson. The application of this concept to intermetallic alloys has been a major thrust of the present research contract, involving 3 main topics:

- i) Extension of the original Rice-Thomson model to treat the case of emission of dissociated superlattice dislocations from crack tips in intermetallic alloys.
- ii) Application of the extended model to intermetallic alloys with the $L1_2$ and B2 crystal structures.
- iii) Experimental assessment of the models for an $Al_{67}Cr_8Ti_{25}$ intermetallic alloy.

The extended model showed that dislocation emission can be inhibited in intermetallic alloys, and that this mechanism can account for observations of cleavage fracture in alloys with low or moderate CRSS. When dislocation emission is inhibited in a particular intermetallic alloy, the model predicts that cleavage fracture will occur independent of CRSS. This fracture mode prediction can be compared with the experimentally observed fracture mode for the same alloy. The papers in Sections 2.1, 2.2 and 2.3 make these comparisons for intermetallic alloys with the $L1_2$ and B2 crystal structures, and the model predictions match the experimental observations in every case where sufficient data are available to perform the model calculations (about 25 alloys in all). A key result of the modeling work is the finding that the antiphase boundary (APB) energy plays a central role in determining whether an intermetallic alloy will exhibit cleavage fracture or not. This is a novel result because it suggests that conventional metallurgical manipulations (such as processing to change the grain size) are unlikely to be effective methods for controlling cleavage fracture, but that micro- or macro-alloying to lower APB energy can prevent cleavage fracture. In addition to formulating the model and comparing model predictions with previously published results, a portion of the research has been devoted to a detailed experimental assessment of model predictions. The experimental results are found to be in good agreement with the detailed model predictions, suggesting that the conceptual basis of the dislocation emission models is sound.

The 4 papers that comprise the remainder of Section 2 of this report describe these research activities in detail.

Published in *Acta Metall. Mater.*, 40 (1992) 673.

Effect of Dislocation Dissociation on Crack Tip Plasticity in $L1_2$ Intermetallic Alloys

Michael F. Bartholomeusz and John A. Wert
Department of Materials Science
University of Virginia
Charlottesville, VA 22901

Abstract

A model describing the energy associated with emission of a dissociated $a\langle 1\bar{1}0 \rangle\{111\}$ dislocation from a crack tip in ordered intermetallic alloys with the $L1_2$ crystal structure has been formulated. The model incorporates five material parameters and two parameters defining the slip system orientation relative to the crack. Numerical calculations using the model allow determination of the range of slip system orientations for which there is no energy barrier for emission of a dissociated superlattice dislocation from a crack tip. Application of the model to a variety of intermetallic alloys with the $L1_2$ crystal structure has revealed a correlation between the observed fracture mode and the calculated range of slip system orientations for which there is no energy barrier for emission of a dissociated superlattice dislocation. The model has also been used to predict the effect of lowering the $\{111\}$ APB or SISF energy on the fracture mode of $Al_{67}Ni_8Ti_{25}$ and Al_3Sc .

1. Introduction

The phenomenon of cleavage fracture in materials with high critical resolved shear stress (CRSS) is relatively easy to rationalize: the high resistance to slip restricts crack tip plasticity, and cleavage fracture occurs as a consequence of the large tensile stress developed at the crack tip. However, many ordered intermetallic alloys that exhibit cleavage fracture have low or modest CRSS (less than $G/100$) as determined by compression or indentation tests. Since crack tip plasticity is not limited by high resistance to slip in these materials, an alternate explanation for the cause of cleavage fracture is needed.

One explanation for cleavage fracture independent of CRSS was proposed by Rice and Thomson [1] and has been elaborated by many subsequent investigators [2-10]. The model formulated by Rice and Thomson is based on the energetics of dislocation emission from crack tips. Dislocations that contribute to crack tip plasticity are assumed to be emitted in the form of semicircular loops from the free surface at the crack tip. The model reveals that dislocation energy monotonically decreases with increasing loop radius in many materials, suggesting that dislocation emission from the crack tip is energetically favorable. In other materials, the dislocation energy increases to a maximum value then decreases, as a function of loop radius. In this situation, the model suggests that an energy barrier exists, preventing dislocations from being emitted from the crack tip. The energy barrier inhibits crack tip plasticity with the result that the material exhibits cleavage fracture independent of CRSS. Rice and Thomson [1] and Stein and coworkers [2] showed that the dislocation emission model is consistent with the observed fracture behavior of a wide variety of metals, ionic solids and ceramics.

Interpretation of cleavage fracture in ordered intermetallic alloys with modest CRSS in terms of an energy barrier for dislocation emission at crack tips is relatively recent. Turner, Powers and Wert [11] showed that the ideas proposed by Rice and Thomson [1] are consistent with observation of cleavage fracture in $\text{Al}_{67}\text{Ni}_8\text{Ti}_{25}$, an ordered intermetallic alloy with the $L1_2$ crystal structure. Since the dislocations in $\text{Al}_{67}\text{Ni}_8\text{Ti}_{25}$ are perfect superlattice dislocations [11,12], the original Rice and Thomson model could be rigorously applied to this material. However, in many ordered intermetallic alloys with the $L1_2$ crystal structure, superlattice dislocations are dissociated into superlattice partial dislocations coupled by a stacking fault [13-17].

Since the original Rice and Thomson model considers only perfect dislocations, it cannot be rigorously applied to these materials.

Turner and coworkers [11] attempted to extend the Rice and Thomson [1] analysis to $L1_2$ intermetallic alloys with dissociated dislocations by considering two limiting cases: high fault energy, corresponding to emission of perfect superlattice dislocations; and low fault energy, corresponding to emission of a single superlattice partial dislocation with a trailing fault. These limiting-case analyses indicated that $L1_2$ intermetallic alloys with dissociated superlattice dislocations exhibit spontaneous emission (no energy barrier for dislocation emission) whereas alloys having undissociated superlattice dislocations exhibit an energy barrier for dislocation emission. Excellent correlation was obtained between limiting-case model results and the observed fracture mode for those $L1_2$ intermetallic alloys for which sufficient data were available to apply the limiting-case analyses.

Subsequent observations have shown that several $L1_2$ intermetallic alloys with dissociated superlattice dislocations exhibit cleavage fracture [18,19], contrary to the suggestions of Turner et al. [11]. This has led Horton and coworkers [18] to suggest low cleavage fracture strength as an alternate mechanism to explain cleavage fracture in $L1_2$ intermetallic alloys with modest CRSS. The objectives of the present investigation are to extend the original Rice and Thomson approach to accommodate dissociated dislocations, and to apply the model to $L1_2$ intermetallic alloys. In the present paper, we show that the results of the extended model are consistent with the observed fracture mode in $L1_2$ intermetallic alloys having dissociated superlattice dislocations. The model is then used to investigate the effects of temperature and variations in material properties on emission of dissociated superlattice dislocations in selected $L1_2$ intermetallic alloys.

2. Model

The primary mechanism of plastic deformation in $L1_2$ intermetallic alloys at low temperatures is glide of $a\langle 1\bar{1}0 \rangle\{111\}$ superlattice dislocations. Emission of an undissociated superlattice dislocation from a crack tip can be analyzed using the original model described by Rice and Thomson [1]. However, the $a\langle 1\bar{1}0 \rangle\{111\}$ superlattice dislocations in $L1_2$ intermetallic alloys may be dissociated via several reactions [13-17]; dissociation to form APB or SISF faults is commonly observed.

Emission of a dissociated dislocation from a crack tip requires consideration of additional factors, as described by Wang and coworkers [8] for the specific case of dissociated $a/2\langle 1\bar{1}0\rangle\{111\}$ dislocations in fcc crystals. In general, the following factors contribute to the total energy change associated with emission of a pair of fault-coupled partial dislocations from a crack tip:

- the ledge energy associated with crack tip blunting
- the change in elastic energy of the crack tip stress field
- the self energy of each partial dislocation
- the elastic interaction energy of the partial dislocations
- the energy of the fault coupling the two partial dislocations

The energy associated with each of these factors depends on the geometry of the dislocation relative to the crack, and on several material properties.

Following the original analysis by Rice and Thomson [1], we assume that the slip plane contains the crack front, as illustrated in Figure 1a. For Mode I loading, the shear stress component driving dislocation emission from the crack tip is larger for this slip plane orientation than for other orientations. An additional geometrical consideration is the shape of the emitted dislocation on the slip plane. Rice and Thomson showed that it is reasonable to assume a semicircular dislocation loop for emission of a perfect dislocation. Since interactions between the superlattice partial dislocations (elastic interaction energy and fault energy) are assumed to be isotropic in the present analysis, no factors are introduced that would cause the pair of fault-coupled superlattice partial dislocations to deviate from the semicircular loop geometry considered by Rice and Thomson. Therefore, we consider emission of concentric, semicircular, superlattice partial dislocation loops, shown schematically in Figure 1b. The Burgers vector, Burgers vector orientation and loop radius of the outer superlattice partial dislocation half loop are denoted b_1 , ψ_1 and r_1 , respectively, while those same characteristics of the inner superlattice partial dislocation half loop are denoted b_2 , ψ_2 and r_2 . The Burgers vector and Burgers vector orientation of the superlattice dislocation are denoted b_s and ψ_s . The following paragraphs describe expressions for the individual energy terms associated with emission of a pair of fault-coupled superlattice partial dislocations.

The ledge energy term results from the creation of new free surface at the crack tip as a semicircular dislocation loop expands [1]:

$$U_{\text{ledge}}(r) = 2 \gamma b^2 (r - \xi_0) \cos \psi \sin \phi \quad (1)$$

where r is the dislocation loop radius and ξ_0 is the core radius of the dislocation; both expressed in units of Burgers vector, b . The surface energy of the crack plane is represented by γ and the orientation of the slip plane and Burgers vector are specified by the angles ϕ and ψ , respectively, as defined in Figure 1. In the case of a pair of fault-coupled superlattice partial dislocations, each superlattice partial dislocation contributes an independent ledge energy term to the total energy of the superlattice dislocation.

The self energy of each partial dislocation half loop is associated with the elastic strain energy and core energy of the dislocation, accounting for the presence of the free surface and self-interaction effects. The self energy term for a semicircular dislocation loop in an elastically-isotropic medium is given by [1]:

$$U_{\text{self}}(r) = \frac{G b^3 (2 - \nu) r}{8 (1 - \nu)} \ln \left(\frac{8 r}{e^2 \xi_0} \right) \quad (2)$$

where G is the shear modulus, ν is Poisson's ratio, and e is the Naperian base. Some intermetallic alloys with the $L1_2$ crystal structure are known to be elastically anisotropic. It is therefore appropriate to use the shear modulus resolved on the slip plane, a refinement over using the polycrystalline average shear modulus [2].

The expression for the self energy of a dislocation half loop is sensitive to fairly small fluctuations in the value of the core radius, ξ_0 . We have used the following expression for the core radius [20]:

$$\xi_0 = \frac{1}{\alpha} (\cos 2\beta + e^\delta \sin 2\beta) \quad (3)$$

where

$$\beta = (-\psi + \pi) / 2$$

and

$$\delta = \frac{(1 - 2\nu)}{4(1 - \nu)}$$

Hirth and Lothe [20] suggest that a value of α near 1 is appropriate for metals and this value has been used in the present investigation.

The crack tip stress field results from the external stress, which is assumed to produce pure Mode I loading of the crack. Following the analysis performed by Rice and Thomson [1], the stress intensity is taken to be that which would cause cleavage fracture in the absence of emitted dislocations. The energy term related to the force acting on a dislocation half loop in the crack tip stress field is:

$$U_{\text{stress}}(r) = -0.986 G b^3 \sin\phi \cos\psi \cos(\phi/2) (r^{1.5} - \xi_0^{1.5}) \sqrt{\frac{2\gamma}{G b (1-\nu)}} \quad (4)$$

In the case of a pair of fault-coupled superlattice partial dislocations, an energy term of this form is associated with each superlattice partial dislocation. The U_{stress} term for emission of the inner superlattice partial dislocation is not modified as a result of prior emission of the outer superlattice partial dislocation because the crack tip radius remains smaller than the value associated with deviation from the Griffith criterion [21].

An energy term is associated with the elastic interaction of the two superlattice partial dislocations. An expression for the interaction energy between two concentric dislocation loops has been derived by Lardner [22]. For dislocation half-loops at the crack tip, the expression for the interaction energy is reduced by a factor of two [8]. The resulting expression is:

$$U_{\text{int}}(r_1, r_2) = \frac{G b^3 (2-\nu)}{8 (1-\nu)} (r_1 + r_2) (2-m) K(m) - 2 E(m) \quad (5)$$

where

$$m = \frac{4 r_1 r_2}{(r_1 + r_2)^2}$$

In Eq. (5), $K(m)$ and $E(m)$ represent complete elliptical integrals of the first and second kinds. In the specific case of dissociated $a\langle 1\bar{1}0 \rangle\{111\}$ dislocations in $L1_2$ intermetallic alloys, the U_{int} terms for the APB and SISF cases differ by a constant factor. This is because the expression for the interaction energy between two concentric loops derived by Lardner [22] is explicitly for the situation where the dislocation loops have parallel Burgers vectors. To apply this equation to superlattice partial dislocations

associated with an SISF fault, the Burgers vectors are resolved into parallel and antiparallel components.

Lastly, a fault energy term proportional to the area between the two superlattice partial dislocation half loops takes the form [8]:

$$U_{\text{sfe}}(r_1, r_2) = \frac{\pi \Gamma b^2}{2} (r_1^2 - r_2^2) \quad (6)$$

where Γ is the stacking fault energy. In the case of dissociated $a\langle 1\bar{1}0 \rangle \{111\}$ superlattice dislocations in an $L1_2$ intermetallic alloy, Γ is the $\{111\}$ APB or SISF energy.

The expression for the total energy change, U_{tot} , associated with emission of a pair of fault-coupled superlattice partial dislocation half loops from a crack tip is a linear combination of the individual energy terms described previously:

$$U_{\text{tot}} = U_{\text{ledge}}(r_1) + U_{\text{ledge}}(r_2) + U_{\text{self}}(r_1) + U_{\text{self}}(r_2) + U_{\text{stress}}(r_1) + U_{\text{stress}}(r_2) + U_{\text{int}}(r_1, r_2) + U_{\text{sfe}}(r_1, r_2) \quad (7)$$

Since the U_{ledge} , U_{self} and U_{stress} terms apply to the individual superlattice partial dislocations, they appear twice in Eq. (6); r_1 and ψ_1 are used in the terms associated with the outer superlattice partial dislocation, and r_2 and ψ_2 are used in the terms associated with the inner superlattice partial dislocation. When the separation between superlattice partial dislocations is smaller than $2\xi_0$, core overlap invalidates the assumption of linear elasticity implicit in the expressions used for several of the energy terms. When the calculated equilibrium spacing of superlattice partial dislocations is less than $2\xi_0$, the superlattice dislocation is effectively undissociated and the original model formulated by Rice and Thomson [1] can be used to evaluate the energetics of crack tip dislocation emission.

To clarify the broad character of the analysis, consider for the moment that the separation between the two superlattice partial dislocations is fixed at a constant value (the equilibrium separation for a pair of straight superlattice partial dislocations, for example). In this situation where r_2 is related to r_1 by an additive constant, U_{tot} can be expressed in terms of r_1 alone and the individual energy terms depend on r_1 as follows:

$$\begin{aligned}
U_{\text{ledge}} &\propto r_1 \\
U_{\text{self}} &\propto r_1 \ln r_1 \\
U_{\text{stress}} &\propto -r_1^{3/2} \\
U_{\text{int}} &\propto r_1 \ln r_1 \\
U_{\text{sfe}} &\propto r_1
\end{aligned}$$

For large values of r_1 the U_{stress} term is dominant for most slip system orientations, regardless of the material parameters. For smaller values of r_1 , depending on the material parameters, the other terms may dominate. If the total energy monotonically decreases from an initial value of zero, spontaneous emission of the coupled superlattice partial dislocations occurs. In contrast, if U_{tot} increases at small r_1 , an energy barrier exists for emission of the dissociated superlattice dislocation. In this case, crack extension occurs rather than plastic blunting of the crack.

The concepts described in the previous paragraph are essentially identical to those considered by Rice and Thomson [1] for emission of an undissociated dislocation. In the case of emission of a dissociated dislocation, the requirement of constant spacing is relaxed and the equilibrium separation of the superlattice partial dislocations may be quite different in the rapidly-varying stress field ahead of the crack tip compared to the equilibrium separation in an unstressed crystal. To account for this effect, the following analysis method has been used. For fixed values of ϕ , ψ_s and the material parameters, the radius of the outer dislocation loop is increased stepwise. For each value of r_1 , the value of r_2 is chosen such that the same *net* force per unit length is exerted on the inner and outer superlattice partial dislocations. This condition is equivalent to a requirement that the two superlattice partial dislocations have equal velocities as the concentric half loops expand.

In practice, the value of r_2 satisfying the above requirement is the solution to the following differential equation:

$$\begin{aligned}
\frac{d}{dr_1} \left[\left(U_{\text{ledge}}(r_1) + U_{\text{self}}(r_1) + U_{\text{stress}}(r_1) + U_{\text{int}}(r_1, r_2) + U_{\text{sfe}}(r_1, r_2) \right) / \pi r_1 \right] = \\
\frac{d}{dr_2} \left[\left(U_{\text{ledge}}(r_2) + U_{\text{self}}(r_2) + U_{\text{stress}}(r_2) + U_{\text{int}}(r_1, r_2) + U_{\text{sfe}}(r_1, r_2) \right) / \pi r_2 \right] \quad (8)
\end{aligned}$$

When the radius of the dissociated superlattice dislocation half loop is large, the derivatives associated with the ledge, self and stress energy terms are nearly equal and the equilibrium spacing between the superlattice partial dislocations is given by the usual balance between the repulsive force associated with elastic strain energy and the attractive force associated with the stacking fault. Finally, evaluation of the derivatives of the elliptical integrals appearing in the expression for U_{int} was performed using polynomial approximations for the integrals [23].

By requiring that the same net force per unit length act on the inner and outer superlattice partial dislocations, r_2 becomes a function of r_1 and the total energy of the superlattice partial dislocation half loops at the crack tip can be represented as a function of r_1 . For many slip system orientations, U_{tot} increases to a maximum value as a function of r_1 . The increase in U_{tot} represents an energy barrier to emission of a dissociated superlattice dislocation from the crack tip and the maximum value of U_{tot} is the activation energy for emission, U_{act} . In the case of emission of an undissociated dislocation, the energy barrier to dislocation emission consists of a single maximum as illustrated in Figure 2a. In the case of emission of a dissociated dislocation, U_{tot} can exhibit more complex behavior as a function of r_1 ; several examples are shown in Figure 2b. U_{act} is defined as the height of the largest barrier in each case.

3. Results

The expression for U_{tot} is a function of five material parameters (G , b , γ , ν , Γ), two geometrical parameters (ϕ , ψ_s), and r_1 . For fixed values of the material and geometrical parameters, the activation energy for emission of a dissociated superlattice dislocation can be evaluated numerically, as described in the previous section. For a given material, it is therefore possible to represent graphically the activation energy for superlattice dislocation emission, U_{act} , as a function of the two geometrical parameters, ϕ and ψ_s . Since the geometrical parameters describe the slip system orientation relative to the crack, they thus account for the variety of grain orientations encountered along a crack front.

The material constants G , b , ν , and Γ have been reported or can be estimated for seven ordered intermetallic alloys with the $L1_2$ crystal structure; these values are listed in Table 1. The values of shear modulus in Table 1 are denoted G_{slip} because they represent the shear modulus on the slip plane, as discussed previously. The measured

polycrystalline shear modulus of Al_3Zr is 49 GPa [29], from which G_{slip} was estimated by assuming a value of 2 for the Zener anisotropy parameter [32]: $A_z = 2c_{44}/(c_{11} - c_{12})$. Values of A_z for the other L1_2 intermetallic alloys listed in Table 1 range from 0.9 to 3.3 [24,31]. The free surface energy has not been reported for any intermetallic alloy and, consequently, must be estimated. The method adopted was that described by Reynolds et al. [26] which relates the free surface energy of an elemental metal to melting temperature and interatomic spacing:

$$\gamma = 760 + 4.77 T_m / r_o^2 \quad (9)$$

where γ is the average free surface energy at the melting temperature (mJ/m^2), T_m is the absolute melting temperature, and r_o is the minimum interatomic spacing expressed in Angstroms. To obtain the free surface energy at room temperature, the approximate temperature dependence $d\gamma/dT = -0.5 \text{ mJ/m}^2\text{K}$ was employed [33].

For purposes of representing U_{act} as a function of the geometrical parameters ϕ and ψ_s , it is convenient to segregate the results for L1_2 intermetallic alloys that exhibit APB-type dissociation and those that exhibit SISF-type dissociation. Figure 3 shows U_{act} as a function of slip system orientation relative to a crack for three alloys that manifest APB-type dissociation and for $\text{Al}_{67}\text{Ni}_8\text{Ti}_{25}$ in which the $a\langle 1\bar{1}0 \rangle\{111\}$ dislocations are undissociated. The constant energy contours in the plots comprising Figure 3 represent conditions of constant activation energy for superlattice dislocation emission. The activation energy axis of the plots was truncated at 30 eV, resulting in a plateau at this value of activation energy. The plateau at 0 eV in the plots in Figures 3 represents combinations of ϕ and ψ_s corresponding to spontaneous emission of dissociated superlattice dislocations. For alloys that exhibit APB-type dissociation or perfect superlattice dislocations, only the positive ranges of ϕ and ψ_s need to be represented since U_{act} is symmetric for positive and negative values of these variables. The significance of these results is discussed in Section 4 of the present paper.

Figure 4 shows similar results for two L1_2 intermetallic alloys that exhibit SISF-type dissociation of $a\langle 1\bar{1}0 \rangle\{111\}$ dislocations. In this case, U_{act} is not symmetric for positive and negative values of ψ_s because the two superlattice partial dislocations have different orientations on the slip plane. Thus, calculations have been performed for ψ_s ranging from -90° to $+90^\circ$. However, to effectively display the results of the calculations, the range of ψ_s shown in Figure 4 is -60° to $+10^\circ$. Figure 4 shows that

both Zr_3Al and $\text{Al}_{66}\text{Fe}_6\text{Ti}_{23}\text{V}_5$ have a range of slip system orientations corresponding to spontaneous emission of dissociated superlattice dislocations.

4. Discussion

4.1 Correlation Between Spontaneous Emission of Superlattice Dislocations and Fracture Mode

To summarize the graphical result for each intermetallic alloy, it is convenient to introduce a parameter, ζ , defined as the fractional angular range of ϕ and ψ_s corresponding to spontaneous emission ($U_{\text{act}} = 0$) for a given material. The parameter ζ characterizes the solid angle range for which spontaneous emission occurs, normalized by the solid angle range for all possible orientations of a superlattice dislocation lying on a slip plane that contains the crack tip. The normalization factor corresponds to a ϕ range from -180° to $+180^\circ$ and a ψ_s range from -90° to $+90^\circ$. Since we consider thermally-activated dislocation emission in a later section, it is convenient to distinguish between the value of ζ associated with spontaneous emission of a dissociated superlattice dislocation without thermal activation, denoted $\zeta(0)$, and the value of ζ associated with spontaneous or thermally-activated emission at temperature T , denoted $\zeta(T)$.

Table 2 lists values of $\zeta(0)$ and the fracture mode observed at room temperature for the L1_2 intermetallic alloys considered. Some ordered intermetallic alloys fail in a macroscopically brittle fashion by intergranular fracture when tested in polycrystalline form. Since the present investigation seeks to define the conditions that permit sufficient crack tip plasticity to avoid transgranular cleavage fracture, other mechanisms of brittle fracture are excluded from consideration. In cases where polycrystalline specimens fail by intergranular fracture (Ni_3Al , for example [35]), it is appropriate to list the single crystal fracture mode in Table 2.

Comparing the fractional angular range for spontaneous emission of superlattice dislocations and the fracture modes listed in Table 2 reveals a strong correlation. The correlation between $\zeta(0)$ and the observed fracture mode can be rationalized by considering that $\zeta(0)$ describes the range of slip system orientations for which dislocation emission from a crack tip is spontaneous. This suggests that $\zeta(0)$ is related to the fraction of grains at the crack tip which are favorably oriented for crack tip

plasticity. Large values of $\zeta(0)$ should therefore be found for materials that exhibit ductile fracture and small values of $\zeta(0)$ should be found for materials that exhibit cleavage fracture. The correlation shown in Table 2 suggests that the critical value of $\zeta(0)$ corresponding to the transition from cleavage fracture to a ductile fracture mode is between 0.045 and 0.052. Owing to the restricted geometry used to determine $\zeta(0)$ (crack front contained in the slip plane), attaching fundamental significance to the value of $\zeta(0)$ corresponding to the transition from cleavage to ductile fracture does not appear to be justifiable.

4.2 Thermal Activation Effects

The results of the dislocation emission model suggest that Al_3Sc , $\text{Al}_{66}\text{Fe}_6\text{Ti}_{23}\text{V}_5$, and $\text{Al}_{67}\text{Ni}_8\text{Ti}_{25}$ exhibit brittle fracture because they have an insufficient range of grain orientations for which spontaneous emission of dislocations can occur at crack tips. However, small energy barriers for dislocation emission exist over a significant range of slip system orientations for all three of these alloys. Thermally-activated dislocation emission over small energy barriers is possible [1,9], effectively expanding the range of slip system orientations for which dislocation emission can occur. At room temperature, the thermal energy available to assist dislocation emission is approximately 1 eV (equivalent to the total thermal energy of the atoms in the core of a dislocation $10b$ in length). Assuming that dislocation emission can occur over energy barriers smaller than 1 eV at room temperature, values of $\zeta(293)$ can be calculated for the various intermetallic alloys; these values are shown in Table 2.

Comparing the values of $\zeta(0)$ and $\zeta(293)$ shows that including thermal energy effects at room temperature raises the fractional angular ranges for which emission is favorable, but the correlation identified in the absence of thermal effects remains valid. Assuming that 1 eV of thermal energy is available at room temperature, the transition between brittle and ductile fracture modes occurs for $\zeta(293)$ between 0.069 and 0.085. However, since no fundamental significance has been attached to the value of ζ corresponding to the transition from brittle to ductile behavior, incorporation of the thermal effects at room temperature introduces no new insight into the crack tip dislocation emission process.

Rice and Thomson [1] suggested that the brittle-to-ductile transition observed with increasing temperature in some materials could be explained by thermal activation

of dislocations over the crack tip energy barrier. Figure 5 shows the effect of thermal energy availability on thermally-activated emission of dissociated dislocations in Al_3Sc , $\text{Al}_{66}\text{Fe}_6\text{Ti}_{23}\text{V}_5$, and $\text{Al}_{67}\text{Ni}_8\text{Ti}_{25}$. For each alloy, $\zeta(T)$ increases with increasing availability of thermal energy, as expected. In the case of Al_3Sc and $\text{Al}_{66}\text{Fe}_6\text{Ti}_{23}\text{V}_5$, $\zeta(T)$ attains values near 0.08 that are characteristic of $\zeta(293)$ for the L1_2 intermetallic alloys that exhibit ductile fracture at room temperature. This suggests that a brittle-to-ductile transition might occur in Al_3Sc near 800 K, and in $\text{Al}_{66}\text{Fe}_6\text{Ti}_{23}\text{V}_5$ near 1100 K, as a consequence of thermally-activated dislocation emission over the crack tip energy barrier. For $\text{Al}_{67}\text{Ni}_8\text{Ti}_{25}$, the temperature required to increase $\zeta(T)$ to 0.08 exceeds the melting temperature of the material, suggesting that no brittle-to-ductile transition would be observed in this case.

Experimental observations have shown that L1_2 intermetallic alloys with compositions similar to $\text{Al}_{66}\text{Fe}_6\text{Ti}_{23}\text{V}_5$ ($\text{Al}_{66}\text{Fe}_9\text{Ti}_{25}$ and $\text{Al}_{66}\text{Fe}_9\text{Ti}_{23}\text{V}_2$) exhibit a brittle-to-ductile transition at about 1000 K [37]. The approximate agreement between the observed brittle-to-ductile transition temperature and the model results suggests that thermally-activated emission of dissociated superlattice dislocations could account for the observed brittle-to-ductile transition in several $(\text{Al,Fe})_3(\text{Ti,V})$ intermetallic alloys. However, other deformation characteristics also change at elevated temperatures: CRSS decreases in $(\text{Al,Fe})_3\text{Ti}$ alloys above approximately 800 K [38] and $\{001\}$ slip is observed at 873 K [19]. The extent to which thermal activation of $a\langle 1\bar{1}0 \rangle\{111\}$ dislocations over the crack tip energy barrier may contribute to the observed brittle-to-ductile transition is uncertain. The results shown in Figure 5 also suggest that a brittle-to-ductile transition is expected for Al_3Sc , but not for $\text{Al}_{67}\text{Ni}_8\text{Ti}_{25}$. The elevated temperature fracture characteristics of Al_3Sc and $\text{Al}_{67}\text{Ni}_8\text{Ti}_{25}$ have not been reported so it is not possible to compare these theoretical results with experimental observations.

In addition to thermal activation, ζ could change as a consequence of changing material properties with increasing temperature. Unfortunately, the temperature dependence of the material properties used in the present model is unknown for the intermetallic alloys investigated. In lieu of a complete analysis, we have made a rough estimate of the potential importance of this effect for Cu_3Au . The temperature dependence of the elastic constants for Cu_3Au has been reported [39] and a typical value for the temperature dependence of free surface energy has been cited above [33]. The temperature dependence of APB energy has not been reported, but measurements of stacking fault energy in fcc metals show a mild increase with

temperature [40]. Assuming the temperature dependence of APB energy in Cu_3Au to be similar to that of stacking fault energy in fcc metals, the temperature dependence of ζ was calculated for Cu_3Au over the temperature range 293 to 573 K. The results show that ζ decreases slightly over this temperature range. The insensitivity of ζ to temperature changes in the case of Cu_3Au results from compensating changes in the material parameters: G and γ decrease with temperature while Γ and ν increase with temperature. Although the analysis for Cu_3Au involves many assumptions, it suggests that gradual changes in material properties with temperature may not produce significant changes in ζ .

4.3 Effect of Fault Energy on Fracture Mode

Correlation of the parameter $\zeta(293)$ with the observed fracture mode shows that L1_2 intermetallic alloys having calculated values of $\zeta(293)$ exceeding about 0.08 exhibit ductile fracture at room temperature. It is of interest to consider what changes in material properties would be necessary to increase the value of $\zeta(293)$ for alloys that exhibit cleavage fracture. Conventional metallurgical manipulations, such as changing grain size, do not affect the value of $\zeta(293)$. This is consistent with the absence of reports of metallurgical manipulations changing the room temperature fracture mode of L1_2 intermetallic alloys that exhibit cleavage fracture. According to the present model, only changes in G , b , ν , Γ , or γ can influence the fracture mode. Of these, Γ is the most susceptible to manipulation by variation of chemical composition.

Consider $\text{Al}_{67}\text{Ni}_8\text{Ti}_{25}$, which has undissociated $a\langle 1\bar{1}0 \rangle\{111\}$ dislocations at room temperature [11,12], and Al_3Sc , which exhibits APB-type dissociation of $a\langle 110 \rangle\{111\}$ dislocations but has a relatively high $\{111\}$ APB energy [18]. Figure 6 shows the effect of APB energy on $\zeta(293)$ for these alloys, assuming the other material parameters remain unchanged. This plot suggests that lowering the APB energy of $\text{Al}_{67}\text{Ni}_8\text{Ti}_{25}$ below approximately 330 mJ/m^2 and that of Al_3Sc below 270 mJ/m^2 would increase $\zeta(293)$ into the range associated with ductile fracture at room temperature in other L1_2 intermetallic alloys. Note the $\zeta(293)$ is larger for emission of undissociated superlattice dislocations than for emission of APB-dissociated superlattice dislocations in $\text{Al}_{67}\text{Ni}_8\text{Ti}_{25}$ when the APB energy exceeds approximately 420 mJ/m^2 . Similar calculations show that lowering the SISF energy of $\text{Al}_{67}\text{Ni}_8\text{Ti}_{25}$ and Al_3Sc does not significantly affect $\zeta(293)$ suggesting that lowering the SISF energy of these alloys would not change their fracture mode.

While experimental results are not available for comparison with the calculations predicting a change in fracture mode of $\text{Al}_{67}\text{Ni}_8\text{Ti}_{25}$ and Al_3Sc with lower APB energy, results for other modified Al_3Ti alloys with the L_{12} crystal structure are worth noting. Recent results reported for $(\text{Al,Cr})_3\text{Ti}$ and $(\text{Al,Mn})_3\text{Ti}$ alloys suggest that the $\{111\}$ APB energies in these alloys are lower than in other alloys in the modified Al_3Ti family [41]. In addition, limited tensile ductility in $(\text{Al,Cr})_3\text{Ti}$ and $(\text{Al,Mn})_3\text{Ti}$ has been reported at room temperature [41-43]. While the full set of material parameters needed to determine $\xi(293)$ for the $(\text{Al,Cr})_3\text{Ti}$ and $(\text{Al,Mn})_3\text{Ti}$ alloys have not been reported, observation of limited tensile ductility in conjunction with more widely dissociated superlattice dislocations is consistent with the present modeling results.

5. Conclusions

A model describing the energy associated with emission of a dissociated $a\langle\bar{1}10\rangle\{111\}$ dislocation from a crack tip in ordered intermetallic alloys with the L_{12} crystal structure has been formulated. Numerical calculations using the model allow determination of the range of slip system orientations for which there is spontaneous emission of dissociated dislocations from the crack tip. Application of the model to a variety of intermetallic alloys with the L_{12} crystal structure has revealed a correlation between the angular range of slip system orientations corresponding to spontaneous emission of dissociated superlattice dislocations and the observed fracture mode. The model has also been used to predict the effect of lowering the $\{111\}$ APB energy on fracture mode of $\text{Al}_{67}\text{Ni}_8\text{Ti}_{25}$ and Al_3Sc . The model results suggest that lowering the $\{111\}$ APB energy in $\text{Al}_{67}\text{Ni}_8\text{Ti}_{25}$ below 330 mJ/m^2 and in Al_3Sc below 270 mJ/m^2 would allow sufficient spontaneous or thermally-activated emission of dissociated superlattice dislocations to avoid cleavage fracture at room temperature.

6. Acknowledgements

The authors are grateful to Professors D. Mikkola and R.A. Johnson for helpful comments. This work was sponsored by AFOSR under contract number AFOSR-90-0143; Dr. A. Rosenstein was the contract monitor.

7. References

1. J.R. Rice and R. Thomson, *Phil. Mag.*, 29 (1974) 73-97.
2. S.S. Hecker, D.C. Rohr and D.F. Stein, *Met. Trans.*, 9A, (1978) 481-488.
3. R. Thomson, in *Atomistics of Fracture*, R.M. Latanision and J. Pickens (eds.), Plenum Press, New York, 1983, pp. 167-207.
4. M.F. Ashby and J.D. Embury, *Scripta Metall.*, 19 (1985) 557-562.
5. I.-H. Lin and R. Thomson, *Acta Metall.*, 34 (1986) 187-206.
6. P.M. Anderson and J.R. Rice, *Scripta Metall.*, 20 (1986) 1467-1472.
7. J.R. Rice, in *Chemistry and Physics of Fracture*, R.M. Latanision and R.H. Jones (eds.), Hartinus Nijoff Pub., Dordrecht, 1987, pp. 23-43.
8. J.-S. Wang, P.M. Anderson and J.R. Rice, in *Mechanical Behavior of Materials - V*, M.G. Yan, S.H. Zhang and Z.M. Zheng (eds.), Pergamon Press, Oxford, 1987, pp. 191-198.
9. D.H. Kim, *Scripta Metall.*, 24 (1990) 687-690.
10. S.M. Ohr, *Mat. Sci. Eng.*, 72 (1985) 1-35.
11. C.D. Turner, W.O. Powers and J.A. Wert, *Acta Metall.*, 37 (1989) 2635-2643.
12. V.K. Vasudevan, R. Wheeler and H.L. Fraser, in *High Temperature Ordered Intermetallic Alloys III*, C.T. Liu, A.I. Taub, N.S. Stoloff and C.C. Koch (eds.), Materials Research Society, Pittsburgh, 1989, pp. 705-710.
13. M.J. Marcinkowski, in *Electron Microscopy and Strength of Crystals*, G. Thomas and J. Washburn, Wiley Interscience, New York, 1963, pp. 333-440.
14. N.S. Stoloff and R.G. Davies, in *Progress in Materials Science*, Vol. 13, Chalmers, B. and Hume-Rothery, W. (eds), Pergamon Press, Oxford, 1966, pp. 1-84.
15. M.J. Marcinkowski, in *Treatise on Materials Science and Technology*, Volume 5, Herman, H. (ed), Academic Press, New York, 1974, pp. 181-287.
16. M. Yamaguchi, V. Vitek and D.P. Pope, *Phil. Mag. A*, 43 (1981) 1027-1044.
17. D.P. Pope and S.S. Ezz, *Inter. Metals Reviews*, 29 (1984) 136-167.
18. E.P. George, J.A. Horton, W.D. Porter and J.H. Schneibel, *J. Materials Research*, 5 (1990) 1639-1648.
19. H. Inui, D.E. Luzzi, D.P. Pope, V. Vitek and M. Yamaguchi, "Transmission Electron Microscopy Study of Dislocation Structures in Iron Doped Al_3Ti with the $L1_2$ Crystal Structure", to be published in *Philosophical Magazine*.
20. J.P. Hirth and J. Lothe, *Theory of Dislocations*, McGraw-Hill, New York, 1968, pp. 211-214 and pp. 325-329.
21. E. Orowan, *The Welding Journal*, 34, no. 3 (1955) 157s-160s.

22. R.W. Lardner, *Mathematical Expositions*, University of Toronto Press, Toronto, 1974, pp. 281-295.
23. M. Abramowitz and I.A. Stegun, *Handbook of Mathematical Functions*, Dover, New York, 1972, pp. 591-592.
24. M.H. Yoo, *Acta Metall.*, 35 (1987) 1559-1569.
25. P. Villars and L.D. Calvert, *Pearson's Handbook of Crystallographic Data for Intermetallic Phases*, American Society for Metals, Metals Park, 1985.
26. C.L. Reynolds, P.R. Couchmand and F.E Karasz, *Phil. Mag.*, 34 (1976) 659-661.
27. S.M.L. Sastry and B. Ramaswami, *Phil Mag.*, 33 (1976) 375-380.
28. A. Korner and H.P. Karnthaler, *Phil Mag.*, 52 (1985) 29-38.
29. E.M. Schulson, *Met. Trans.*, 9A (1978) 527-538.
30. L.M. Howe, M. Rainville and E.M. Schulson, *J. Nuclear Materials*, 50 (1975) 139-154.
31. C.L. Fu, *J. Materials Research*, 5 (1990) 971-979.
32. G. Grimvall, *Thermophysical Properties of Materials*, North-Holland, Amsterdam, 1986, p. 30.
33. L.E. Murr, "Interfacial Phenomena in Metals and Alloys", Addison-Wesley, Reading, 1975, p. 122.
34. K.H. Chien and E.A. Starke, *Acta Metall.*, 23 (1975) 1173-1184.
35. N.S. Stoloff, *Inter. Materials Reviews*, 34 (1989) 153-183.
36. T. Takasugi and O. Izumi, *Acta Metall.*, 33 (1985) 1247-1258.
37. K.S. Kumar, Martin-Marietta Laboratory, Baltimore, private communication, 1991.
38. Z.I. Wu, D.P. Pope and V. Vitek, *Scripta Metall.*, 24 (1990) 2187-2190.
39. S. Siegel, *Phys. Rev.*, 57 (1940) 537-545.
40. L. Remy, A. Pineau and B. Thomas, *Mat. Sci. Eng.*, 36 (1978) 47-63.
41. S. Zhang, J.P. Nic, W.W. Milligan and D.E. Mikkola, *Scripta Metall.*, 24 (1990) 1441-1446.
42. S. Zhang, J.P. Nic and D.E. Mikkola, *Scripta Metall.*, 24 (1990) 57-62.
43. J.P. Nic, S. Zhang and D.E. Mikkola, *Scripta Metall.*, 24 (1990) 1099-1104.

Table 1

Material Parameters for the L1₂ Intermetallic Alloys
Considered in the Present Investigation

Material	G _{slip} GPa	K GPa	a ₀ nm	γ J/m ²	Γ(APB) J/m ²	Γ(SISF) J/m ²	Refs. #
Cu ₃ Au	33	152	0.3748	2.1	0.04		[24,24,25,26,27]
Ni ₃ Al	49	173	0.3566	2.7	0.18	0.01	[24,24,25,26,24]
Ni ₃ Fe	62	181	0.3555	2.0	0.13		[24,24,25,26,28]
Zr ₃ Al	36*	202	0.4372	2.4		0.08	[29,29,25,26,30]
Al ₃ Sc	71	99	0.41	2.3	0.31		[31,31,18,26,18]
Al ₆₇ Ni ₈ Ti ₂₅	69 ⁺	116	0.385	2.4	--	--	[11,11,11,26,11]
Al ₆₆ Fe ₆ Ti ₂₃ V ₅	70 ⁺	90	0.395	2.4		0.10	[18,18,18,26,18]

* Estimated value on the slip plane, see text.

+ Shear modulus on the slip plane estimated from polycrystalline shear modulus and A₂ = 1.7 calculated for Al₃Ti in L1₂ crystal structure [31].

References listed in same order as parameters in the table.

Table 2

Correlation Between ζ and Fracture Mode for the L1₂ Intermetallic Alloys
Considered in the Present Investigation

Material and dislocation dissociation mode		ζ(0)	ζ(293)	Fracture mode	Ref.
Cu ₃ Au	APB	0.169	0.262	Ductile	[34]
Ni ₃ Al	APB	0.130	0.196	Ductile	[35]
Ni ₃ Al	SISF	0.052	0.090	Ductile	[35]
Ni ₃ Fe	APB	0.100	0.156	Ductile	[36]
Zr ₃ Al	SISF	0.052	0.085	Ductile	[29]
Al ₃ Sc	APB	0.045	0.069	Brittle	[18]
Al ₆₇ Ni ₈ Ti ₂₅	None	0.033	0.043	Brittle	[11]
Al ₆₆ Fe ₆ Ti ₂₃ V ₅	SISF	0.022	0.042	Brittle	[18]

List of Figures

Fig. 1 Crack tip and slip system geometry. a. Geometry of a dislocation half loop emitted from a crack tip. b. Geometry of a dissociated superlattice dislocation on the slip plane.

Fig. 2 Schematic representation of the total energy of a superlattice dislocation emitted from a crack tip as a function of dislocation half loop radius. a. Energy barrier for emission of an undissociated superlattice dislocation. b. Two types of energy barrier for emission of a dissociated superlattice dislocation. r_1^* represents the radius of the outer superlattice partial dislocation when the inner superlattice partial dislocation is emitted.

Fig. 3 Activation energy for emission of a dissociated superlattice dislocation as a function of slip system orientation in several $L1_2$ intermetallic alloys exhibiting APB-type dissociation. a. Cu_3Au . b. Ni_3Al . c. Al_3Sc d. $\text{Al}_{67}\text{Ni}_8\text{Ti}_{25}$.

Fig. 4 Activation energy for emission of a dissociated superlattice dislocation as a function of slip system orientation in two $L1_2$ intermetallic alloys exhibiting SISF-type dissociation. a. Zr_3Al . b. $\text{Al}_{66}\text{Fe}_6\text{Ti}_{23}\text{V}_5$. In this figure, the ψ (ψ) axis of the plots represents ψ_s which represents the Burgers vector orientation of the superlattice dislocation.

Fig. 5 Effect of thermal energy on the fractional angular range for spontaneous or thermally-activated dislocation emission, $\zeta(T)$, in several $L1_2$ intermetallic alloys.

Fig. 6 Effect of $\{111\}$ APB energy on the fractional angular range for spontaneous emission, $\zeta(293)$, in $\text{Al}_{67}\text{Ti}_8\text{Ti}_{25}$ and Al_3Sc .

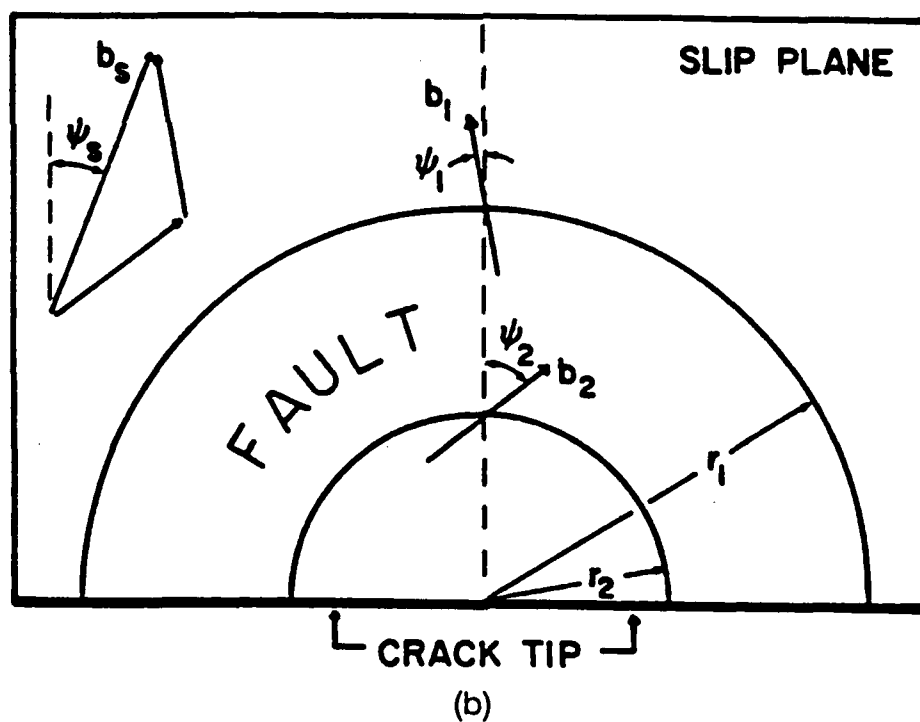
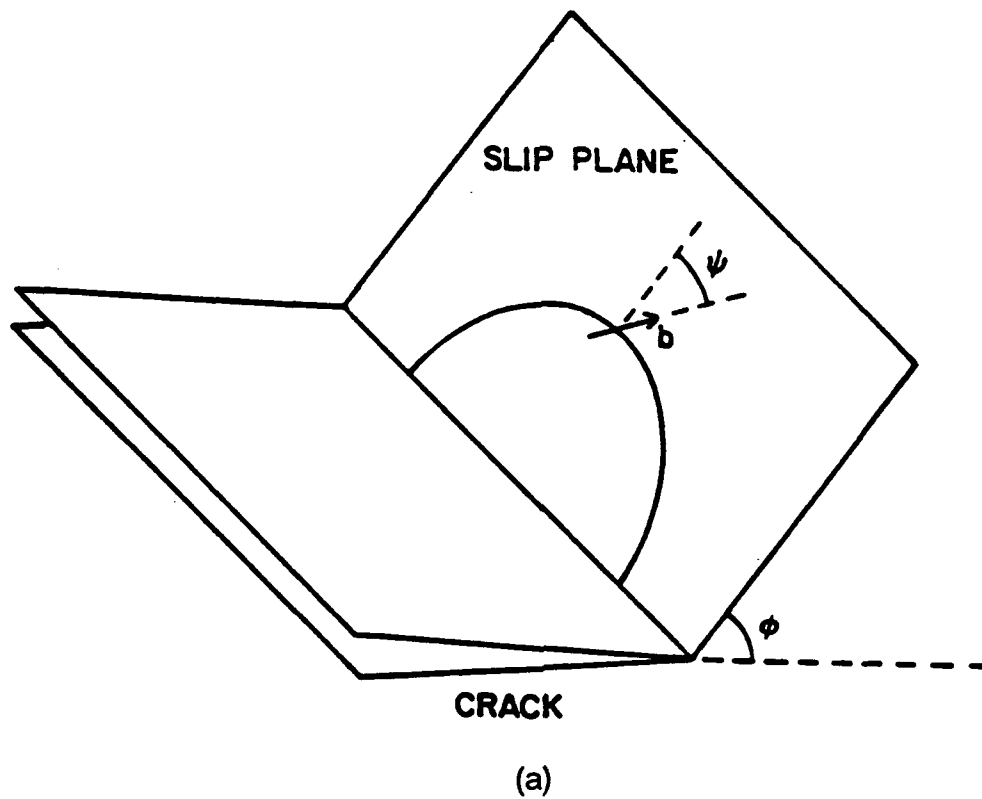
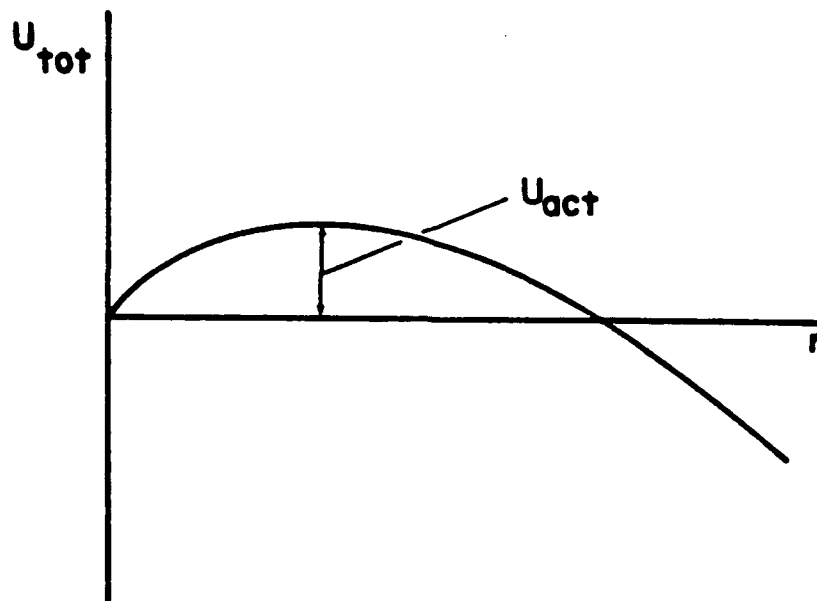
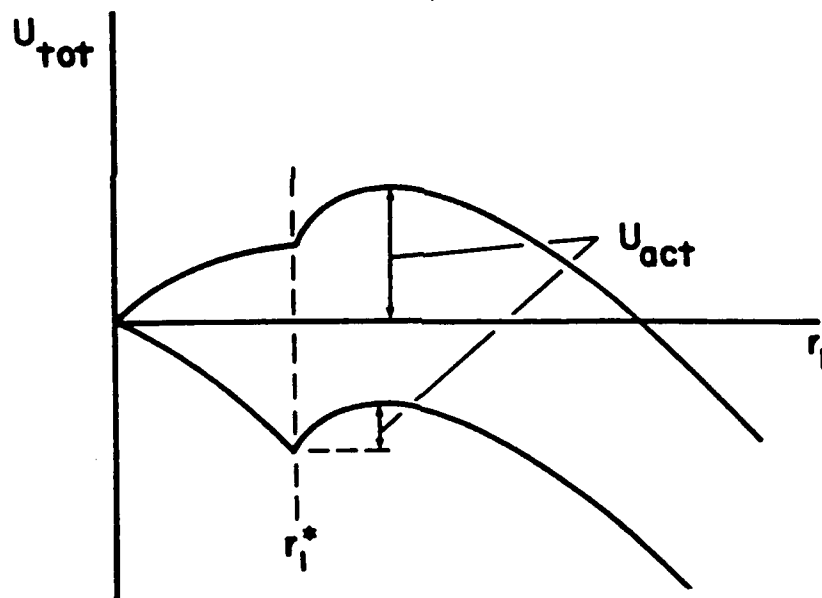


Fig. 1 Crack tip and slip system geometry. a. Geometry of a dislocation half loop emitted from a crack tip. b. Geometry of a dissociated superlattice dislocation on the slip plane.

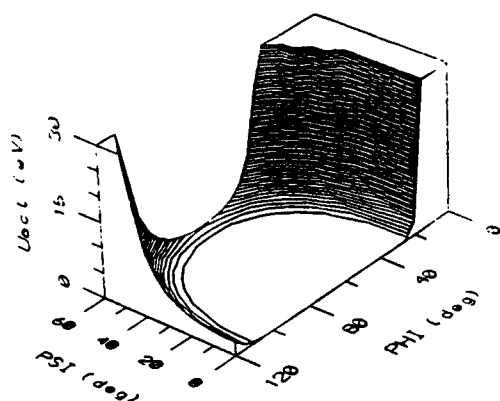


(a)

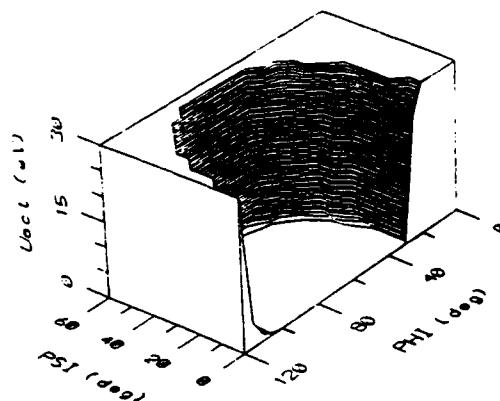


(b)

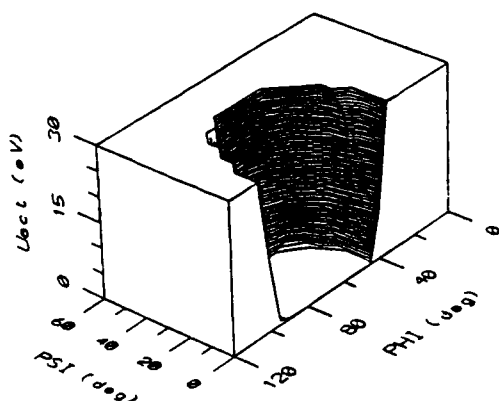
Fig. 2 Schematic representation of the total energy of a superlattice dislocation emitted from a crack tip as a function of dislocation half loop radius. a. Energy barrier for emission of an undissociated superlattice dislocation. b. Two types of energy barrier for emission of a dissociated superlattice dislocation. r_1^* represents the radius of the outer superlattice partial dislocation when the inner superlattice partial dislocation is emitted.



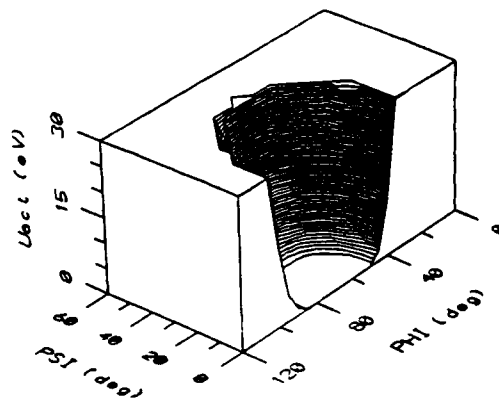
(a)



(b)

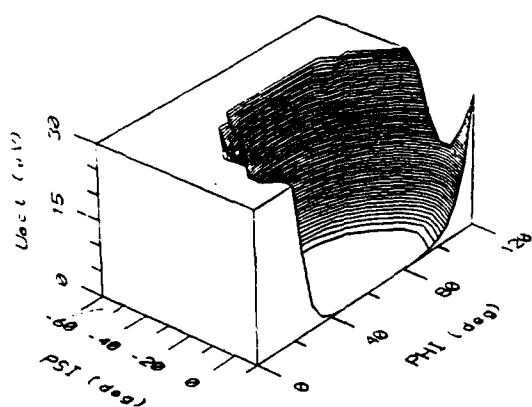


(c)

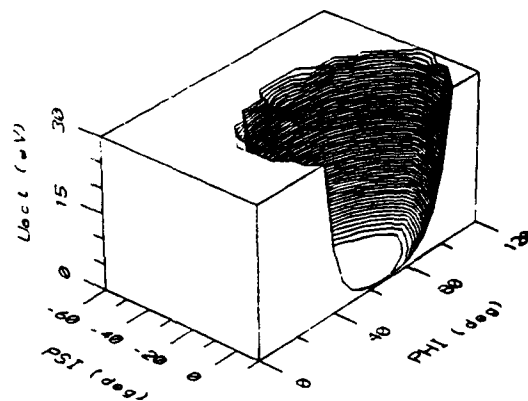


(d)

Fig. 3 Activation energy for emission of a dissociated superlattice dislocation as a function of slip system orientation in several $L1_2$ intermetallic alloys exhibiting APB-type dissociation. a. Cu_3Au . b. Ni_3Al . c. Al_3Sc d. $\text{Al}_{67}\text{Ni}_8\text{Ti}_{25}$.



(a)



(b)

Fig. 4 Activation energy for emission of a dissociated superlattice dislocation as a function of slip system orientation in two $L1_2$ intermetallic alloys exhibiting SISF-type dissociation. a. Zr_3Al . b. $Al_{66}Fe_6Ti_{23}V_5$. In this figure, the psi (ψ) axis of the plots represents ψ_S which represents the Burgers vector orientation of the superlattice dislocation.

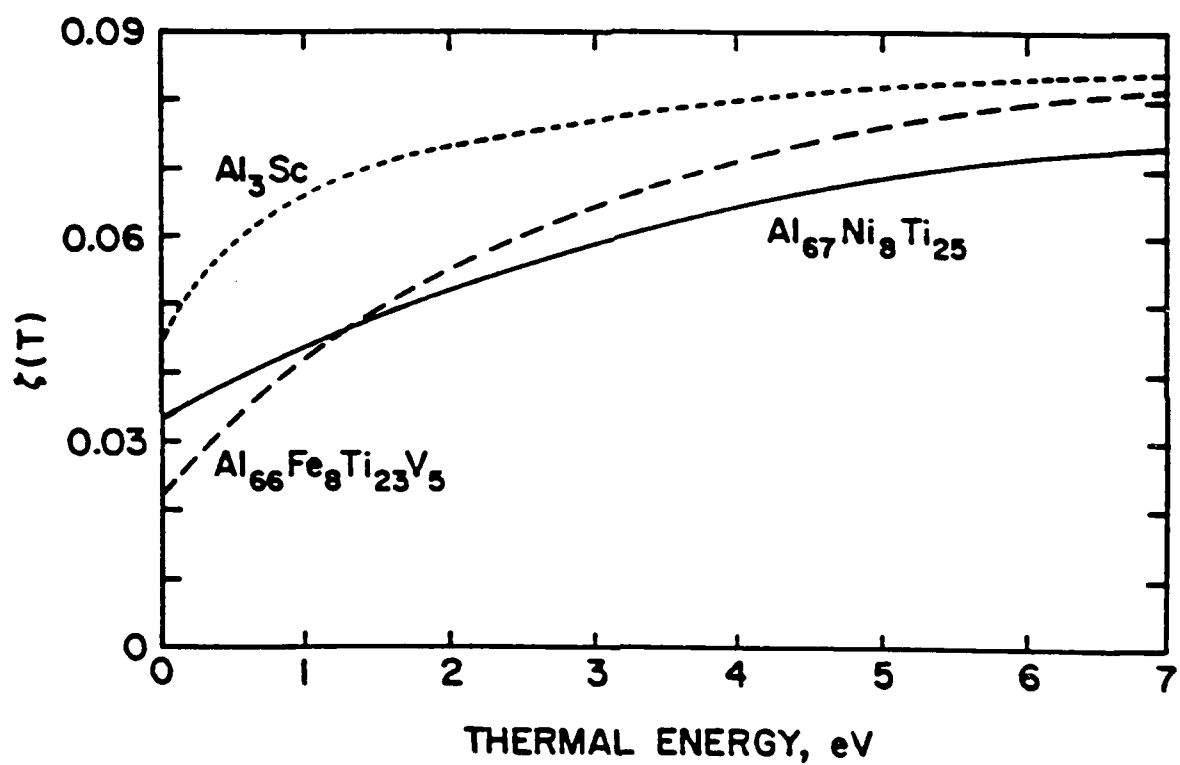


Fig. 5 Effect of thermal energy on the fractional angular range for spontaneous or thermally-activated dislocation emission, $\zeta(T)$, in several L1₂ intermetallic alloys.

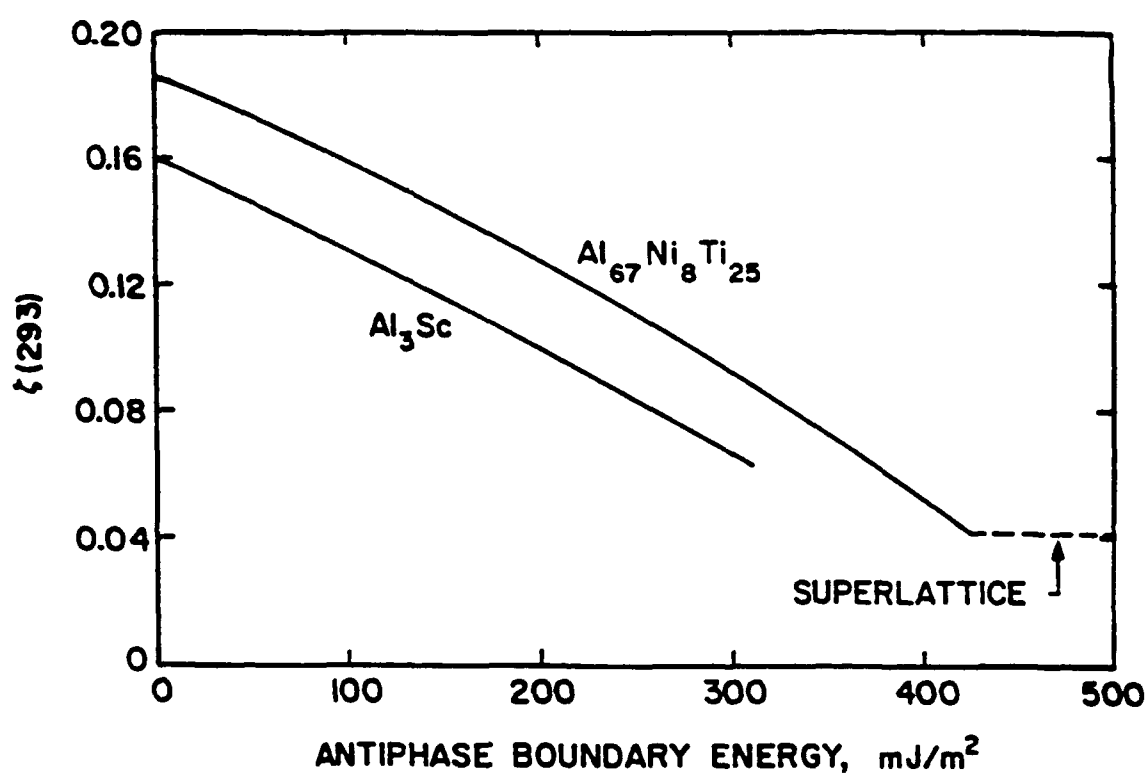


Fig. 6 Effect of $\{111\}$ APB energy on the fractional angular range for spontaneous emission, $\zeta(293)$, in $\text{Al}_{67}\text{Ti}_8\text{Ti}_{25}$ and Al_3Sc .

Published in *J. Mater. Res.*, 7 (1992) 919.

Modeling of Crack Tip Dislocation Emission in B2 Intermetallic Alloys

Michael F. Bartholomeusz and John A. Wert

Department of Materials Science

University of Virginia

Charlottesville, VA 22901

Abstract

A model has been previously proposed to describe the energy associated with emission of dissociated superlattice dislocations from crack tips in ordered intermetallic alloys. In the present paper, the model is applied to several B2 intermetallic alloys. The results of the analysis reveal a correlation between the range of slip system orientations for which emission of a dislocation from a crack tip is energetically favorable, and the macroscopic fracture mode of the alloy. Additionally, the effects of changing the active slip system, increasing the thermal energy available for thermally-activated dislocation emission, and changing the $\{111\}$ APB energy on the fracture mode of NiAl and FeAl are discussed.

1. Introduction

Brittle fracture at ambient temperatures in intermetallic alloys with the B2 crystal structure can occur by grain boundary separation or by transgranular cleavage. Previous investigators have attributed brittle fracture in B2 intermetallic alloys to environmental effects, impurity segregation to grain boundaries, poor grain boundary cohesion and violation of the compatibility requirement for polycrystalline deformation.¹⁻⁴ Intergranular fracture in B2 intermetallic alloys has been extensively studied. In some cases, intergranular fracture can be controlled by alloying additions, such as boron additions to Fe-40Al.⁴ The boron segregates to grain boundaries where it is thought to enhance grain boundary cohesion. The compatibility problem arises because the room temperature slip vector of many B2 intermetallic alloys is $\langle 100 \rangle$, which does not provide enough independent slip systems for generalized plastic flow of a polycrystalline aggregate.³ The problem of compatibility can be remedied by changing the slip vector. For example, Cr is known to promote $\langle 111 \rangle$ slip in NiAl; but an associated increase in tensile ductility has not been observed.⁵ This suggests that compatibility is a necessary, but not sufficient, condition for ductile fracture in this particular alloy. Grain refinement has been found to inhibit brittle fracture in some B2 intermetallic alloys. It has been proposed that below a critical grain size the stress required to nucleate cracks is less than the stress necessary to propagate them.^{3,6}

In contrast to grain boundary fracture, the causes of cleavage fracture in B2 intermetallic alloys are poorly understood. As with other ordered intermetallic alloys, B2 intermetallic alloys generally have low to moderate CRSS (less than $G/100$), suggesting that inhibition of crack tip plasticity due to restriction of slip is not a supportable explanation for cleavage fracture in these materials. Rice and Thomson⁷ proposed a general model that could potentially explain cleavage fracture in B2 intermetallic alloys. In their model they consider the presence of an atomistically sharp crack in a material under uniaxial stress, and determine if it is energetically more favorable for crack extension or crack tip blunting to occur. Crack extension results in cleavage fracture while crack tip blunting leads to ductile fracture, independent of CRSS. In the original Rice and Thomson model, crack tip blunting is accomplished by the emission of a perfect dislocation half loop from the crack tip.

Turner, Powers and Wert⁸ applied the Rice and Thomson model to $L1_2$ intermetallic alloys with dissociated dislocations by considering two limiting cases: high

fault energy, corresponding to emission of a perfect superlattice dislocation; and low fault energy, corresponding to emission of a single superlattice partial dislocation with a trailing fault. These limiting-case analyses revealed that dissociated superlattice dislocations were readily emitted resulting in crack tip plasticity, whereas emission of undissociated superlattice dislocations was unfavorable. Subsequently, the predictions of Turner and coworkers were shown to be inconsistent with experimental observations of cleavage fracture in several $L1_2$ intermetallic alloys which possess dissociated superlattice dislocations.⁹ Bartholomeusz and Wert¹⁰ extended the Rice and Thomson model to deal explicitly with the emission of dissociated dislocations from crack tips. The results of their model were completely consistent with the observed fracture modes of the $L1_2$ intermetallic alloys for which sufficient data existed to apply the model. Bartholomeusz and Wert also used their model to examine thermally-activated dislocation emission, as well as the effect of altering the $\{111\}$ APB energy, on the fracture mode of various intermetallic alloys with the $L1_2$ crystal structure.

The objective of this paper is to present an application of the model to crack tip emission of dissociated superlattice dislocations in intermetallic alloys with the B2 crystal structure. The model is used to examine the effects of temperature and variations in material characteristics on the fracture mode of this class of materials. We consider only brittle fracture by cleavage due to a lack of crack tip plasticity, neglecting the other forms of brittle fracture mentioned earlier in the introduction.

2. Model

In their model Rice and Thomson⁷ evaluate the total energy change at the crack tip associated with emission of a semi-circular dislocation half loop. The total energy is comprised of three distinct terms; the self, ledge and stress energies. The self energy term describes the strain energy of the dislocation line, the interaction energy between all segments of the loop, and accounts for the presence of a free surface. The ledge energy results from the creation of new free surface at the crack tip as the dislocation half loop expands. The stress energy term is the energy reduction associated with partial relaxation of elastic strain energy when the dislocation half loop expands in the stress field of the crack tip. The stress field associated with the crack is assumed to result from mode I loading, and the critical stress intensity is chosen as that which would lead to cleavage fracture in the absence of crack blunting.⁷ The total energy of the dislocation half loop, U_{tot} , is a function of the half loop radius. If U_{tot} increases

before monotonically decreasing, an energy barrier exists for the emission of a perfect dislocation half loop. This energy barrier, which represents the maximum value of U_{tot} , is an activation energy for dislocation emission, U_{act} . If U_{act} is greater than 0, crack extension occurs and the material is considered to fail by brittle cleavage. If U_{tot} monotonically decreases ($U_{\text{act}} = 0$), emission of a dislocation half loop from the crack tip occurs spontaneously and crack tip blunting is favored over crack extension. This model has been shown to be consistent with the observed fracture mode in a wide variety of metallic, ionic, and ceramic materials.^{7,11}

In the case of ordered intermetallic alloys, the Rice and Thomson model can be rigorously applied to those materials that possess perfect superlattice dislocations.⁸ However, in many ordered intermetallic alloys, superlattice dislocations are dissociated into superlattice partial dislocations coupled by a stacking fault or antiphase boundary. Bartholomeusz and Wert¹⁰ extended the Rice and Thomson model to accommodate emission of dissociated superlattice dislocations from crack tips in $L1_2$ intermetallic alloys. The dissociation of dislocations introduces two additional energy contributions to the total energy function: the energy associated with elastic interaction between the two superlattice partial dislocation half loops,¹² and the energy of the associated stacking fault.¹³ In their model, Bartholomeusz and Wert determine U_{act} numerically by evaluating U_{tot} as a function of the distance ahead of the crack tip of the outer superlattice partial dislocation. The position of the inner superlattice partial dislocation is related to that of the outer superlattice partial dislocation through a constraint that the force per unit length acting on both dislocations be the same. As in the case of the original model, a finite value of U_{act} implies crack extension by cleavage, whereas crack tip blunting occurs for $U_{\text{act}} = 0$. For a detailed description of this model and of the equations used, refer to the previous paper by Bartholomeusz and Wert.¹⁰

The primary mechanism of room temperature plastic deformation in B2 intermetallic alloys is glide of $\langle 100 \rangle \{001\}$, $\langle 100 \rangle \{011\}$, $\langle 1\bar{1}1 \rangle \{011\}$, $\langle 11\bar{1} \rangle \{112\}$ or $\langle 11\bar{1} \rangle \{123\}$ superlattice dislocations.^{3,14,15} While observations of dissociated dislocations in B2 intermetallic alloys are not as prevalent as in the case of $L1_2$ intermetallic alloys, APB-dissociated $\langle 111 \rangle$ superlattice dislocations have been reported for several B2 intermetallic alloys.^{16,17} This is consistent with calculations described by Yamaguchi et al.¹⁸ showing that APB dissociation is the only stable dissociated superlattice dislocation configuration in alloys with the B2 crystal structure. The model developed by Bartholomeusz and Wert¹⁰ can be directly applied to the

problem of analyzing emission of superlattice or APB-dissociated superlattice partial dislocations in B2 intermetallic alloys. In the next section we present the results of this analysis.

3. Results

U_{tot} is a function of five material and two geometrical parameters. The material parameters are: shear modulus, G ; Burgers vector, b ; true fracture surface energy, γ ; Poisson's ratio, ν ; and stacking fault energy, Γ . The two geometrical parameters, ϕ and ψ_s , describe the slip plane and Burgers vector orientations relative to the crack, as defined in Figure 1. For fixed values of these parameters, U_{act} is determined numerically, as mentioned previously. For a given material, it is possible to determine U_{act} as a function of ϕ and ψ_s , the parameters describing the slip system orientation relative to the crack tip. Variation of ϕ and ψ_s accounts for the variety of grain orientations encountered along a crack front.

The material constants for twelve B2 intermetallic alloys are listed in Table I. In the case of the shear modulus, an average value of G resolved on the respective slip planes of the materials within the scope of this study is used.^{11,19} Elasticity calculations revealed that the average value of G on $\{011\}$, $\{112\}$, and $\{123\}$ planes is the same, but the average value of G on $\{001\}$ planes is somewhat higher when the Zener anisotropy coefficient,²⁰ A_z , is greater than 1. For the B2 intermetallic alloys included in the present investigation, A_z is greater than 1 in all cases. Dislocation emission on the $\langle 100 \rangle \{001\}$ slip system is less favorable than on the $\langle 100 \rangle \{011\}$ slip system due to the higher shear modulus on $\{001\}$ planes. When the model is applied to B2 intermetallic alloys that exhibit $\langle 100 \rangle$ slip, the average shear modulus on $\{011\}$ planes is used. This represents the most favorable condition for dislocation emission in B2 intermetallic alloys possessing a $\langle 100 \rangle$ slip vector. We were unable to find reported values for the anisotropic elastic constants of CoAl in the literature, so we estimated its resolved shear modulus by assuming an anisotropy coefficient equal to that of NiAl.²¹

The free surface energy has not been experimentally determined for any intermetallic alloy. Consequently, γ has been estimated using a method described by Reynolds et al.²² which relates the free surface energy of an elemental metal to its melting temperature and interatomic spacing. To extrapolate the value of free surface

energy from the material's melting temperature to room temperature, an approximate temperature dependence factor was employed.^{10,23}

Figure 2 shows the results of our calculation for four B2 intermetallic alloys. Figures 2a and 2b represent the emission of APB-dissociated superlattice dislocations for CuZn and Fe-40Al. Figures 2c and 2d represent the emission of $\langle 100 \rangle$ and $\langle 111 \rangle$ superlattice dislocations for NiAl and CoAl, respectively. The vertical axis of the plots represents the activation energy for dislocation emission. The two horizontal axes represent slip system orientations relative to the crack tip. Only the positive ranges of ϕ and ψ_s are represented in the plots, since U_{act} is symmetric for positive and negative values of these variables in both the superlattice and APB-dissociated superlattice dislocation cases. The plateau at 30 electron-volts (eV) is a suitable cut-off for the purpose of representing the numerical results. The plateau at 1 eV (shaded region) represents the range of slip system orientations for which spontaneous or thermally-activated emission occurs at room temperature (293 K). We assume that at room temperature, there is enough thermal energy available to the dislocation half loop to overcome an energy barrier of 1 eV.¹⁰ This corresponds approximately to the total thermal energy of the atoms in a dislocation core $10b$ in length.

4. Discussion

4.1 Correlation between spontaneous emission of superlattice dislocations and fracture mode

The parameter $\zeta(293)$, as first introduced by Bartholomeusz and Wert,¹⁰ describes the fractional angular ranges of ϕ and ψ_s corresponding to spontaneous or thermally-activated emission of dislocations at room temperature for a given material. *Fractional* implies the solid angle range for which emission is favorable, normalized by the solid angle range of all possible orientations of a superlattice dislocation lying on a slip plane that contains the crack tip. This normalization factor encompasses a ϕ range from -180° to $+180^\circ$ and a ψ_s range from -90° to $+90^\circ$.

Table II shows the calculated values of $\zeta(293)$ for the B2 intermetallic alloys studied. The experimentally-determined fracture mode is also listed for some of the B2 alloys in Table II. For the B2 alloys that exhibit $\langle 100 \rangle$ slip, it is necessary to list the single crystal fracture mode, since polycrystalline samples of these alloys can suffer from intergranular fracture as a result of violation of the compatibility requirement. In the

previous paper describing dissociated dislocation emission in $L1_2$ intermetallic alloys, it was proposed that materials having a value of $\zeta(293)$ greater than 0.08 fracture in a ductile fashion.¹⁰ This suggests that spontaneous or thermally-activated emission of dislocations must occur over a range of slip system orientations greater than some critical range for a material to exhibit macroscopically-ductile fracture. The results for the B2 intermetallic alloys (Table II) are consistent with this. No physical significance is attached to the value of $\zeta(293) = 0.08$, since only slip planes which contain the crack tip are considered in the analysis.

A considerable research undertaking has been devoted to promotion of $\langle 111 \rangle$ slip in NiAl.^{5,24} The objective of this research has been to overcome the lack of compatibility associated with $\langle 100 \rangle$ slip, which was presumed to restrict ductility in this material. Results of the present investigation indicate that changing the active slip system from $\langle 100 \rangle \{011\}$ to $\langle 1\bar{1}1 \rangle \{011\}$ in NiAl significantly reduces the value of $\zeta(293)$. The model suggests that changing the slip vector in NiAl cannot achieve the desired result of improving ductility. Although compatibility is satisfied for $\langle 111 \rangle$ slip, there are no $\langle 1\bar{1}1 \rangle \{011\}$ slip system orientations that favor spontaneous or thermally-activated emission of superlattice dislocations from a crack tip.

4.2 Thermal effects

In defining $\zeta(293)$, it was proposed that 1 eV of thermal energy associated with the core atoms of a dislocation at room temperature enables the dislocation to overcome energy barriers smaller than 1 eV. At higher temperatures, more thermal energy is available and the value of $\zeta(T)$ increases. The thermal activation of dislocations over a crack tip energy barrier is a possible explanation for the brittle-to-ductile transition observed in many ordered intermetallic alloys.^{10,25} Figures 3a and 3b show the variation of $\zeta(T)$ with available thermal energy for two B2 intermetallic alloys that exhibit cleavage fracture at room temperature, NiAl and Fe-40Al.

In Figure 3a there are two curves for NiAl, representing the slip systems characterized by the $\langle 100 \rangle$ and $\langle 111 \rangle$ slip vectors. When more than 2.5 eV of thermal energy is available, $\zeta(T)$ for NiAl undergoing $\langle 100 \rangle$ slip assumes a value characteristic of materials that exhibit ductile fracture. This suggests that a brittle-to-ductile transition for NiAl $\langle 100 \rangle$ may occur at about 600 K. This is in agreement with the reported observation of a brittle-to-ductile transition temperature for NiAl between

600 and 700 K.^{26,27} Figure 3a shows that no such transition in fracture mode for NiAl undergoing $\langle 111 \rangle$ slip is predicted on the basis of the model. From the nature of the results discussed in this paragraph, it is conceivable that for samples of NiAl undergoing $\langle 111 \rangle$ slip at ambient temperatures, a brittle-to-ductile transition could occur as a consequence of a thermally-induced change in slip vector to $\langle 100 \rangle$. A transition of the slip vector of chromium-modified NiAl from $\langle 111 \rangle$ to $\langle 100 \rangle$ has been observed to take place at about 900 K.⁵

Fe-40Al is reported to deform by $\langle 111 \rangle$ slip. $\zeta(T)$ for undissociated $\langle 111 \rangle$ slip in Fe-40Al is 0 for all temperatures represented in Figure 3, suggesting that a brittle-to-ductile transition cannot occur by thermally-activated emission of $\langle 111 \rangle$ superlattice dislocations from a crack tip. In contrast, $\zeta(T)$ for emission of $\langle 100 \rangle$ superlattice dislocations in Fe-40Al is greater than 0.08 when the available thermal energy exceeds 3.0 eV, which corresponds to about 700 K. The results of the model imply that Fe-40Al may exhibit a brittle-to-ductile transition provided that a slip vector transition from $\langle 111 \rangle$ to $\langle 100 \rangle$ occurs, and the temperature exceeds 700 K. A change in slip vector from $\langle 111 \rangle$ to $\langle 100 \rangle$ accompanied by a brittle-to-ductile transition between 700 and 900 K has been observed for FeAl alloys.²⁸

Figure 3b suggests an alternate mechanism by which thermally activated emission of dislocations can lead to a brittle-to-ductile transition in Fe-40Al: emission of APB-dissociated $\langle 111 \rangle$ dislocations. The APB energy for Fe-40Al can be extrapolated from reported values of APB energies for Fe-Al alloys with aluminum contents ranging from 27 to 37 at. %.¹⁷ Model calculations for Fe-40Al with an APB energy of 133 mJ/m² suggest that emission of APB-dissociated superlattice dislocations would lead to a brittle-to-ductile fracture mode transition at 600 K. Since the brittle-to-ductile transition temperatures for both mechanisms mentioned are similar to the experimentally-observed temperature range, either mechanism could account for the brittle-to-ductile transition in Fe-40Al.

4.3 Effect of APB energy

According to the present model, changes of the five material parameters included in the dislocation emission model (G , ν , Γ , γ , b) can change the value of $\zeta(293)$. Of these five material parameters, the APB energy is most susceptible to manipulation by variation of the chemical composition. Figure 4 shows the effect of varying Γ for the

two B2 intermetallic alloys considered in detail previously. For both of these alloys, the value of $\zeta(293)$ increases with decreasing APB energy.

Figure 4 suggests that APB-dissociation of superlattice dislocations with $\langle 111 \rangle$ slip vectors increases $\zeta(293)$ for NiAl. However, to achieve values of $\zeta(293)$ similar to those associated with ductile fracture in other B2 intermetallic alloys requires reduction of the APB energy to values on the order of 10 mJ/m^2 , far below the calculated value of 810 mJ/m^2 on $\{011\}$ planes.²⁹ Thus, the model results suggest that avoiding cleavage fracture in NiAl at room temperature requires both altering the slip vector to ensure compatibility and drastically lowering the APB energy to solve the crack tip dislocation emission problem.

The APB energies of dissociated superlattice dislocations have been reported for FeAl alloys over a fairly large range of composition. Crawford et al.¹⁶ found that the APB energy varies linearly from 28 mJ/m^2 for Fe-27Al to 109 mJ/m^2 for Fe-37Al. Studies of fracture characteristics reveal that FeAl alloys with aluminum contents greater than 25 atomic percent fail by brittle cleavage.^{4,28,30-33} Figure 4 demonstrates that the APB energy of Fe-40Al must be reduced to values smaller than 28 mJ/m^2 for $\zeta(293)$ to approach values characteristic of intermetallic alloys that exhibit ductile fracture. As indicated above, one means of lowering the APB energy is reduction of the aluminum content of the alloy. Experimental observation of increased tensile elongation concomitant with a decrease in aluminum content is consistent with the model results.³⁴

5. Conclusions

The results presented in this paper lead to three conclusions relative to cleavage fracture of intermetallic alloys with the B2 crystal structure:

1. For the B2 intermetallic alloys considered in this paper, a correlation has been found between the angular range of slip system orientations for which spontaneous or thermally-activated emission of dislocations occurs and the macroscopic fracture mode.
2. Changing the slip vector of NiAl from $\langle 100 \rangle$ to $\langle 111 \rangle$ to satisfy compatibility has a deleterious effect on the material's ability to undergo crack tip blunting. This is because emission of $\langle 111 \rangle$ superlattice dislocations from crack tips is more difficult than emission of $\langle 100 \rangle$ superlattice dislocations. Thus, changing the slip vector is a

necessary, but not sufficient, condition for ductile fracture of NiAl at ambient temperatures.

3. In NiAl and Fe-40Al, crack tip blunting can be achieved by thermally-activated emission of $\langle 100 \rangle$ superlattice dislocations at elevated temperatures. In contrast, thermally-activated emission of undissociated $\langle 111 \rangle$ superlattice dislocations is energetically unfavorable in these two intermetallic alloys at all temperatures investigated. Model results also show that APB-dissociated $\langle 111 \rangle$ dislocations, observed in FeAl alloys, are more readily emitted than undissociated $\langle 111 \rangle$ dislocations in Fe-40Al.

6. Acknowledgements

The authors are grateful to Dr. K.M. Chang for his thoughtful contributions. This work was sponsored by AFOSR under contract number AFOSR-90-0143; Dr. A. Rosenstein was the contract monitor.

7. References

1. N.S. Stoloff, in *High Temperature Ordered Intermetallic Alloys*, edited by C.C. Koch, C.T. Liu and N.S. Stoloff (Materials Research Society, Pittsburgh, 1985), p. 343.
2. J.A. Wert, "Ordered Intermetallic Alloys for Elevated Temperature Aerospace Applications", (1990), submitted to Monograph on Flight-Vehicle Materials, Structures and Dynamics Technologies - Assessment and Future Directions.
3. I. Baker and P.R. Munroe, in *High Temperature Aluminides & Intermetallics*, edited by S.H. Whang, C.T. Liu, D.P. Pope and J.O. Stiegler (The Minerals, Metals & Materials Society, Warrendale, 1990), p. 425.
4. C.T. Liu and E.P. George, *Scripta Metall.* **24**, 1285 (1990).
5. D.B. Miracle, S. Russell and C.C. Law, in *High Temperature Ordered Intermetallic Alloys III*, edited by C.T. Liu, A.I. Taub, N.S. Stoloff and C.C. Koch (Materials Research Society, Pittsburgh, 1989), p. 225.
6. K.H. Hahn, K. Vedula, *Scripta Metall.* **17**, 7 (1989).
7. J.R. Rice and R. Thomson, *Phil. Mag.* **29**, 73 (1974).
8. C.D. Turner, W.O. Powers and J.A. Wert, *Acta Metall.* **37**, 2635 (1989).
9. E.P. George, J.A. Horton, W.D. Porter and J.H. Schneibel, *J. Materials Research* **5**, 1639 (1990).
10. M.F. Bartholomeusz and J.A. Wert, "Effect of Dislocation Dissociation on Crack Tip Plasticity in $L1_2$ Intermetallic Alloys", accepted for publication in *Acta Metallurgica et Materialia*.
11. S.S. Hecker, D.C. Rohr and D.F. Stein, *Met. Trans.* **9A**, 481 (1978).
12. R.W. Lardner, *Mathematical Expositions* (University of Toronto Press, Toronto, 1974), p. 281.
13. J.S. Wang, P.M. Anderson and J.R. Rice, in *Mechanical Behavior of Materials V*, edited by M.G. Yan, S.H. Zhang and Z.M. Zheng (Pergamon Press, Oxford, 1987), p. 191.
14. D.I. Potter, *Mat. Sci. Eng.* **5**, 201 (1969).
15. E.P. Lautenschlager, T. Hughes and J.O. Brittain, *Acta Metall.* **15**, 1347 (1967).
16. R.C. Crawford and I.L.F. Ray, *Phil. Mag.* **35**, 549 (1977).
17. H. Saka, M. Kawase, A. Nohara and T. Imura, *Phil. Mag.* **50**, 65 (1984).
18. M. Yamaguchi, D.P. Pope, V. Vitek and Y. Umakoshi, *Phil. Mag.* **43**, 1265 (1981).
19. J. Turley and G. Sines, *J. Phys. D: Appl. Phys.* **4**, 264 (1971).
20. G. Grimvall, *Thermophysical Properties of Materials* (North-Holland, Amsterdam, 1986), p. 30.

21. G. Simmons and H. Wang, *Single Crystal Elastic Constants and Calculated Aggregate Properties: A Handbook* (The M.I.T. Press, Massachusetts, 1971).
22. C.L. Reynolds, P.R. Couchmand and F.E Karasz, *Phil. Mag.* **34**, 659 (1976).
23. L.E. Murr, *Interfacial Phenomena in Metals and Alloys* (Addison-Wesley, Reading, 1975), p. 122.
24. R. Darolia, D.F. Lahrman, R.D. Field and A.J. Freeman in *High Temperature Ordered Intermetallic Alloys III*, edited by C.T. Liu, A.I. Taub, N.S. Stoloff and C.C. Koch (The Materials Research Society, Pittsburgh, 1989), p. 113.
25. K. Vedula and J.R. Stephens in *High Temperature Ordered Intermetallic Alloys II*, edited by N.S. Stoloff, C.C. Koch, C.T. Liu and O. Izumi (Materials Research Society, Pittsburgh, 1987), p. 381.
26. K. Vedula, K.H. Hahn and B. Boulogne in *High Temperature Ordered Intermetallic Alloys III*, edited by C.T. Liu, A.I. Taub, N.S. Stoloff and C.C. Koch (Materials Research Society, Pittsburgh, 1989), p. 299.
27. R. Darolia, *JOM* **43** (3), 44 (1991).
28. M.G. Mendiratta et al. in *High Temperature Ordered Intermetallic Alloys II*, edited by N.S. Stoloff, C.C. Koch, C.T. Liu and O. Izumi (Materials Research Society, Pittsburgh, 1987), p. 393.
29. C.L. Fu and M.H. Yoo in *High Temperature Ordered Intermetallic Alloys IV*, edited by L.A. Johnson, D.P. Pope and J.O. Stiegler (Materials Research Society, Pittsburgh, 1991), p. 667.
30. K.M. Chang and R.A. Rosa, *Cleavage Behavior of Intermetallic Fe-40Al Single Crystals* (General Electric Technical Report Class 1, 1990).
31. C.T. Liu, J.G. McCaney and E.H. Lee, *Scripta Metall.* **24**, 385 (1990).
32. W.R. Kerr, *Met. Trans.* **17A**, 2298 (1986).
33. C.G. McCaney and J.A. Horton, *Met. Trans.* **20A**, 751 (1989).
34. C.T. Liu and E.P. George in *High Temperature Ordered Intermetallic Alloys IV*, edited by L.A. Johnson, D.P. Pope and J.O. Stiegler (Materials Research Society, Pittsburgh, 1991), p. 527.
35. P. Villars and L.D. Calvert, *Pearson's Handbook of Crystallographic Data for Intermetallic Phases* (American Society for Metals, Metals Park, 1985).
36. M.G. Mendiratta, H.K. Kim and H.A. Lipsitt, *Met. Trans.* **15A**, 395 (1984).
37. B. Verlinden and L. Delaey, *Acta Metall.* **36**, 1771 (1988).
38. W.G. Moffatt, *The Handbook of Binary Phase Diagrams* (Genium Publishing Co., Schenectady, 1987).
39. K. Murakami, Y. Umakoshi and M. Yamaguchi, *Phil. Mag.* **37**, 719 (1978).

40. Y. Murakami and S. Kachi, J. Phys. Soc. Japan **37**, 1475 (1974).
41. R.V. Krishnan and L.C. Brown, Phys. Stat. Sol. **12**, k35 (1972).
42. M.R. Harmouche and A. Wolfenden, in *High Temperature Ordered Intermetallic Alloys*, edited by C.C. Koch, C.T. Liu and N.S. Stoloff (Materials Research Society, Pittsburgh, 1985), p. 343.
43. S. Zirinsky, Acta Metall. **4**, 164 (1956).
44. H. Yasuda, T. Takasugi and M. Koiwa, Met. Trans. J.I.M. **32**, 48 (1991).
45. T. Takasugi, M. Yoshida and T. Kawabata, *The Effect of Temperature and Orientation on Dislocation Microstructures in B2-Type CoTi Single Crystals*, accepted for publication in Phil. Mag.
46. R.J. Wasiewski, Trans. A.I.M.E. **236**, 455 (1966).
47. R.J. Schiltz, T.S. Prevender and J.F. Smith, J. Appl. Phys. **42**, 4680 (1971).
48. E.M. Schulson and E. Teghtsoonian, Phil. Mag. **37**, 155 (1969).
49. M.M. Shea and N.S. Stoloff, Met. Trans. **5A**, 755 (1974).
50. J.B. Mitchell, O. Abo-El-Fotah and J.E. Dorn, Met. Trans. **2A**, 3265 (1971).
51. E.A. Dwight, Trans. A.I.M.E. **215**, 283 (1959).
52. T. Takasugi, O. Izumi and M. Yoshida, Journal of Material Science **26**, 2941 (1991).

Table I. Material Parameters for the B2 Intermetallic Alloys Considered in the Present Investigation

Material	G GPa	K GPa	a_0 nm	γ J/m ²	Γ (APB) J/m ²	Slip	Refs. (300 K) ^d
AuCd	7	85	0.331	1.6		<100>	43,43,14,14,3
CuZn	17	116	0.295	2.0	0.050 ^c	<111>	37,37,14,38,3,3
AuZn	14	132	0.313	1.8		<100>	47,47,14,38,48
Fe-40Al	53	136	0.291	2.7	0.133 ^b	<111>	21,21,35,25,3,36
NiAl	52	166	0.289	3.0		<100>	46,46,14,25,24
AgCd	8	90	0.333	1.6		<111>	28,28,12,42,37
AgZn	14	94	0.316	1.7		<111>	40,40,35,35,41
CoTi	48	154	0.230	2.3		<100>	44,44,35,38,45
AgMg	21	66	0.332	1.8		<111>	21,21,35,38,39
CoAl	72 ^a	109	0.286	3.1		<111>	42,42,35,38,43

^a Estimated value on the slip plane.

^b The value of γ for Fe-40Al is extrapolated from reported values of the APB energy as a function of composition for the Fe-Al system. Γ for Fe-35Al is 0.093 mJ/m².

^c This is the value of the APB energy on the {011} plane. Γ has a slightly lower value of 37 mJ/m² on the {112} plane.

^d References listed in same order as parameters in Table.

Table II. Correlation Between $\zeta(293)$ and Fracture Mode for the B2 Intermetallic Alloys Considered in the Present Investigation.

Material and dislocation dissociation mode		$\zeta(293)$	Fracture mode	Ref.
AuCd		0.168	-	
CuZn	APB{112}	0.161	Ductile	49
CuZn	APB{011}	0.154	Ductile	49
AuZn		0.137	-	
Fe-37Al	APB	0.037	Brittle	31
Fe-40Al	APB	0.029	Brittle	30
Fe-40Al		0	Brittle	30
NiAl<100>		0.025	Brittle	27
NiAl<111>		0	-	
AgCd		0.020	-	
AgZn		0.005	-	
CoTi		0.004	Brittle	52
AgMg		0	Brittle	50
CoAl		0	Brittle	51

List of Figures

Fig. 1 Crack tip and slip system geometry.

Fig. 2 Activation energy for emission of a superlattice or APB-dissociated superlattice dislocation as a function of slip system orientation in several B2 intermetallic alloys. a. CuZn. b. Fe-40Al. c. NiAl d. CoAl.

Fig. 3 Effect of thermal energy on the fractional angular range for spontaneous or thermally-activated dislocation emission, $\zeta(T)$, in two B2 intermetallic alloys: a. NiAl b. Fe-40Al.

Fig. 4 Effect of APB energy on the fractional angular range for spontaneous emission at room temperature, $\zeta(293)$, in NiAl and Fe-40Al.

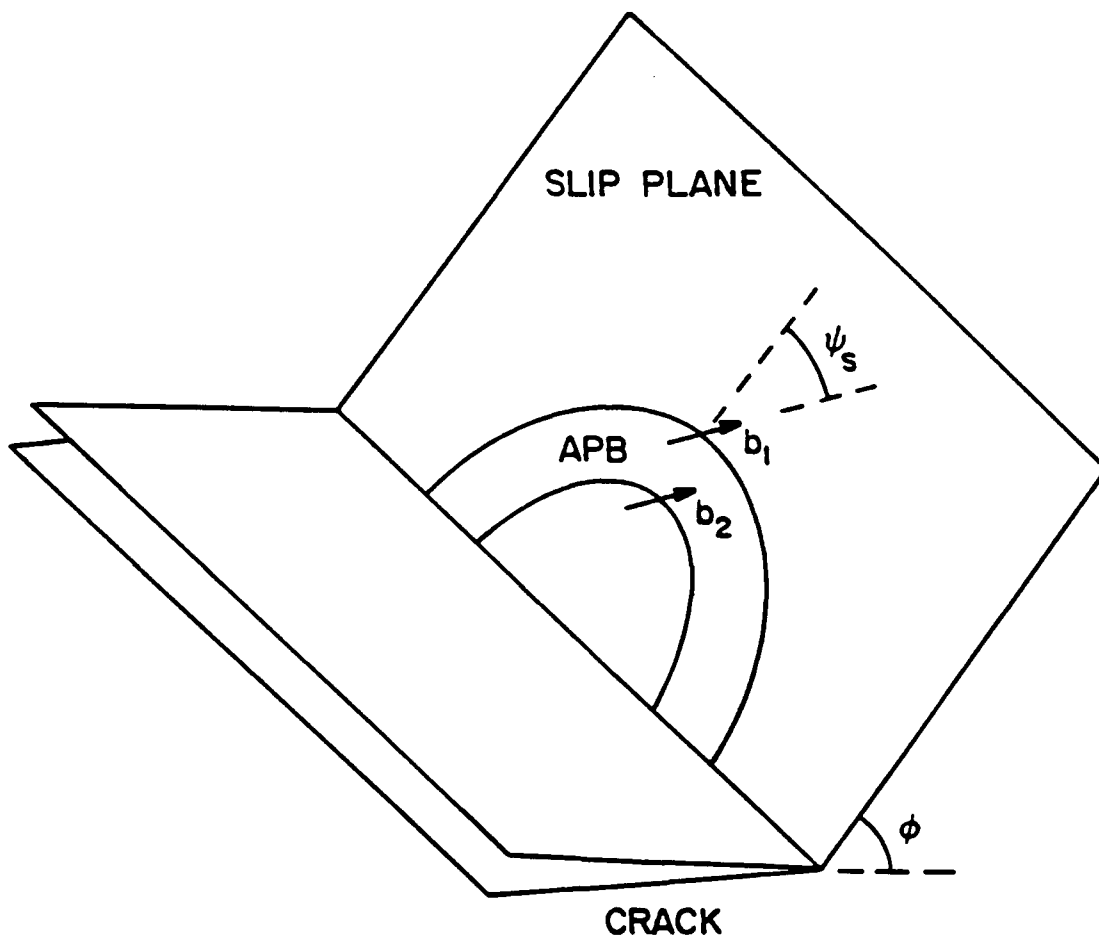
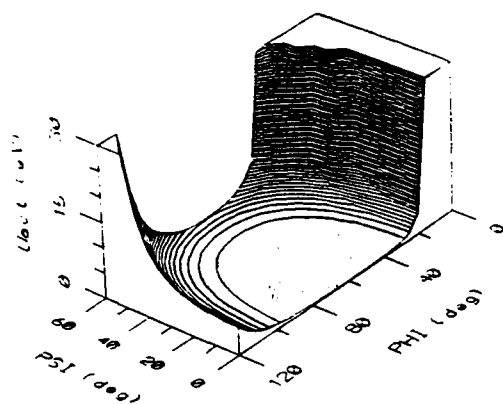
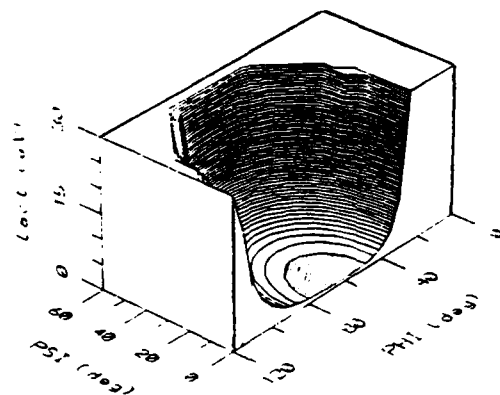


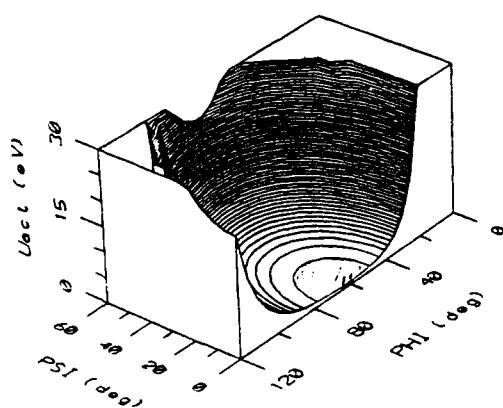
Fig. 1 Crack tip and slip system geometry.



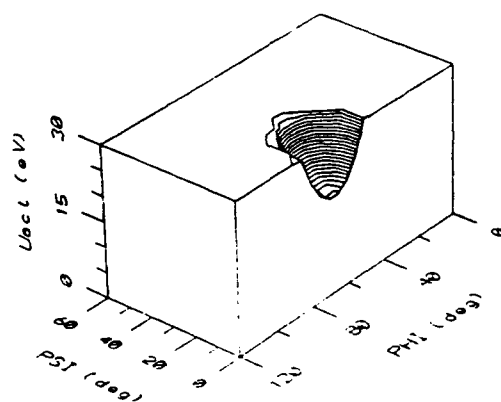
(a)



(b)

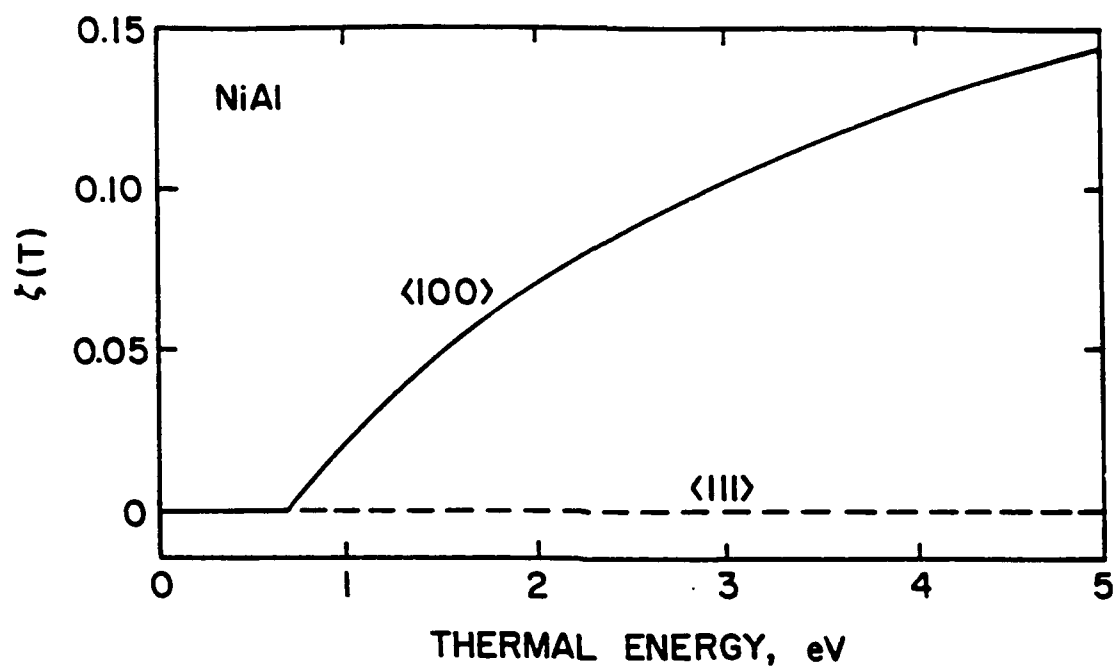


(c)

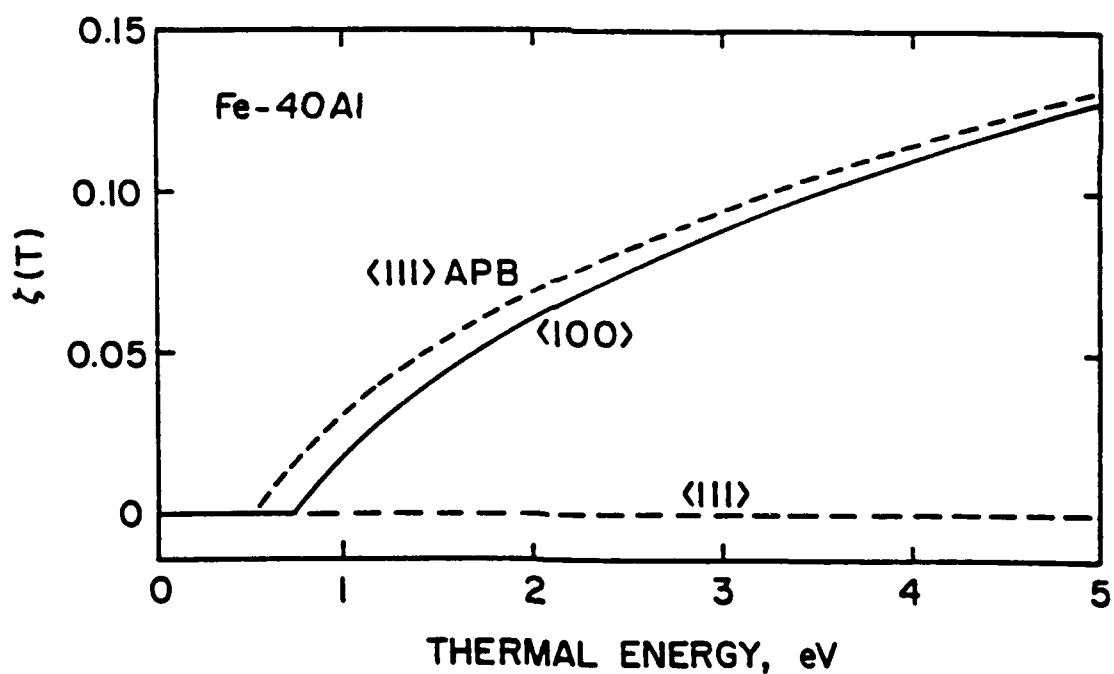


(d)

Fig. 2 Activation energy for emission of a superlattice or APB-dissociated superlattice dislocation as a function of slip system orientation in several B2 intermetallic alloys. a. CuZn. b. Fe-40Al. c. NiAl d. CoAl.



(a)



(b)

Fig. 3 Effect of thermal energy on the fractional angular range for spontaneous or thermally-activated dislocation emission, $\zeta(T)$, in two B2 intermetallic alloys: a. NiAl b. Fe-40Al.

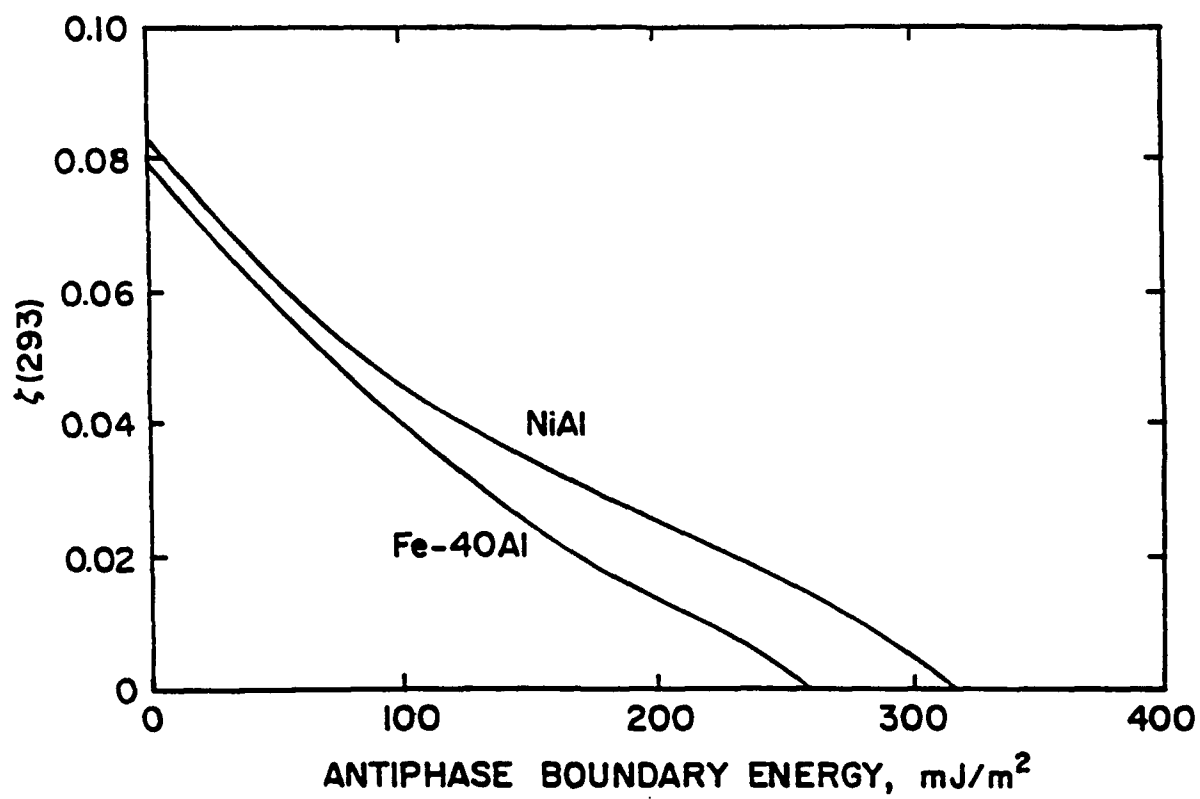


Fig. 4 Effect of APB energy on the fractional angular range for spontaneous emission at room temperature, $\zeta(293)$, in NiAl and Fe-40Al.

Published in *High Temperature Ordered Intermetallic Alloys V*, edited by I. Baker, R. Darolia, J.D. Whittenberger and M.H. Yoo (MRS, Pittsburgh, 1992) 537.

THE EFFECT OF DISLOCATION DISSOCIATION ON CRACK TIP PLASTICITY IN $L1_2$
AND B2 INTERMETALLIC ALLOYS

MICHAEL F. BARTHOLOMEUSZ, WEIGANG MENG AND JOHN A. WERT

Department of Materials Science and Engineering
University of Virginia, Charlottesville, VA 22903

ABSTRACT

Low toughness at ambient temperatures is an inherent problem in many ordered intermetallic alloys that otherwise have attractive properties for high temperature applications. One potential explanation of low toughness is the existence of an energy barrier for crack tip dislocation emission. A model describing the energy associated with emission of a dissociated superlattice dislocation from a crack tip in ordered intermetallic alloys has been formulated. Application of the model to a wide variety of intermetallic alloys with the $L1_2$ and B2 crystal structures has revealed a correlation between the observed macroscopic fracture mode and the calculated range of slip system orientations for which emission of a dissociated superlattice dislocation at ambient temperatures is possible. Additionally, the model has been used to predict the effects of lowering the stacking fault energy, increasing the thermal energy available for thermally activated dislocation emission, and changing the active slip system. Preliminary fractographic analyses have been conducted with a chromium-modified Al_3Ti alloy to verify the model predictions.

1. Introduction and Model

Cleavage fracture in materials possessing a high critical resolved shear stress (CRSS) is relatively easy to understand: the high resistance to slip inhibits crack tip plasticity, resulting in cleavage fracture. However, many intermetallic alloys that fail by cleavage fracture possess low to moderate values of CRSS, requiring an alternate explanation for cleavage fracture. Rice and Thomson (RT) [1] proposed a model for cleavage fracture independent of CRSS in which the Griffith criterion is invoked to determine the critical remote stress required for cleavage fracture. The RT model proposes that cleavage fracture will not occur if it is energetically favorable for an atomistically sharp crack under mode I loading to emit a dislocation at the critical stress. However, if an energy barrier for dislocation emission exists at the crack tip, dislocation emission is inhibited resulting in cleavage fracture.

Bartholomeusz and Wert (BW) [2, 3] extended the RT analysis to treat emission of dissociated superlattice dislocations from crack tips in $L1_2$ and B2 intermetallic alloys. The extended model can be used to examine the effects of temperature and variations of material properties on the emission of superlattice and dissociated superlattice dislocations from crack tips. For a detailed description of the mathematics of the model and a discussion of the material parameters selected, see Refs.[2, 3]. The purpose of the present paper is to describe model results, and place them in the context of available experimental results.

In the case of a dissociated superlattice dislocation, the total energy of the dislocation as a function of distance ahead of the crack tip is dependent on five material and two geometrical parameters. The material parameters are: shear modulus, G ; Burgers vector, b ; true fracture surface energy, γ ; bulk modulus, K ; and stacking fault energy, Γ . Two geometrical parameters are also required: ϕ describes the angle between the slip plane and the crack plane, and ψ_s describes the superlattice Burgers vector orientation relative to the crack. For fixed values of these parameters, the energy barrier for superlattice dislocation emission, U_{act} , is determined numerically. If U_{act} is equal to zero, there is no energy barrier to superlattice dislocation emission, plastic crack blunting occurs and cleavage fracture is averted. For a given material, it is possible to determine U_{act} as a function of ϕ and ψ_s , the parameters describing the slip system orientation relative to the crack tip. Variation of ϕ and ψ_s accounts for the variety of grain orientations encountered along a crack front.

2. Results

The model results for each material in this study can be represented using a plot such as the one shown in Figure 1. The vertical axis of the plot represents the activation energy for dislocation emission. The two horizontal axes represent slip system orientations relative to the crack tip. The plateau at 30 eV is a suitable cut-off for the purpose of representing the numerical results. The plateau at 1 eV (shaded region) represents the range of slip system orientations for which spontaneous or thermally activated dislocation emission can occur at room temperature (293K). We assume that at room temperature, there is enough thermal energy available to the dislocation half loop to overcome an energy barrier of 1 eV. This corresponds approximately to the total thermal energy of the atoms in a dislocation core $10b$ in length.

3. Discussion

3.1 Correlation between spontaneous emission of superlattice dislocations and fracture mode

The parameter $\zeta(293)$, first introduced by BW, describes the fractional angular ranges of ϕ and ψ_s corresponding to spontaneous or thermally activated emission of dislocations at room temperature for a given material. *Fractional* implies the solid angle range for which emission is favorable, normalized by the solid angle range of all possible orientations of a superlattice dislocation lying on a slip plane that contains the crack front. This normalization factor encompasses a ϕ range from -180° to $+180^\circ$ and a ψ_s range from -90° to $+90^\circ$.

Table I shows the calculated values of $\zeta(293)$ for the $L1_2$ and B2 intermetallic alloys studied. The observed dislocation dissociation mode and experimentally-determined single crystal fracture mode are listed for each alloy. Comparing the values of $\zeta(293)$ and the fracture modes listed in Table I reveals a strong correlation. Materials having a value of $\zeta(293)$ greater than 0.08 are resistant to cleavage fracture. This suggests that spontaneous or thermally activated emission of dislocations must occur over a range of slip system orientations greater than some critical range for a material to resist cleavage fracture. We do not attach a physical significance to the value of $\zeta(293) = 0.08$.

3.2 Effect of changing material properties on fracture mode

3.2.1 Effect of changing the Burgers vector

Reducing the magnitude of the Burgers vector renders dislocation emission from a crack tip more energetically favorable. This can be accomplished either by dissociation of superlattice dislocations (as discussed in section 3.2.2) or by a change in slip vector. Analysis of the effect of changing the slip vector on dislocation emission is applicable to B2 intermetallic alloys, since these alloys may deform by either $\langle 100 \rangle$ or $\langle 111 \rangle$ slip [4]. For a given B2 intermetallic alloy, the model results indicate that emission of $\langle 100 \rangle$ dislocations is more favorable than emission of $\langle 111 \rangle$ superlattice dislocations.

A considerable research undertaking has been devoted to promotion of $\langle 111 \rangle$ slip in NiAl [6, 7]. The objective of this research has been to overcome the lack of compatibility associated with $\langle 100 \rangle$ slip, which was presumed to restrict ductility in NiAl. Results of the present investigation indicate that changing the active slip system from $\langle 100 \rangle \{011\}$ to $\langle 1\bar{1}1 \rangle \{011\}$ in NiAl significantly reduces the value of $\zeta(293)$, as shown in Table I. Thus, model results suggest that changing the slip vector in NiAl cannot achieve the desired result of improving ductility. Although compatibility requirements may be satisfied for $\langle 111 \rangle$ slip, spontaneous or thermally activated emission of $\langle 1\bar{1}1 \rangle \{011\}$ superlattice dislocations from a crack tip in NiAl does not occur for any slip system orientations at room temperature.

3.2.2 Effect of changing the stacking fault energy

Figure 2 is a plot of $\zeta(293)$ as a function of fault energy for APB and SISF dissociated superlattice dislocations in $\text{Al}_{67}\text{Ni}_8\text{Ti}_{25}$. This plot suggests that emission of APB coupled superlattice partial dislocations is more energetically favorable than emission of undissociated superlattice dislocations. Lowering the APB energy of $\text{Al}_{67}\text{Ni}_8\text{Ti}_{25}$ below approximately 330 mJ/m^2 would increase $\zeta(293)$ into the range associated with ductile fracture in other L_{12} and B2 intermetallic alloys at room temperature. This implies that lowering the APB energy is a possible means of inducing resistance to cleavage failure in intermetallic alloys at ambient temperatures. In contrast to this, Figure 2 demonstrates that lowering the SISF energy does not have a significant effect on $\zeta(293)$. The different results for APB and SISF dissociated superlattice

dislocations stem from the difference in Burgers vector orientations of the two superlattice partial dislocations in the case of SISF-dissociation.

Although direct evidence for the effect of APB fault energy on fracture mode has not yet been reported, some insight into the correlation between these two factors can be gained by comparing $\text{Al}_{67}\text{Ni}_8\text{Ti}_{25}$ and $\text{Al}_{67}\text{Mn}_8\text{Ti}_{25}$. These alloys have very similar material parameters, except that $\text{Al}_{67}\text{Ni}_8\text{Ti}_{25}$ deforms by glide of undissociated $\langle 1\bar{1}0 \rangle \{111\}$ superlattice dislocations while $\text{Al}_{67}\text{Mn}_8\text{Ti}_{25}$ deforms by glide of APB dissociated superlattice dislocations [8]. From Table I it can be seen that both $\text{Al}_{67}\text{Ni}_8\text{Ti}_{25}$ and $\text{Al}_{67}\text{Mn}_8\text{Ti}_{25}$ have approximately the same value of $\zeta(293)$ for superlattice dislocations. Calculations show that APB dissociation in the case of $\text{Al}_{67}\text{Mn}_8\text{Ti}_{25}$ raises its value of $\zeta(293)$, making it more resistant to cleavage fracture. In support of this, recent results by Mikkola et al. [9] demonstrate that $\text{Al}_{67}\text{Mn}_8\text{Ti}_{25}$ has a significantly higher fracture stress than $\text{Al}_{67}\text{Ni}_8\text{Ti}_{25}$.

3.2.3 Effect of changing the shear and bulk moduli

Pugh [10] proposed that the ratio of the bulk modulus to the shear modulus (K/G) could be used to describe the relationship between the fracture strength and the ease of plastic flow in a material. Resistance to cleavage fracture correlates with increasing values of K/G . The model described in the present paper is consistent with Pugh's criterion. $\zeta(293)$ decreases with increasing values of G and/or decreasing values of K . In the Pugh criterion, however, the fracture mode is equally sensitive to changes in K and G . This dependency is not reflected by the results of our model.

The relative importance of variations of K and G can be illustrated in the case of $\text{Al}_{67}\text{Ni}_8\text{Ti}_{25}$ and $\text{Al}_{67}\text{Cr}_8\text{Ti}_{25}$. $\text{Al}_{67}\text{Cr}_8\text{Ti}_{25}$ has values of shear and bulk modulus that are 7 GPa and 41 GPa lower than those of $\text{Al}_{67}\text{Ni}_8\text{Ti}_{25}$, respectively [5]. Application of the Pugh criterion as mentioned by Mikkola et al. [5], indicates that $\text{Al}_{67}\text{Ni}_8\text{Ti}_{25}$ is less susceptible to cleavage fracture than $\text{Al}_{67}\text{Cr}_8\text{Ti}_{25}$ ($K/G = 1.4$ and 1.0 respectively). However, BW model calculations show that the lower value of shear modulus for $\text{Al}_{67}\text{Cr}_8\text{Ti}_{25}$ offsets its lower bulk modulus and predicts that $\text{Al}_{67}\text{Cr}_8\text{Ti}_{25}$ should be more resistant to cleavage fracture than $\text{Al}_{67}\text{Ni}_8\text{Ti}_{25}$. This prediction is consistent with the previously mentioned report that $\text{Al}_{67}\text{Cr}_8\text{Ti}_{25}$ exhibits a higher fracture stress than $\text{Al}_{67}\text{Ni}_8\text{Ti}_{25}$ [9]. Thus, the dislocation emission model indicates that crack tip plasticity is more sensitive to changes in G than in K .

3.3 Thermal activation effects

In defining $\zeta(293)$, it was proposed that 1 eV of thermal energy associated with the core atoms of a dislocation at room temperature enables the dislocation to overcome energy barriers of 1 eV or less [2]. At higher temperatures, more thermal energy is available and the value of $\zeta(T)$ increases. The thermal activation of dislocations over a crack tip energy barrier is a possible explanation for the change in fracture mode from cleavage to a ductile or intergranular (non-cleavage) mode, as observed in many ordered intermetallic alloys with increasing temperature.

The gradient of the surface represented by contour lines in Figure 1 is related to the potential for significant thermal activation effects. Decreasing steepness of the sides of the activation energy well indicates a greater sensitivity to thermal activation. Within the scope of the present model and the alloy systems studied, three factors found to affect significantly thermally activated dislocation emission are: superlattice dislocation dissociation, shear modulus, and slip system. Examples of the effects of dislocation dissociation and shear modulus on thermally activated dislocation emission are presented below.

Figure 3(a) depicts $\zeta(T)$ as a function of available thermal energy for three $L1_2$ modified Al_3Ti intermetallic alloys. $\zeta(T)$ increases with increasing availability of thermal energy. In the case of $Al_{66}Fe_6Ti_{23}V_5$ and $Al_{67}Cr_8Ti_{25}$, $\zeta(T)$ attains values near 0.08 that are characteristic of $\zeta(293)$ for the $L1_2$ and B2 intermetallic alloys that do not exhibit cleavage fracture at room temperature. This suggests that a transition in fracture mode from cleavage to non-cleavage might occur in $Al_{66}Fe_6Ti_{23}V_5$ near 1100K and in $Al_{67}Cr_8Ti_{25}$ near 800K [2]. For $Al_{67}Ni_8Ti_{25}$, the temperature required to increase $\zeta(T)$ to 0.08 exceeds the melting temperature of the material, suggesting that no fracture mode transition would be observed in this case. Comparison of $Al_{66}Fe_6Ti_{23}V_5$ and $Al_{67}Ni_8Ti_{25}$ shows that both alloys have similar material parameters but $Al_{66}Fe_6Ti_{23}V_5$ has SISF dissociated superlattice dislocations while $Al_{67}Ni_8Ti_{25}$ has undissociated superlattice dislocations [2, 8]. Model calculations show that APB or SISF dissociation of superlattice dislocations reduce the gradient of the activation energy well, compared with that found for undissociated superlattice dislocations. This suggests that superlattice dislocation dissociation renders crack tip emission more sensitive to thermal activation and thus increases the resistance to cleavage fracture at elevated temperatures. The greater susceptibility of $Al_{67}Cr_8Ti_{25}$ to thermally activated

superlattice dislocation emission compared to that of $\text{Al}_{67}\text{Ni}_8\text{Ti}_{25}$ is due to its lower value of shear modulus [5]. If future experimental observations confirm the presence of dissociated superlattice dislocations in $\text{Al}_{67}\text{Cr}_8\text{Ti}_{25}$, this would simply reduce the calculated fracture mode transition temperature.

Figure 3(b) shows the result of fractographic measurements done on the $\text{Al}_{67}\text{Cr}_8\text{Ti}_{25}$ alloy as a function of temperature. There is a clear transition in fracture mode at 800K from transgranular cleavage to intergranular fracture. A correlation between model and experimental results suggests that with increasing temperature the $\text{Al}_{67}\text{Cr}_8\text{Ti}_{25}$ matrix becomes resistant to transgranular cleavage and subsequent failure occurs at the grain boundaries. A future paper will describe detailed analyses of the fracture mode transition in $\text{Al}_{67}\text{Cr}_8\text{Ti}_{25}$ [11].

4. Conclusions

The results presented in this paper can be summarized by a few broad observations that transcend the details of individual intermetallic alloys.

- (1) A correlation exists between the angular range of slip system orientations for which spontaneous or thermally activated emission of dislocations is predicted and the macroscopic fracture mode at room temperature.
- (2) Decreasing the magnitude of the Burgers vector by inducing a change in the slip vector is predicted to enhance a material's ability to exhibit plastic crack blunting.
- (3) For low to moderate values of APB energy, the emission of APB-dissociated superlattice dislocations is always more energetically favorable than the emission of undissociated superlattice dislocations.
- (4) Lowering the APB energy for L1_2 and B2 intermetallic alloys can generate sufficient spontaneous or thermally activated emission of dissociated superlattice dislocations to avoid cleavage fracture at room temperature. In contrast, lowering the SISF energy for L1_2 intermetallic alloys does not have a significant effect on spontaneous or thermally activated superlattice dislocation emission, and is not expected to affect the fracture mode.
- (5) The model predicts that crack tip plasticity is more sensitive to variations in the shear modulus than equivalent variations in the bulk modulus. Reducing the shear modulus increases resistance to cleavage fracture.
- (6) The thermally activated emission of undissociated and dissociated superlattice dislocations from a crack tip with increasing temperature is a possible explanation for a

transition in fracture mode from cleavage to non-cleavage, as observed in many L1₂ and B2 intermetallic alloys.

5. Acknowledgements

This work was sponsored by AFOSR under contract number AFOSR-90-0143; Dr. A. Rosenstein was the contract monitor.

6. References

1. J.R. Rice and R. Thomson, *Phil. Mag.* **29**, 73 (1974).
2. M.F. Bartholomeusz and J.A. Wert, *Acta Metall. et Mater.*, **40**, 673 (1992).
3. M.F. Bartholomeusz and J.A. Wert, *J. Mater. Res.*, **7**, 919 (1992).
4. I. Baker and P.R. Munroe, in *High Temperature Aluminides & Intermetallics*, S.H. Whang, C.T. Liu, D.P. Pope and J.O. Stiegler (eds), MRS, Warrendale, 1990, p. 425.
5. D.E. Mikkola, J.P. Nic, S. Zhang and W.W. Milligan, *ISIJ International*, **31**, 1076 (1991).
6. D.B. Miracle, S. Russell and C.C. Law, in *High Temperature Ordered Intermetallic Alloys III*, C.T. Liu, A.I. Taub, N.S. Stoloff and C.C. Koch (eds), MRS, Pittsburgh, 1989, p. 225.
7. R. Darolia, D.F. Lahrman, R.D. Field and A.J. Freeman in *High Temperature Ordered Intermetallic Alloys III*, C.T. Liu, A.I. Taub, N.S. Stoloff and C.C. Koch (eds), MRS, Pittsburgh, 1989, p. 113.
8. E.P. George, D.P. Pope, C.L. Fu and J.H. Schneibel, *ISIJ International*, **31**, 1063 (1991).
9. J.P. Nic, S. Zhang and D.E. Mikkola, in *High Temperature Ordered Intermetallic Alloys IV*, L.A. Johnson, D.P. Pope and J.O. Stiegler (eds), MRS, Pittsburgh, 1991, p. 697.
10. S.F. Pugh, *Phil. Mag.*, **45**, 823 (1954).
11. W. Meng, M. Vaudin, M.F. Bartholomeusz and J.A. Wert, "Experimental assessment of a fracture mechanism model for an Al₆₇Cr₈Ti₂₇ intermetallic alloy", in preparation.

Table I.

Correlation Between $\zeta(293)$ and Fracture Mode for the $L1_2$ and B2 Intermetallic Alloys Considered in the Present Investigation.

Material and dislocation dissociation mode		$\zeta(293)$	Fracture mode	Alloy system
Cu ₃ Au	APB	0.262	Ductile	$L1_2$
Ni ₃ Al	APB	0.196	Ductile	$L1_2$
Ni ₃ Al	SISF	0.090	Ductile	$L1_2$
Ni ₃ Fe	APB	0.156	Ductile	$L1_2$
Zr ₃ Al	SISF	0.085	Ductile	$L1_2$
Al ₃ Sc	APB	0.069	Brittle	$L1_2$
Al ₆₇ Cr ₈ Ti ₂₅ *		0.049	Brittle	$L1_2$
Al ₆₇ Ni ₈ Ti ₂₅ *	None	0.043	Brittle	$L1_2$
Al ₆₇ Mn ₈ Ti ₂₅ *	APB	0.042	Brittle	$L1_2$
Al ₆₆ Fe ₆ Ti ₂₃ V ₅	SISF	0.042	Brittle	$L1_2$
AuCd		0.168		B2
CuZn	APB{112}	0.161	Ductile	B2
CuZn	APB{011}	0.154	Ductile	B2
AuZn		0.137		B2
Fe-37Al	APB	0.037	Brittle	B2
Fe-40Al	APB	0.029	Brittle	B2
Fe-40Al		0	Brittle	B2
NiAl<100>		0.025	Brittle	B2
NiAl<111>		0		B2
AgCd		0.020		B2
AgZn		0.005		B2
CoTi		0.004	Brittle	B2
AgMg		0	Brittle	B2
CoAl		0	Brittle	B2

* For data on Al₆₇Cr₈Ti₂₅ and Al₆₆Fe₆Ti₂₃V₅ see Ref.[5]. For the sources of the material parameters and fracture modes of all the other alloys listed see Refs. [2, 3].

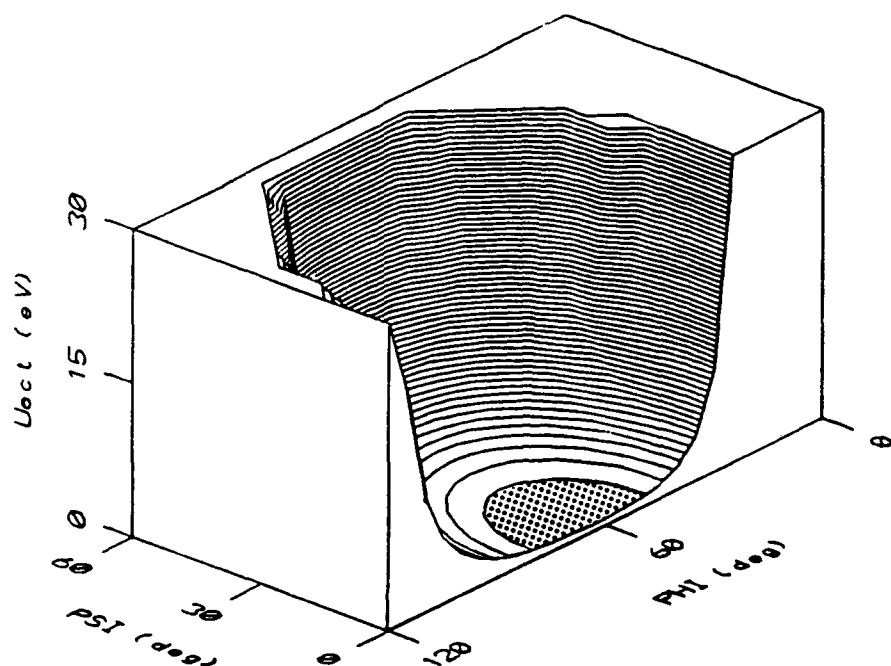


Fig. 1. Activation energy for emission of a dissociated superlattice dislocation as a function of slip system orientation for the B2 intermetallic alloy Fe-40Al.

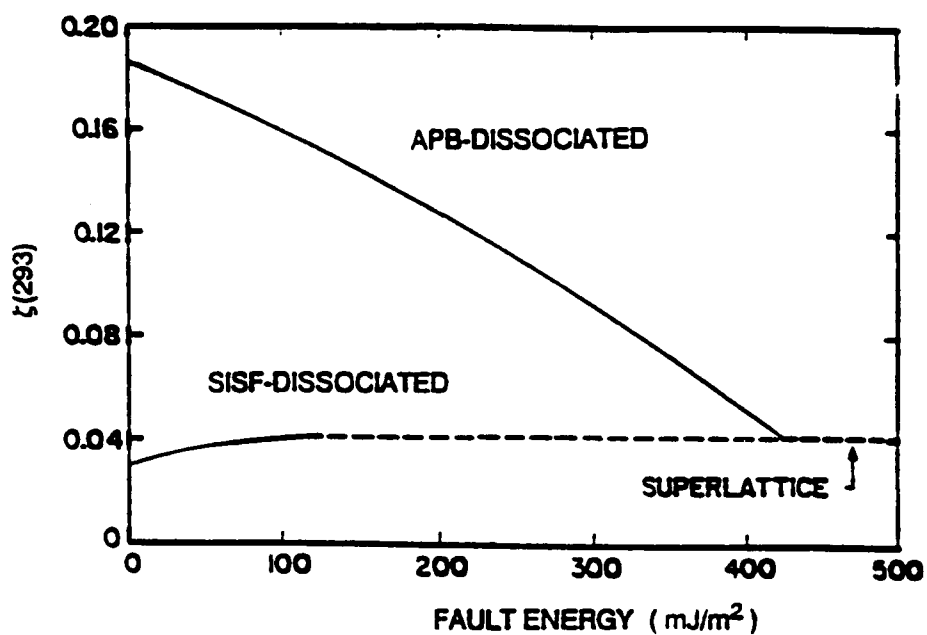
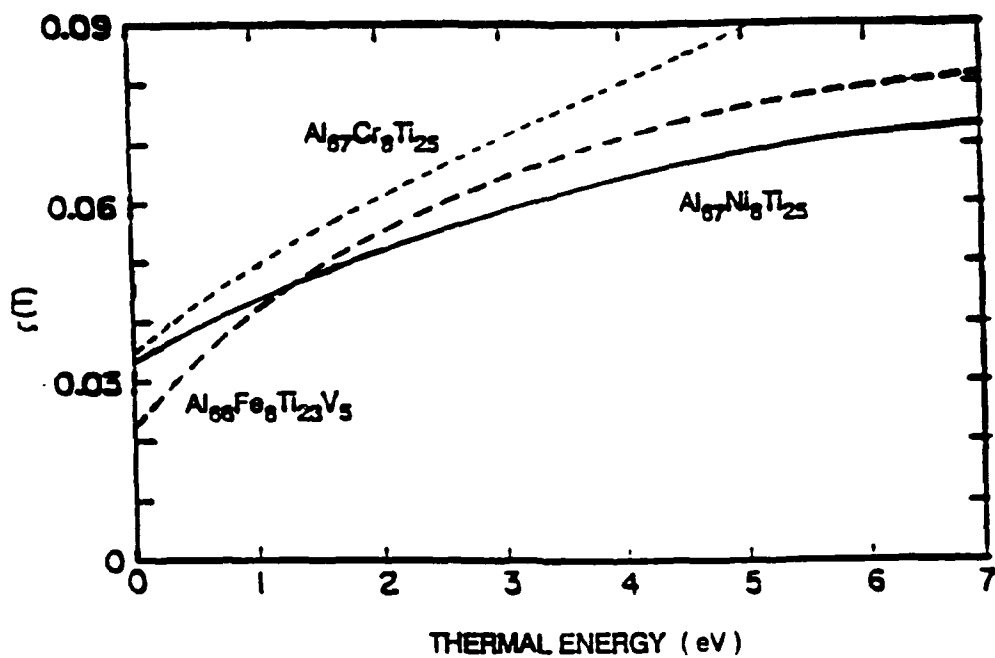
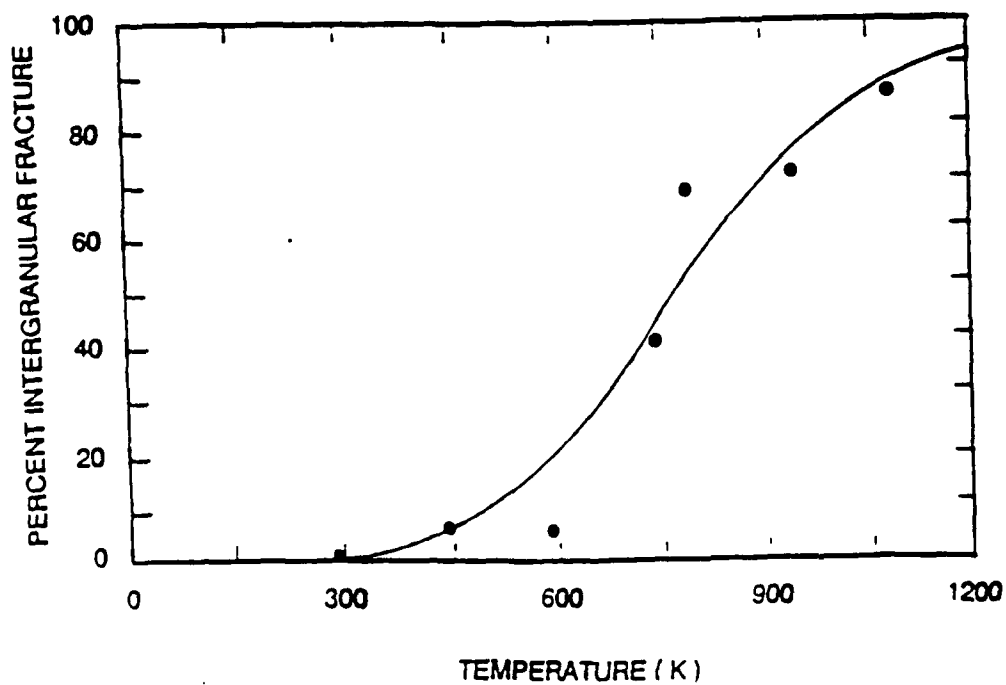


Fig. 2. Effect of $\{111\}$ APB and SISF energy on $\zeta(293)$ in $\text{Al}_{67}\text{Ni}_8\text{Ti}_{25}$. For values of SISF energy greater than about 150 mJ/m^2 , it is appropriate to use the value of $\zeta(293)$ associated with emission of an undissociated superlattice dislocation due to the narrow equilibrium separation between the two partial superlattice dislocations.



(a)



(b)

Fig. 3. (a) Effect of thermal energy on $\zeta(T)$ in several L1₂ intermetallic alloys. (b) Percent intergranular fracture as a function of temperature in $\text{Al}_{67}\text{Cr}_8\text{Ti}_{25}$

Submitted to *Metallurgical Transactions A*, 1993

**Experimental Assessment of Crack Tip Dislocation Emission Models
for an $\text{Al}_{67}\text{Cr}_8\text{Ti}_{25}$ Intermetallic Alloy**

W.G. Meng*, M.D. Vaudin⁺, M.F. Bartholomeusz* and J.A. Wert*

*Department of Materials Science and Engineering
University of Virginia
Charlottesville, VA 22903-2442

+Ceramics Division
National Institute for Standards and Technology
Gaithersburg, MD 20899

ABSTRACT

A potential explanation for cleavage fracture of intermetallic alloys with low or moderate CRSS is the existence of an energy barrier for crack tip dislocation emission, as described by models that analyze the energetics of dislocation emission from crack tips. In the present study, an intermetallic alloy with the L1_2 crystal structure, $\text{Al}_{67}\text{Cr}_8\text{Ti}_{25}$, has been used to experimentally assess the predictions of the Rice-Thomson dislocation emission model. The assessment is performed in two ways. First, model predictions of a fracture mode transition at elevated temperature are compared with experimental results. Bend tests performed at temperatures in the range 293 to 1061 K reveal that the fracture mode of $\text{Al}_{67}\text{Cr}_8\text{Ti}_{25}$ changes from predominately cleavage fracture at room temperature, to a mixed mode of cleavage and intergranular fracture at intermediate temperatures, and then to predominately intergranular fracture at high temperatures. The observed cleavage-to-intergranular fracture transition temperature is approximately 800 K, in good agreement with the model prediction. Second, model predictions of the effect of grain orientation on the fracture mode are compared with experimental results. Electron back scatter patterns and fractographic techniques were used to analyze the grain orientations and fracture modes of grains on the fracture surfaces of specimens fractured at 4 temperatures in the range 439 to 1061 K. Experimental results reveal a correlation between fracture mode and slip system orientation relative to the crack, in good agreement with dislocation emission model predictions.

1. Introduction

Rice and Thomson (RT) [1] sought to account for cleavage fracture in materials with low or moderate critical resolved shear stress (CRSS) by modeling the energetics of dislocation emission from atomically sharp cracks. The RT dislocation emission model shows that an energy barrier may exist for dislocation emission from a crack tip, depending on several material parameters, on the loading mode, and on the slip system geometry relative to the crack; but independent of CRSS. The dislocation emission model led to formulation of a fracture mode criterion for Mode I loading, as follows. When the remote stress satisfies the Griffith criterion for fracture, the model predicts whether dislocation emission from a crack tip is energetically favorable. If dislocation emission is not energetically favorable, sharp cracks are not blunted and the material is predicted to fail by cleavage fracture. If dislocation emission is energetically favorable, spontaneous emission of dislocations occurs prior to reaching the Griffith criterion and the crack is blunted. The blunted crack remains trapped at its original position until the external stress is increased sufficiently to promote crack tip damage processes that eventually lead to fracture by other mechanisms. RT model predictions of fracture mode correlate well with experimentally observed fracture modes for a variety of metals, ceramics and ionic compounds [1,2].

Turner, Powers and Wert (TPW) [3] first applied the RT model to intermetallic alloys. TPW showed that the RT model is consistent with cleavage fracture of $\text{Al}_{67}\text{Ni}_8\text{Ti}_{25}$, a trialuminide intermetallic alloy in which the Ni addition changes the crystal structure of Al_3Ti from D0_{22} to L1_2 . Room temperature plastic deformation of $\text{Al}_{67}\text{Ni}_8\text{Ti}_{25}$ in compression was shown to occur by glide of undissociated $\langle 110 \rangle \{111\}$ superlattice dislocations [3,4], which permitted direct application of the RT model. Other intermetallic alloys with the L1_2 crystal structure deform by glide of dissociated superlattice dislocations [5-9], complicating application of the original RT model which considers crack tip emission of single perfect dislocations. TPW applied the RT model to a variety of intermetallic alloys with the L1_2 crystal structure by considering two limiting cases. If the antiphase boundary (APB) or superlattice intrinsic stacking fault (SISF) between the two superlattice partial dislocations has high specific energy, the spacing of the two superlattice partial dislocations is small and their emission from a crack tip can be approximated as emission of an undissociated superlattice dislocation. Alternatively, if the APB or SISF energy is low, the two superlattice partial dislocations have sufficient equilibrium separation that their emission may be considered as two independent

events. Based on these limiting cases, TPW concluded that:

- i) crack tip dislocation emission of undissociated superlattice dislocations is generally unfavorable in $L1_2$ intermetallic alloys, and these materials are predicted to exhibit cleavage fracture; and
- ii) crack tip dislocation emission occurs readily in $L1_2$ intermetallic alloys with dissociated superlattice dislocations, and these materials are predicted to exhibit ductile fracture.

The conclusion reached by TPW through consideration of limiting cases was subsequently challenged when George and co-workers [10,11] showed that the $L1_2$ intermetallic alloys Al_3Sc and $Al_{66}Fe_6Ti_{23}V_5$ have dissociated dislocations and exhibit cleavage fracture. This led George *et al.* to propose low cleavage fracture strength as the cause of cleavage fracture in $L1_2$ trialuminide alloys. Their arguments were based on calculations showing that Al_3Sc has a significantly lower cohesive strength on $\{011\}$ than Ni_3Al , and that $\{011\}$ is the cleavage plane of Al_3Sc . However, as George *et al.* [11] pointed out, if low cohesive strength is the cause of brittle fracture, Al_3Sc should cleave on $\{111\}$, which is calculated to have lower cohesive strength than $\{011\}$. Moreover, the variety of cleavage fracture planes identified in $Al_{66}Fe_6Ti_{23}V_5$ [10], Al_3Sc [11] and $Al_{67}Ni_8Ti_{25}$ [3] is difficult to reconcile with a fracture mechanism based on low cleavage fracture strength.

More recently, Bartholomeusz and Wert (BW) [12–14] undertook a detailed analysis of the energetics of dissociated dislocation emission from crack tips. The fundamental dislocation energy concepts of the original RT model were preserved in the BW model, but additional energy terms were required to model crack tip emission of two superlattice partial dislocations coupled by an associated order or stacking fault. Excellent correlation was found between BW model results and published fracture mode observations for intermetallic alloys with the $L1_2$ and B2 crystal structures. In particular, the BW model predicts cleavage fracture at room temperature in some $L1_2$ intermetallic alloys with dissociated superlattice dislocations, such as Al_3Sc and $Al_{66}Fe_6Ti_{23}V_5$.

In addition to predicting the average fracture mode at room temperature, dislocation emission models can be used to make a variety of detailed predictions. These include predictions of fracture mode transition temperatures and predictions of the effect of grain orientation on fracture mode. Fracture mode transitions have been reported for several $L1_2$ trialuminide alloys [15–17], and excellent agreement is found

between BW model predictions and experimentally determined fracture mode transition temperatures in cases where sufficient data exist to apply the model [12,14]. However, the effect of grain orientation on fracture mode has not been reported for any $L1_2$ trialuminide alloy. Thus, while dislocation emission models are consistent with global fracture characteristics of $L1_2$ trialuminide alloys, the models make many specific predictions for which the corresponding experimental results have not been reported.

The goal of the present paper is to describe a detailed experimental assessment of dislocation emission model predictions for a trialuminide intermetallic alloy with the $L1_2$ crystal structure. $Al_{67}Cr_8Ti_{25}$ was selected as the model material for the present study. Assessment of dislocation emission model predictions includes two parts: an assessment of the predicted fracture mode transition temperature, and an assessment of the predicted effect of grain orientation on fracture mode at selected temperatures.

2. Experimental Procedure

High purity elemental metals consisting of aluminum pellets, chromium shot and titanium sponge were used as starting materials for preparation of a 10 g arc-melted sample of the $Al_{67}Cr_8Ti_{25}$ intermetallic alloy. To eliminate composition inhomogeneity resulting from solidification, the arc-melted Al-Cr-Ti alloy was homogenized at 1323 K for 100 hours in an evacuated silica tube. Homogenization of the Al-Cr-Ti alloy substantially increased the void volume fraction. Although previous investigators have demonstrated that voids introduced during homogenization do not alter the fracture mode of $Al_{67}Ni_8Ti_{25}$ [18], hot isostatic pressing (HIPing) was performed after homogenization to eliminate porosity. The alloy was HIPed at 1473 K and 200 MPa for 2 hours, after which metallographic examination confirmed that the voids had been eliminated. Most metallographic investigations of the microstructure were performed on specimens etched with Keller's reagent. Keller's reagent was modified to etch HIPed specimens for the purpose of delineating grain boundaries more clearly. The modified Keller's reagent contained 2 ml HF, 3 ml HCl, 20 ml HNO_3 and 175 ml H_2O .

Bend tests were conducted at room and elevated temperatures using single-edge-notched specimens cut from the HIPed alloy. All bend test specimens were rectangular bars with dimensions approximately $2 \times 3 \times 10 \text{ mm}^3$ which were cut by electrodischarge machining (EDM) and polished through 0.05 μm alumina prior to

testing. A rectangular notch of about 0.5 mm depth was cut by EDM in the center of one face of each specimen. A stainless steel fixture was used to hold the individual bend test specimens. The fixture was outfitted with an Inconel-sheathed thermocouple which served to hold the specimen in position for testing, to measure the specimen temperature, and to manipulate the test fixture. A tube furnace was first heated to a temperature 20 K higher than the selected test temperature and the fixture containing the specimen was inserted into the furnace. After the thermocouple reached the furnace temperature, the specimen was held in the furnace for an additional 30 seconds. Then the fixture was quickly withdrawn from the furnace, placed on an anvil, and the steel pin resting on the specimen was struck with a hammer. The test temperature was read from the thermocouple immediately upon breaking the specimen.

As described later, assessing the dislocation model predictions requires knowledge of the fracture mode, the crack plane orientation, the crack front orientation, and the slip system orientations within individual grains. Conventional fractography was used to determine the fracture mode and to check the assumption that the cleavage facets were approximately normal to the longitudinal axis of the bend test specimens. River markings on the cleavage fracture surfaces were used to determine the crack propagation direction, from which the crack front orientation could be estimated. Slip system orientations were determined from the crystal orientation information provided by electron back scatter patterns (EBSPs). The methods used for each of these analyses are summarized below

Fracture surfaces of the bend test specimens were examined using scanning electron microscopy (SEM). For each specimen, micrographs were taken at 100X magnification for every field of view on the fracture surface. A point counting method was used to measure the projected area fractions of cleavage and intergranular fracture on each fracture surface. To determine if stress state affected fracture mode, the fraction of intergranular fracture was measured for the entire fracture surface, and separately for the tension and compression halves of the fracture surface.

The bend test specimens were prepared for EBSP analysis using the following method. First, the fracture surfaces were protected by an acrylic spray coating. Each specimen was then mounted in a phenolic metallographic mount such that a transverse face of the bend specimen was exposed for grinding and polishing (see Fig. 1a for specimen orientation details). The exposed transverse face of the specimen was

subsequently ground to remove about 1/3 of the specimen thickness, and was then electropolished to remove the disturbed surface layer. Thus, the electropolished face represents a transverse section through the fracture surface near the midplane of the bend specimen. Finally, each specimen was carefully removed from the phenolic mount without damaging the fracture surface and the acrylic spray coating on the fracture surface was removed by acetone.

EBSP analyses were performed on an Amray 1830 SEM. The electropolished transverse section of each specimen was oriented such that the surface normal was inclined at 72° relative to the incident electron beam. When the electron beam was focused on one grain on the electropolished surface, an EBSP was obtained and the crystal orientation within the grain could be determined [19–23]. Crystal orientation information was stored in the form of an orientation matrix prescribing the orientation of the crystal axes relative to the specimen axes. To identify the crystal orientation of fractured grains, we obtained EBSPs from those grains which were exposed on both the electropolished surface and on the fracture surface; for example, grains labeled 4–7 in Figs. 1b and 2.

When the EBSP analyses were complete, conventional SEM micrographs of the fracture surface and electropolished plane near the fracture surface were used to identify the fracture modes of the specific grains whose crystal orientations had been determined. Finally, to confirm the correspondence between grains on the electropolished surface and on the fracture surface, the electropolished surface was severely etched to reveal the grain boundaries. By these methods, both the crystal orientations and fracture modes of approximately 10 grains per specimen were obtained for bend test specimens fractured at four different temperatures.

3. Experimental Observations

a. Microstructure

Fig. 3 shows the microstructure of the $\text{Al}_{67}\text{Cr}_8\text{Ti}_{25}$ alloy after the HIPing treatment. In accord with previous reports [24,25], HIPing eliminated the porosity present in the homogenized $\text{Al}_{67}\text{Cr}_8\text{Ti}_{25}$ alloy. A small volume fraction of second phase particles remains after the homogenization and HIPing treatments. Although no attempt was

made to identify these particles, they may be oxide or nitride particles formed as a result of contamination during preparation of the alloy. Inspection of micrographs from previous studies of trialuminide alloys indicates that such particles are generally present, but no previous investigators have suggested that these particles have a significant effect on macroscopic deformation and fracture properties.

The x-ray diffraction pattern obtained from a pulverized specimen of the homogenized $\text{Al}_{67}\text{Cr}_8\text{Ti}_{25}$ alloy was compared with the x-ray powder pattern calculated [26] for $\text{Al}_{67}\text{Cr}_8\text{Ti}_{25}$ with an L1_2 crystal structure assuming random substitution of Cr on the Al sites and a lattice parameter of 0.395 nm. A close correspondence between the measured and calculated patterns confirmed that the $\text{Al}_{67}\text{Cr}_8\text{Ti}_{25}$ alloy has an L1_2 crystal structure. Energy dispersive x-ray spectroscopy was used to evaluate the composition of the alloy after HIPing. The composition measured using this method was $\text{Al}_{68.1}\text{Cr}_{8.0}\text{Ti}_{23.9}$, similar to the nominal $\text{Al}_{67}\text{Cr}_8\text{Ti}_{25}$ composition.

b. Fractographic Analysis of Bend Test Specimens

Bend tests were performed at 7 temperatures in the range 298 to 1061 K. Examination of the fracture surfaces of bend test specimens showed that the fracture mode of $\text{Al}_{67}\text{Cr}_8\text{Ti}_{25}$ changes from predominantly cleavage fracture at ambient temperatures, to a mixture of cleavage and intergranular fracture at intermediate temperatures, and then to predominantly intergranular fracture at high temperatures. The fracture surfaces are not suggestive of increased plasticity prior to fracture at higher test temperatures.

Quantitative evaluation of the entire fracture surface of each bend test specimen yielded the projected area fraction of intergranular fracture as a function of test temperature, as shown by the filled circles in Fig. 4a. The ends of the vertical bars in Fig. 4a represent the projected area fractions of intergranular fracture on the tension and compression halves of the bend specimen fracture surfaces (the result for the tension half corresponds to the "T"-shaped end of each bar). The projected area fraction of intergranular fracture was generally greater on compression side of the bend test specimens than on the tension side, consistent with previous findings [16,17].

c. Crystal Orientation Measurements

Fig. 2 shows a portion of the bend specimen fractured at 919 K, both the fracture surface and the transverse section are visible. The fracture mode and crystal orientation were determined for the grains labeled 4 through 7 in Fig. 2. Close examination of Fig. 2 shows that the grains 4 and 7 fractured intergranularly and grains 5 and 6 fractured by cleavage. Crystal orientation measurements are represented in terms of rotation matrices that transform vector components from the L-T-S specimen axes to the cubic crystal axes. The rotation matrices for the 4 grains labeled in Fig. 2 are given in Table 1 along with the fracture modes for those grains. Similar measurements were performed for the bend test specimens fractured at 439, 733, 919 and 1061 K. Thus, both crystal orientation and fracture mode were determined in a total of 40 grains.

4. Dislocation Emission Modeling Results

a. Material Parameters Used for the Dislocation Emission Models

For ordered alloys with undissociated superlattice dislocations, four material parameters are needed to calculate the activation energy for crack tip dislocation emission: shear modulus (G), bulk modulus or Poisson's ratio (K or ν), superlattice dislocation Burgers vector (b_s), and fracture surface energy (γ). In the present implementation, we use the shear modulus on the slip plane (G_{slip}) and approximate the fracture surface energy by the free surface energy. For ordered alloys with dissociated superlattice dislocations, the fault energy (Γ) is also required as a model input. The dislocation core radius must be estimated for either dislocation configuration.

The model calculations described in the present paper consider crack tip emission of undissociated superlattice dislocations. Since only undissociated dislocations are involved, the RT model formulation has been used for these calculations. However, several aspects of the more recent BW model are used for comparison of modeling results and experimental observations. For simplicity, the blended models are referred to simply as *dislocation emission models* (DEMs) in the remainder of the present paper.

The values used for DEM calculations for $\text{Al}_{67}\text{Cr}_8\text{Ti}_{25}$ are listed in Table 2. These values were adopted from literature or were estimated, as described in the following paragraphs.

Shear modulus: Hecker *et al.* [2] recommend using the shear modulus on the slip plane, G_{slip} , rather than the polycrystalline average shear modulus, G_{poly} . A value of 75 GPa has been reported for G_{poly} by Mikkola *et al.* [27], and the Zener anisotropy coefficient was calculated to be 1.7 for Al_3Ti with the L1_2 crystal structure [28]. Inserting these values in equations developed by Turly and Sines [29] gives the value of G_{slip} shown in Table 2.

Poisson's ratio: Mikkola *et al.* [27] measured the value of Poisson's ratio for $\text{Al}_{67}\text{Cr}_8\text{Ti}_{25}$.

Burgers vector: The slip vector has not been reported for $\text{Al}_{67}\text{Cr}_8\text{Ti}_{25}$; however, the active slip system at room temperature is $\langle 110 \rangle \{111\}$ in all L1_2 trialuminides for which the slip vector has been determined [30]. Assuming that slip in $\text{Al}_{67}\text{Cr}_8\text{Ti}_{25}$ also occurs on $\langle 110 \rangle \{111\}$, the magnitude of \mathbf{b}_s can be determined from the lattice parameter, which was measured by x-ray diffraction in the present study.

Free surface energy: The free surface energy has been estimated using the relationship proposed by Reynolds [31] and values of $T_m = 1613$ K, interplanar spacing = 0.228 nm, and temperature dependence of the free surface energy = -0.5 mJ/m²K [3].

Dislocation core parameter: Since the self-energy of a semicircular dislocation loop emitted from a crack tip is a significant factor in DEMs, the value assigned to the core parameter α (ratio of the Burgers vector to the core radius) strongly influences modeling results. Hirth and Lothe [32] indicate that the range $1 \leq \alpha \leq 2$ is appropriate for metals; BW selected $\alpha = 1$ for a prior investigation of the effects of dislocation dissociation on crack tip dislocation emission in intermetallic alloys. In the present investigation of $\text{Al}_{67}\text{Cr}_8\text{Ti}_{25}$ where comparison of experimental and model results is performed at a level of detail considerably exceeding that attempted by BW, a value of $\alpha = 1.5$ was found to produce the best agreement with experimental observations. Since this value is within the range suggested by Hirth and Lothe as appropriate for metals, no fundamental significance is attached to selection of a different value than that used by BW.

A central result of the BW model is identification of a critical value of $\xi(T)$, the normalized solid angle range of slip system orientations corresponding to spontaneous or thermally activated dislocation emission at temperature T . By calculating $\xi(293)$ for various intermetallic alloys and comparing the $\xi(293)$ values with experimentally observed fracture modes, BW found that alloys having $\xi(293) < 0.08$ exhibit cleavage fracture at room temperature, while alloys having $\xi(293) > 0.08$ do not cleave. Thus, a critical value, $\xi_{crit} = 0.08$, was identified. Since the value of $\xi(293)$ calculated for each intermetallic alloy depends on the value assumed for α , identification of the critical value of ξ also depends on α . In the present work, where $\alpha = 1.5$ is found to improve detailed agreement with experimental results, a new value of ξ_{crit} has been determined by repeating the BW calculations with $\alpha = 1.5$ and correlating with model results with the same experimental observations summarized by BW. The new critical value, $\xi_{crit,1.5} = 0.15$, includes the value of α in the subscript in recognition of sensitivity of DEM results to the value assumed for α .

b. Prediction of the Effect of Temperature on Fracture Mode

RT proposed that thermal energy can assist crack tip dislocation emission when the activation energy for emission is small, an effect that could produce a fracture mode transition from cleavage to ductile fracture with increasing temperature. The effect of thermal energy on dislocation emission from a crack tip can be calculated using DEM methods. However, approximations are required to establish a correspondence between temperature and the thermal energy available to assist dislocation emission. BW estimated the amount of thermal energy available to assist dislocation emission as the total thermal energy of 4 core atoms per atom plane normal to the dislocation line, multiplied by the length of a semicircular dislocation loop of critical radius. In previous papers, BW presented DEM results based on the simplistic assumption that the critical half loop length is $10b_s$. In the present paper, detailed DEM calculations revealed that the critical half loop length varies with the activation energy required for dislocation emission: from $7b_s$ for an activation barrier of 1 eV, to $14b_s$ for an activation barrier of 8 eV. Thus, the thermal energy available to assist crack tip dislocation emission depends directly on temperature through the thermal energy per atom, and indirectly through the effect of temperature on the critical half loop length. These calculations were used to establish a correspondence between temperature and the thermal energy available to assist dislocation emission. This correspondence is represented by the temperature and energy scales along the lower and upper edges of Fig. 4b. Also shown

in Fig. 4b are the effect of thermal energy on $\xi(T)$ for $\text{Al}_{67}\text{Cr}_8\text{Ti}_{25}$ and the value of $\xi_{\text{crit},1.5}$. Following the BW interpretation, the results shown in Fig. 4b indicate that $\text{Al}_{67}\text{Cr}_8\text{Ti}_{25}$ is expected to exhibit a fracture mode transition near 800 K, where the value of $\xi(T)$ exceeds $\xi_{\text{crit},1.5}$.

c. Prediction of the Effect of Slip System Orientation on Fracture Mode

Fig. 5a shows the calculated activation energy for dislocation emission in $\text{Al}_{67}\text{Cr}_8\text{Ti}_{25}$ as a function of the slip system orientation parameters ϕ and ψ_s , which are defined for the ideal DEM geometry in Fig. 6a. The constant energy contours in Fig. 5a represent conditions of constant activation energy for the dislocation emission.

Spontaneous dislocation emission is not predicted for any slip system orientation at room temperature, consistent with $\xi(293) = 0$ in Fig. 4b.

Fig. 5b shows a projection of the 3 eV activation energy contour onto the ϕ - ψ_s plane. The loop-shaped contour line defines the locus of slip systems orientations for which the activation energy for crack tip dislocation emission has a constant value. Consider a case where the thermal energy available to assist dislocation emission is equal to the energy represented by the contour line in Fig. 5a. Comparing Figs. 5a and 5b reveals that slip system orientations inside the loop in Fig. 5b (labeled "E" = emission) require less thermal energy for dislocation emission than is available; emission occurs readily for these slip system orientations. Slip system orientations outside the loop in Fig. 5b (locations labeled "N" = no emission) represent orientations requiring more thermal energy for dislocation emission than is available; emission is inhibited for these slip system orientations. Note that the parameter $\xi(T)$ is the ratio of area E to area (N + E), with the requirement that the angles extend over their geometrically possible ranges of $-90^\circ \leq \psi_s \leq +90^\circ$ and $-180^\circ \leq \phi \leq +180^\circ$.

Through arguments presented in the Introduction, grains for which all slip system orientations lie in region N in Fig. 5b are predicted to exhibit cleavage fracture. In contrast, plastic crack blunting is expected to prevent cleavage for grains having at least 1 slip system in region E. At higher temperatures, the emission loop expands because more thermal energy is available to assist dislocation emission, causing cleavage fracture to become unfavorable in a larger fraction of grains. In this manner, DEMs can be used to make specific predictions about the correspondence between grain orientation and fracture mode as a function of temperature; the DEM predictions for

$\text{Al}_{67}\text{Cr}_8\text{Ti}_{25}$ are presented in Section 5b in conjunction with the experimental observations.

5. Discussion

a. *Assessment of Model Predictions of the Fracture Mode Transition Temperature*

Fig. 4 illustrates the effect of temperature on both the experimentally observed fracture mode and $\xi(T)$ calculated using DEM. Based on the value of $\xi_{\text{crit},1.5}$, DEMs predict a fracture mode transition for $\text{Al}_{67}\text{Cr}_8\text{Ti}_{25}$ at approximately 800 K. The experimental results also exhibit a gradual fracture mode transition over a temperature range roughly centered at 800 K. Thus, the fracture mode transition predicted by DEM is consistent with the experimental observations of the average fracture mode.

Two other aspects of the DEM results may be compared with the experimental observations of average fracture mode. First, Fig. 4b reveals that $\xi(T)$ increases gradually with temperature above 600 K, indicating that the fraction of grains favorably oriented for dislocation emission increases gradually with temperature. This suggests that the fracture mode transition should occur over a range of temperatures rather than abruptly at one temperature. As noted earlier, the experimental results exhibit the expected gradual fracture mode transition.

A second aspect of the comparison between the DEM results and the average fracture mode observations concerns the temperature at which dislocation emission is predicted in any grain. Fig. 4b shows that dislocation emission is not predicted for any grain orientations for temperatures below 600 K (represented by $\xi(T) = 0$ for $T < 600$ K). Thus, DEM calculations predict that the fraction of cleavage fracture should be 1 for $T < 600$ K, and should rise gradually for temperatures above 600 K. The experimental results represented in Fig. 4a shows that the fraction of intergranular fracture is very small below 600 K, and begins to increase at about 600 K; in accord with DEM predictions.

The comparisons noted above show that the DEM predictions for the occurrence of cleavage fracture are in excellent agreement with experimental observations for $\text{Al}_{67}\text{Cr}_8\text{Ti}_{25}$. However, DEM fracture mode transition predictions generally consider a

transition from cleavage fracture to ductile fracture, not to intergranular fracture as found for $\text{Al}_{67}\text{Cr}_8\text{Ti}_{25}$. Kumar and Brown [15,16] reported a similar cleavage-to-intergranular fracture mode transition in $\text{Al}_{66}\text{Mn}_9\text{Ti}_{25}$ and $\text{Al}_{67}\text{Cr}_8\text{Ti}_{25}$, suggesting that the observations made in the present investigation do not represent an isolated case. Recall that DEM results do not directly predict fracture mode, they only predict whether or not dislocation emission from an atomically sharp crack is favorable at the minimum stress required for cleavage fracture for mode I loading in plane strain. If model calculations show that dislocation emission is favorable, the model predicts that cleavage fracture will not occur, but does not identify an alternate fracture mode. Thus, we adopt the point of view that intergranular fracture is the alternate fracture mode exhibited by $\text{Al}_{67}\text{Cr}_8\text{Ti}_{25}$ when cleavage is suppressed, and that DEM predictions of fracture mode transition temperatures apply to the cleavage-to-intergranular transition. This point is considered further in Section 5d where additional experimental evidence is presented in support of the point of view that DEM predictions apply to the cleavage-to-intergranular fracture mode transition in $\text{Al}_{67}\text{Cr}_8\text{Ti}_{25}$.

b. Assessment of Model Predictions of the Effect of Grain Orientation on Fracture Mode

In Section 5a the average fracture mode predictions were compared with the average fracture mode observations. The current section compares DEM fracture mode predictions and experimental observations for individual grains. To make these comparisons, several assumptions about the crack and slip system geometry are required. These assumptions discussed first, then comparisons between DEM predictions and observations are made.

i) Calculation of the angles ϕ and ψ_s in each grain

We first assume that the cleavage fracture planes are normal to the long axes of the bend specimens. This assumption is supported by SEM and metallographic observations showing that the cleavage fracture facets in the $\text{Al}_{67}\text{Cr}_8\text{Ti}_{25}$ alloy are flat and are nearly perpendicular to the sides of the specimens fractured at 733, 919 and 1061 K. SEM observations suggest that the orientation of the cleavage fracture facets do not deviate by more than 12° from the assumed orientation for the 3 specimens listed above. However, SEM observations for the specimen fractured at 439 K reveal that the cleavage fracture facets deviate considerably from the assumed orientation for grains 1 through 8. An accurate assessment of the cleavage facet orientations for the specimen

fractured at 439 K is not possible because the grains of interest were ground away during metallographic preparation after the EBSD experiments were complete. Fortunately, DEM results described later show that cleavage is predicted in $\text{Al}_{67}\text{Cr}_8\text{Ti}_{25}$ for all slip system orientations at 439 K. This permits DEM predictions of cleavage fracture at 439 K to be compared to experimental results, irrespective of the ϕ values assigned to individual grains. We therefore retain the assumption that the crack planes are normal to the long axes of the bend test specimens in all cases, and note in subsequent comparisons between DEM results and experimental observations that the ϕ values for grains 1 through 8 of the specimen fractured at 439 K are inaccurate. Combining the assumed cleavage facet orientations with the grain orientation results, we can determine the orientation of crack plane relative to the slip planes in each grain. This permits determination of ϕ , the angle between the slip plane and the crack plane, for every $\langle 110 \rangle \{111\}$ slip system in each grain.

The standard DEM geometry is illustrated in Fig. 6a which shows that the crack front is contained in the slip plane and permits a simple definition of the angle ψ_s as the complement of the angle between the crack front and the Burgers vector. This ideal geometry is not necessarily attained in fracture experiments with a polycrystalline specimen. Instead, the more complex situation illustrated in Fig. 6b generally occurs. However, simply redefining ψ_s as the complement of the angle between the Burgers vector and the crack plane/slip plane intersection allows calculation of ψ_s for each $\langle 110 \rangle \{111\}$ slip system.

ii) Selection of slip systems by ψ_s

For $\langle 110 \rangle \{111\}$ slip, three values of ψ_s are associated with each slip plane, corresponding to the three Burgers vector orientations on each slip plane. Examination of the geometry of crack tip dislocation emission leads to the conclusion that emission is favored for Burgers vector orientations associated with small values of ψ_s , regardless of the details of the DEM. Thus, only the Burgers vector orientation with the lowest value of ψ_s for each slip plane is considered in subsequent analyses. This limits consideration to 4 slip systems in each grain, rather than 12.

iii) Selection of favorable slip system(s) for crack tip dislocation emission

DEM analyses assume that the crack front contains the slip plane, as schematically illustrated in Fig 6a. As noted previously, this ideal situation is unlikely to be achieved in most grains. We next consider the extent to which the crack/slip system geometry in individual grains deviated from the ideal slip system geometry. In the present paper, this assessment is based on the range of crack front orientations on the fracture surface. Ultimately, we seek to determine the angle κ , defined in Fig. 6b as the angle between the crack front and the crack plane/slip plane intersection. Small values of κ indicate nearly ideal DEM geometry.

After the bend test specimens are fractured it is not possible to measure directly the crack front orientation at each point in the crack propagation process. Fortunately, river markings on cleavage facets are indicative of the local crack propagation direction [75]; we assume that the crack front is normal to the direction of propagation. For example, Fig. 7a shows the river markings on individual cleavage facets on the fracture surface of the bend specimen fractured at 439 K. Although the river marking direction is somewhat variable, averaging the river marking directions on all cleavage facets indicates that the crack propagation direction was approximately normal to the notch root. River markings deviate locally from the assumed propagation direction, but nearly all are within $\pm 25^\circ$ of the assumed propagation direction.

A similar conclusion was reached after detailed analyses of the bend specimens fractured at 919 K and 1061 K, although the analysis is compromised to some extent for the specimens fractured at higher temperatures as a result of the reduced fraction of grains that exhibit cleavage fracture. However, for the specimen fractured at 733 K, the river markings suggest that the crack propagated parallel to the notch root, as shown in Fig. 7b. We are not certain why this occurred, possibly the specimen or loading pin became misaligned in the bend test fixture before the test was performed. For this specimen, the river markings were taken as a more conclusive indication of the crack propagation direction than the initial specimen geometry.

The above considerations show how the crack front orientation relative to the specimen axes can be approximately established. Combining this information with the grain orientation information permits calculation of the angle κ for each of the 4 slip planes in every grain. Performing this evaluation shows that none of the slip planes

examined identically satisfies the model geometry for the average crack front orientation. In the prior discussion of river markings on the fracture surfaces, it was noted that local crack propagation directions, as inferred from river marking orientations, are nearly always within $\pm 25^\circ$ of the average crack propagation direction. Since the crack front orientation may deviate by up to 25° from the average propagation direction, slip systems with $|\kappa| \leq 25^\circ$ *may* satisfy the ideal DEM geometry. Thus, we include in subsequent analyses slip systems having $|\kappa| \leq 25^\circ$.

To compare experimental observations with DEM predictions for individual grains, we therefore use the following strategy. For slip systems with $|\kappa| \leq 25^\circ$, we consider that the assumptions of the DEM are approximately satisfied and a direct comparison of model results with experimental observations is performed. If model calculations show that spontaneous or thermally activated emission is favorable for at least one slip system with $|\kappa| \leq 25^\circ$, we consider that a fracture mode other than cleavage is predicted. For slip systems with $|\kappa| > 25^\circ$, we assume that the slip system deviates significantly from the ideal DEM geometry and that the model results do not apply. For these slip systems, the shear stress on the slip planes is small and dislocation emission is unlikely to be energetically favorable. Thus, grains for which $|\kappa| > 25^\circ$ for all slip systems are included in the comparison by making the simplistic assumption that cleavage fracture is favored for all such grains.

iv) Comparison of experimental results and emission model predictions

Applying the selection criteria described previously identifies 0, 1, or 2 slip systems with $|\kappa| \leq 25^\circ$ in each grain. The values of ϕ and ψ_s locate these slip systems on a ϕ - ψ_s plot; such plots are shown in Fig. 8 for individual test temperatures. The small number adjacent to each open or closed circle represents the grain number associated with the particular slip system orientation. (Recall that the values of ϕ for grains 1 through 8 of the specimen fractured at 439 K are inaccurate.) In some grains, two slip systems with $|\kappa| \leq 25^\circ$ were identified. Since we have assumed that emission on a single slip system is sufficient to prevent cleavage fracture, only the most favorable of the two slip systems in these grains is included in Fig. 8. The experimentally determined fracture mode is also indicated on Fig. 8 by the symbols used to represent the slip system orientations. Open circles represent grains exhibiting cleavage fracture and filled circles represent grains exhibiting intergranular fracture.

In addition to presenting experimental slip system orientation and fracture mode results, Fig. 8 compares the experimental results with the dislocation emission model results. The semicircular region on each graph represents the range of slip system orientations over which DEMs predict spontaneous or thermally activated emission at the test temperature. Good agreement between the emission model and experimental results is characterized by filled symbols lying within the semicircular region and open symbols lying outside the semicircle. A filled symbol lying outside the semicircle represents a grain that did not cleave, although the DEM predicted that cleavage was favorable. An open symbol lying inside the semicircle represents a grain that cleaved when the DEM predicted crack tip dislocation emission.

Lastly, experimental observations for grains containing only slip systems with $|\kappa| > 25^\circ$ are indicated in the upper right corner of each ϕ - ψ_s plot in Fig. 8. Recall that we make the simplistic assumption that all such grains are predicted to cleave.

The fraction of grains for which agreement is obtained between the experimental observations and model predictions could be used as a measure of DEM accuracy. For the present results, DEMs correctly predict the fracture mode in over 83% of all the grains examined. Given the many uncertainties and assumptions required for detailed comparison of the experimental and DEM results, we interpret the high level of agreement as strong evidence supporting the fundamental concepts embodied in the DEM.

c. Validity of Model Assumptions

In this section, several assumptions involved in the preceding analysis are examined to evaluate their impact on the agreement between DEM and the experimental observations. Principal among these are the value assumed for the core radius parameter (α), the range of slip system orientations accepted (κ range), and the assumption that dislocations are undissociated.

It is well-known that DEM results are sensitive to the value assumed for α . This sensitivity arises because the self energy of the semicircular dislocation loop is a large term in the energetic analysis. Decreasing α increases the core radius, which reduces the dislocation self energy and reduces the energy barrier for dislocation emission. Thus, decreasing α has the effect of shifting the energy surface shown in Fig. 5a to

lower values of energy and expanding the loop corresponding to spontaneous or thermally activated emission (region E) on the projected ϕ - ψ_s plot in Fig. 5b. In the present study, model calculations were performed using values of α in the range 1 to 2. Reasonable agreement is obtained between model and experimental results over a very narrow range of α values, from about 1.4 to 1.6.

Although α is an adjustable model parameter within the range 1 to 2, variation of α can only shrink and expand the loop-shaped region corresponding to spontaneous or thermally activated emission on the ϕ - ψ_s plots. Selecting different values for α cannot change the shape of the favorable emission region on the ϕ - ψ_s plots; these loop-shaped regions are always centered around $\phi = 60^\circ$ and $\psi_s = 0$. Thus, varying α can only affect agreement between the model and experimental results in a limited way.

A second assumption addresses the allowed κ range. Geometrical considerations show that dislocations emitted on slip systems having κ near $\pi/2$ do not blunt the crack. Thus, irrespective of the details of the DEM, cleavage fracture is predicted for slip systems having κ near $\pi/2$. However, this general consideration does not indicate the range of κ values for which the idealized model geometry is a reasonable approximation. We selected the range $|\kappa| \leq 25^\circ$ based on two considerations. First, river markings on the cleavage fracture facets deviated by up to about 25° from the crack propagation direction determined from specimen geometry. Factors such as local grain orientation, local stress field, and local crack geometry are probably responsible for this deviation. Since the crack front orientation deviated by up to 25° from the ideal crack front orientation, rejecting grains with $|\kappa| < 25^\circ$ would omit grains from the fracture mode comparison that have the possibility of locally satisfying the ideal model geometry.

Second, we explored the possibility of expanding the $|\kappa|$ range beyond 25° and found that values larger than 30° encompassed several slip systems in a majority of grains. This increased the opportunity for emission to the extent that cleavage become unfavorable in many grains, even at low temperatures where cleavage fracture is observed in the majority of grains. Thus, there is limited direct support for selecting the range $|\kappa| < 25^\circ$, and this range also provides the best agreement between DEM predictions and experimental fracture mode observations.

Both dissociated and undissociated superlattice dislocations have been reported in trialuminide alloys with the $L1_2$ crystal structure [33]. In the present paper, the DEM

results presented so far assume that undissociated superlattice dislocations are emitted. We now show that the model predictions based on emission of dissociated superlattice dislocations can provide equally good agreement with the experimental results. First, BW showed that SISF dissociation of superlattice dislocations does not have a strong effect on crack tip dislocation emission. Thus, SISF dissociation would not appreciably alter the DEM fracture mode predictions presented above.

Mikkola *et al.* [33] recently presented experimental observations of APB dissociated superlattice dislocations in an $\text{Al}_{67}\text{Mn}_8\text{Ti}_{25}$ alloy, and proposed that only APB dissociation occurs in L1_2 trialuminide alloys. BW model results showed that the energy barrier to emission of APB dissociated superlattice dislocations decreases with decreasing APB energy. Additional calculations for the specific case of $\text{Al}_{67}\text{Cr}_8\text{Ti}_{25}$ show that lowering the APB energy expands the emission loops in Fig. 5. It would appear that significant expansion of the emission loops would degrade agreement between DEM predictions and experimental results. However, for any APB energy, a core radius parameter can be chosen such that the emission loops are essentially unchanged from those shown in Fig. 5. Thus, the assumption that undissociated superlattice dislocations are emitted from crack tips does not preclude good agreement between DEM predictions and experimental results for the case of APB dissociated dislocations, provided that α is considered to be an adjustable DEM parameter.

d. Alternate Interpretations of the Experimental Results

As a final discussion point, it is valuable to consider whether alternate fracture mechanisms could account equally well for the experimental observations. In particular, we consider two potential mechanisms: a decrease in CRSS at elevated temperatures and grain boundary embrittlement at elevated temperatures.

Two experimental observations demonstrate that the fracture mode transition in $\text{Al}_{67}\text{Cr}_8\text{Ti}_{25}$ is not a result of decreasing CRSS with increasing temperature. First, Fig. 9 shows elevated temperature microhardness measurements for $\text{Al}_{67}\text{Cr}_8\text{Ti}_{25}$. A slight increase in hardness near 650 K reflects a range of positive temperature dependence of CRSS, a frequent observation in intermetallic alloys with the L1_2 crystal structure [9]. The slight increase in microhardness at intermediate temperatures found in the present study is qualitatively consistent with various prior yield strength results for $\text{Al}_{67}\text{Cr}_8\text{Ti}_{25}$ which reveal either an increase in yield strength or a yield strength plateau at

intermediate temperatures [17,33–35]. Of more significance for the present argument, both the yield strength and microhardness results indicate that the CRSS does not decrease rapidly in the temperature range between 700 and 800 K where the projected area fraction of intergranular fracture increases from approximately 0.2 to 0.7. This provides strong evidence that the fracture mode transition is not caused by decreasing CRSS. Second, compression test results from prior studies [16,23] show that the room temperature yield strength is less than 500 MPa, corresponding to $\text{CRSS}/G \approx 10^{-3}$. Engineering alloys with similar values of CRSS/G do not generally exhibit cleavage fracture, suggesting that the room temperature yield strength of $\text{Al}_{67}\text{Cr}_8\text{Ti}_{25}$ is insufficient to prevent plastic crack blunting.

Observation of a temperature range where the microhardness increases with temperature suggests that thermally activated cross slip may cause a change of active slip system in $\text{Al}_{67}\text{Cr}_8\text{Ti}_{25}$ at approximately 600 K. Such a change would require revision of the calculations for ϕ , ψ_s , and κ , and re-examination of the comparison between DEM results and experimental observations. However, as noted by previous authors [17], a propensity for thermally activated cross slip does not necessarily imply a change of active slip plane. For example, Kumar *et al.* [15] found predominately $\langle 110 \rangle\{111\}$ dislocations in $\text{Al}_{66}\text{Mn}_9\text{Ti}_{25}$ after plastic deformation at 923 K; well above the temperature where Zhang *et al.* [33] observed a peak in yield strength. In the results from the present study, it is notable that the temperature range of most rapid change in fracture mode is more than 100 K higher than the microhardness peak, and that the fracture mode transition continues at temperatures exceeding 1100 K. Until additional information regarding the active slip systems in $\text{Al}_{67}\text{Cr}_8\text{Ti}_{25}$ becomes available, we retain the interpretation of experimental results presented in the Section 5b.

The present interpretation of DEM predictions is based on the idea that a fracture mode transition occurs because the material becomes resistant to cleavage fracture as temperature increases. Alternately, a fracture mode transition could result from a mechanism that promotes intergranular fracture as temperature increases. In particular, intergranular fracture due to impurity segregation could become more severe at elevated temperatures, if segregation kinetics were the controlling factor. However, recall that the $\text{Al}_{67}\text{Cr}_8\text{Ti}_{25}$ alloy was cooled from the HIPing treatment at a much slower rate than the heating rate used for the bend tests. If the kinetics of impurity segregation to grain boundaries were the critical step, segregation would have occurred during cooling and intergranular fracture would have been observed at room temperature. Since cleavage

fracture exclusively was observed at room temperature, such a mechanism does not account for the fracture mode transition observed in $\text{Al}_{67}\text{Cr}_8\text{Ti}_{25}$ alloy.

6. Conclusions

1. The fracture mode of a $\text{Al}_{67}\text{Cr}_8\text{Ti}_{25}$ changes from predominantly cleavage at ambient temperatures, to a mixture of cleavage and intergranular fracture at intermediate temperatures, and then to predominantly intergranular fracture at high temperatures. The cleavage-to-intergranular fracture transition temperature is about 800 K.

2. The cleavage-to-intergranular fracture mode transition of the $\text{Al}_{67}\text{Cr}_8\text{Ti}_{25}$ alloy is consistent with thermally activated crack tip dislocation emission predictions. The DEM prediction of the fracture mode transition temperature matches well with experimental results.

3. The grain orientation range corresponding to cleavage and intergranular fracture modes as predicted by DEM matches well with experimental results. Many approximations are involved in analysis of the experimental results, but in each case the approximations have been shown to be reasonable or the correlation has been shown to be insensitive to the approximation. The correlation between model predictions and experimental observations provide support for the principles upon which the dislocation emission models are based.

7. Acknowledgments

The authors have appreciated helpful discussions with Dr. D. Slavic and Prof. D. Mikkola. Experimental assistance of Mr. H. Koenigsmann, Prof. K. Lawless, Ms. S. Zambo, and Ms. Di Lan is gratefully acknowledged. This work has been sponsored by the Air Force Office of Scientific Research under Contract Number AFOSR-90-0143; Dr. A. Rosenstein was the contract monitor.

8. References

1. J.R. Rice and R. Thomson, *Phil. Mag.*, 1974, vol. 29, pp. 73-97.
2. S.S. Hecker, D.L. Rohr and D.F. Stein, *Met. Trans. A*, 1978, vol. 9A, pp. 481-488.
3. C.D. Turner, W.O. Powers and J.A. Wert, *Acta Metall.*, 1989, vol. 37, pp. 2635-2643.
4. V.K. Vasudevan, R. Wheeler and H. L. Fraser, in *High Temperature Ordered Intermetallic Alloys III*, C.T. Liu, A.I. Taub, N.S. Stoloff and C.C. Koch (eds.), MRS, Pittsburgh, 1989, pp. 705-710.
5. M.J. Marcinkowski, in *Electron Microscopy and Stength of Crystals*, G. Thomas and J. Washburn (eds), Wiley Interscience, New York, 1963, pp. 333-440.
6. N.S. Stoloff and R.G. Davies, *Progress in Materials Science*, 1966, vol. 13, pp. 1-84.
7. M.J. Marcinkowski, *Treatise on Materials Science and Technology*, 1974, vol. 5, pp. 181-287.
8. M. Yamaguchi, V. Vitek and D.P. Pope, *Phil. Mag.*, 1981, vol. 43, pp. 1027-1044.
9. D.P. Pope and S.S. Ezz, *Inter. Metals Reviews*, 1984, vol. 29, pp. 136-167.
10. E.P. George, J.A. Horton, W.D. Porter and J.M. Schneibel, *J. Mater. Res.*, 1990, vol. 4, pp. 78-84.
11. E.P. George, W.D. Porter, H.M. Henson, W.C. Oliver and B.F. Oliver, *J. Mater. Res.*, 1991, vol. 5, pp. 1639-1648.
12. M.F. Bartholomeusz and J.A. Wert, *Acta Metall. Mater.*, 1992, vol. 40, pp. 673-682.
13. M.F. Bartholomeusz and J.A. Wert, *J. Mater. Res.*, 1992, vol. 7, pp. 919-925.
14. M.F. Bartholomeusz, W.G. Meng and J.A. Wert, in *High-Temperature Ordered Intermetallic Alloys V*, I. Baker, R. Darolia, J.D. Whittenberger and M.H. Yoo (eds), MRS, Pittsburgh, 1992, pp. 537-542.
15. K.S. Kumar and S.A. Brown, *Phil. Mag.*, 1992, vol. 65, pp. 91-109.
16. K.S. Kumar and S.A. Brown, *Acta Metall. Mater.*, 1992, vol. 40, pp. 1923-1932.
17. K.S. Kumar, S.A. Brown and J.D. Whittenberger, in *High Temperature Ordered Intermetallic Alloys IV*, L.A. Johnson, D.P. Pope and J.O. Stiegler (eds), MRS, Pittsburgh, 1990, pp. 481-486.
18. D.D. Mysko, J.B. Lumsden, W.O. Powers and J.A. Wert, *Scripta Metall.*, 1989, vol. 23, pp. 1827-1830.
19. J.A. Venables and R. Bin-Jaya, *Phil. Mag.*, 1977, vol. 34, pp. 1317-1321.
20. D.J. Dingley, *Scanning Electron Microscopy*, 1984, vol. ii, pp. 569-575.
21. D.J. Dingley and K. Baba-Kishi, *Scanning Electron Microscopy*, 1986, vol. ii, pp. 383-391.
22. S.I. Wright and B.L. Adams, *Metall. Trans. A*, 1992, vol. 23A, pp. 759-767.
23. S. Zhang, J.P. Nic and D.E. Mikkola, *Scripta Metall. Mater.*, 1990, vol. 24, pp. 57-62.
24. D.C. Slavik, J.A. Wert and R.P. Gangloff, "Determining Facet Crystallography Using Electron Back Scatter Patterns and Quantitative Tilt Fractography", submitted to *J. Materials Research*, 1993.
25. J.P. Nic, S. Zhang, and D.E. Mikkola, *Scripta Metall. Mater.*, 1990, vol. 24, pp. 1099-1104.

26. B.D. Cullity, *Elements of X-Ray Diffraction*, Second edition, Addison-Wesley, 1978, pp. 104-136.
27. D.E. Mikkola, J.P. Nic, S. Zhang and W.W. Milligan, *ISIJ International*, 1991, vol. 31, pp. 1076-1079.
28. M.H. Yoo, *Acta Metall.*, 1987, vol. 35, pp. 1559-1569.
29. J. Turley and G. Sines, *J. Phys. D: Applied Physics*, 1971, vol. 4, pp. 264-271.
30. S. Zhang, D.E. Mikkola and W.W. Milligan, *Scripta Metall. Mater.*, 1992, vol. 27, pp. 1073-1077.
31. C.L. Reynolds, P.R. Couchman and F.E. Karasz, *Phil. Mag.*, 1976, vol. 34, pp. 659-661.
32. J.P. Hirth and J. Lothe, *Theory of Dislocations*, McGraw-Hill, 1968, pp. 211-212.
33. S. Zhang, D.E. Mikkola and W.W. Milligan, *Scripta Metall. Mater.*, 1992, vol. 27, pp. 1073-1077.
34. S. Zhang, J.P. Nic, W.W. Milligan and D.E. Mikkola, *Scripta Metall. Mater.*, 1990, vol. 24, pp. 1441-1446.
35. H. Mabuchi, K. Hirukawa, H. Tsuda and Y. Nakayama, *Scripta Metall. Mater.*, 1990, vol. 24, pp. 505-508.

Table 1

Grain Orientation Matrices and Fracture Mode for Selected Grains
from the Bend Test Specimen Fractured at 919 K.

Grain Number	Fracture Mode	Rotation Matrix		
4	Intergranular	-0.306	-0.845	-0.438
		0.929	-0.365	0.057
		-0.208	-0.389	0.897
5	Cleavage	-0.778	0.544	-0.315
		-0.014	-0.515	-0.857
		-0.628	-0.662	0.408
6	Cleavage	-0.422	-0.723	-0.547
		0.805	-0.576	0.140
		-0.417	-0.382	0.825
7	Intergranular	0.314	0.426	0.848
		-0.928	-0.050	0.369
		0.199	-0.903	0.380

Table 2

Material Parameters Used for Dislocation Emission Calculations for $\text{Al}_{67}\text{Cr}_8\text{Ti}_{25}$.

Property	Value
G_{slip} (GPa)	61
ν	0.13
γ (J/m ²)	2.4
b_s (nm)	0.558

List of Figures

Fig. 1 Schematic diagrams showing specimen geometry used for local grain orientation and fracture mode determination. a) Specimen geometry showing orientation of transverse section. b) Specimen orientation during EBSD measurements.

Fig. 2 A portion of the bend test specimen fractured at 919 K showing locations of EBSD measurements and fracture mode in grains labeled 4–7.

Fig. 3 Microstructure of the $\text{Al}_{67}\text{Cr}_8\text{Ti}_{25}$ alloy after the HIPing treatment.

Fig. 4 a) Filled circles represent the projected area fraction of intergranular fracture as a function of test temperature. The ends of the vertical bars represent the projected area fractions of intergranular fracture on the tension halves ("T"-shaped end) and compression halves (plain end) of the bend specimen fracture surfaces. b) The effect of thermal energy on the fractional angular range corresponding to spontaneous or thermally activated dislocation emission, $\xi(T)$, for $\text{Al}_{67}\text{Cr}_8\text{Ti}_{25}$.

Fig. 5 a) The activation energy surface for dislocation emission as a function of the slip system orientation parameters ϕ and ψ_s for $\text{Al}_{67}\text{Cr}_8\text{Ti}_{25}$. b) A projection of the 3 eV activation energy contour onto the ϕ - ψ_s plane.

Fig. 6 a) Schematic diagram showing ideal crack/slip system geometry for dislocation emission models. b) Definition of the angle κ representing deviation from the ideal case.

Fig. 7 a) River markings on individual cleavage facets on the fracture surface of the bend specimen fractured at 439 K. b) River markings on individual cleavage facets on the fracture surface of the bend specimen fractured at 733 K. The notch is at the top of both fractographs.

Fig. 8 The ϕ - ψ_s plane for 4 test temperatures showing DEM results and experimental fracture mode observations for individual grains. Open circles represent grains that cleaved and filled circles represent grains that failed by intergranular fracture; small numbers indicate the grain number. Regions labeled "E" represent ϕ - ψ_s combinations where spontaneous or thermally activated dislocation emission is favorable; emission is unfavorable in regions labeled "N".

Fig. 9 Elevated temperature microhardness measurements for $\text{Al}_{67}\text{Cr}_8\text{Ti}_{25}$.

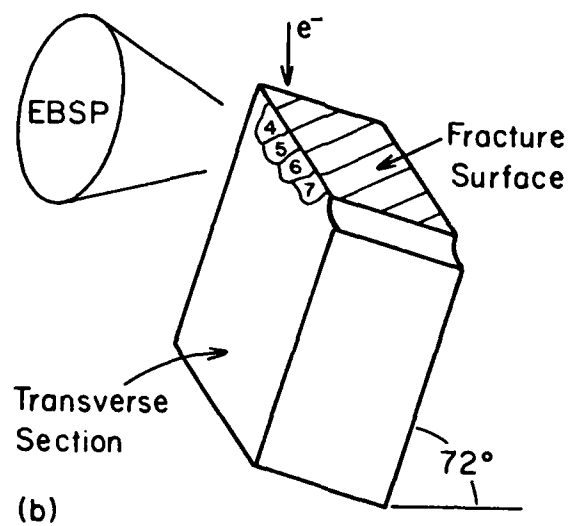
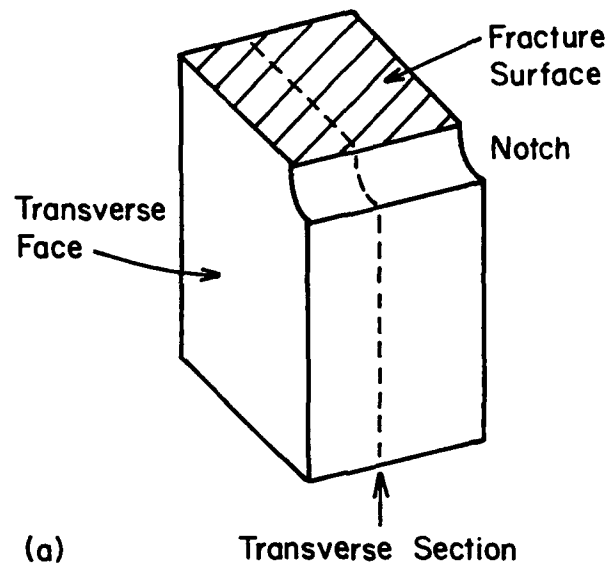


Fig. 1 Schematic diagrams showing specimen geometry used for local grain orientation and fracture mode determination. a) Specimen geometry showing orientation of transverse section. b) Specimen orientation during EBSD measurements.

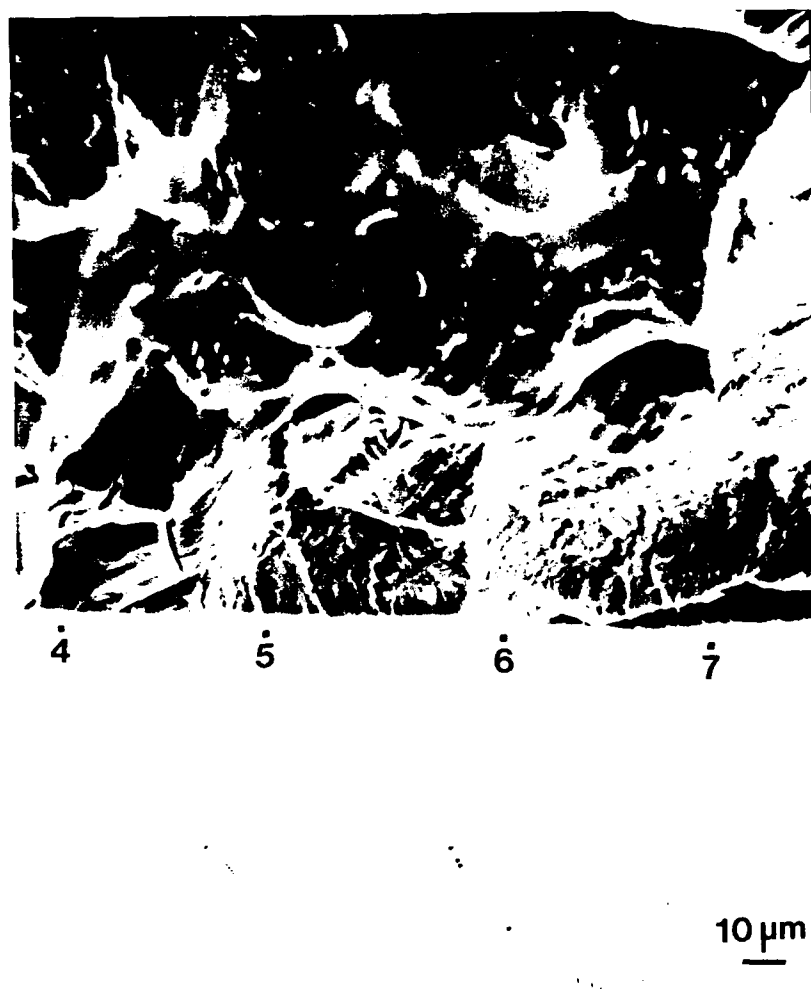


Fig. 2 A portion of the bend test specimen fractured at 919 K showing locations of EBSD measurements and fracture mode in grains labeled 4-7.

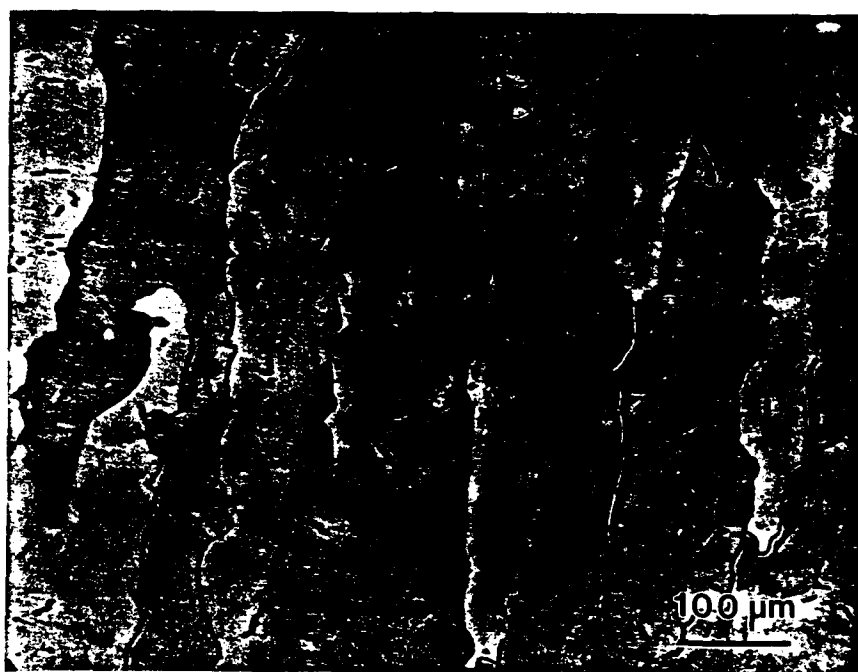


Fig. 3 Microstructure of the Al₆₇Cr₈Ti₂₅ alloy after the HIPing treatment.

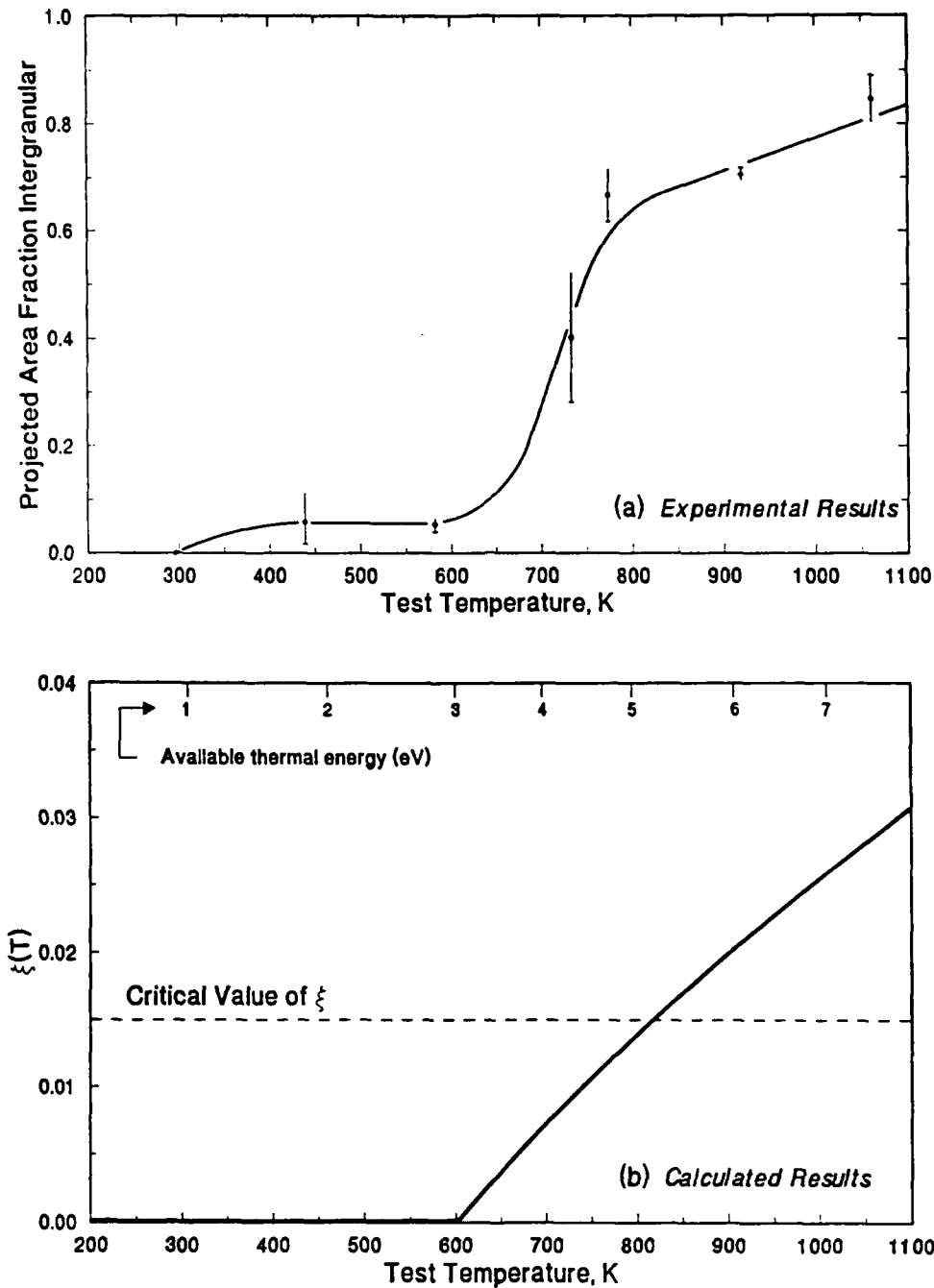


Fig. 4 a) Filled circles represent the projected area fraction of intergranular fracture as a function of test temperature. The ends of the vertical bars represent the projected area fractions of intergranular fracture on the tension halves ("T"-shaped end) and compression halves (plain end) of the bend specimen fracture surfaces. b) The effect of thermal energy on the fractional angular range corresponding to spontaneous or thermally activated dislocation emission, $\xi(T)$, for $\text{Al}_{67}\text{Cr}_8\text{Ti}_{25}$.

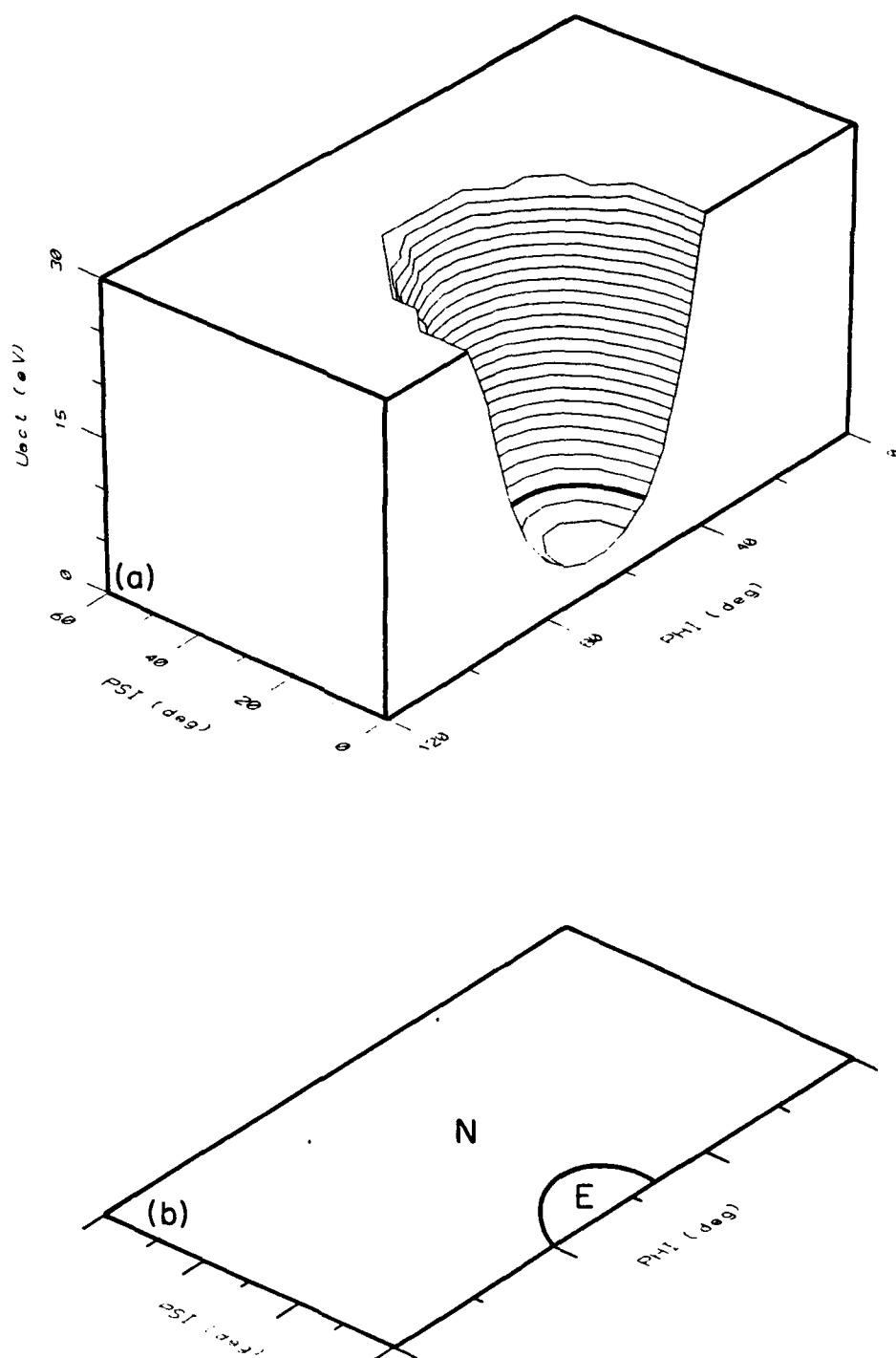


Fig. 5 a) The activation energy surface for dislocation emission as a function of the slip system orientation parameters ϕ and ψ_s for $\text{Al}_{67}\text{Cr}_8\text{Ti}_{25}$. b) A projection of the 3 eV activation energy contour onto the ϕ - ψ_s plane.

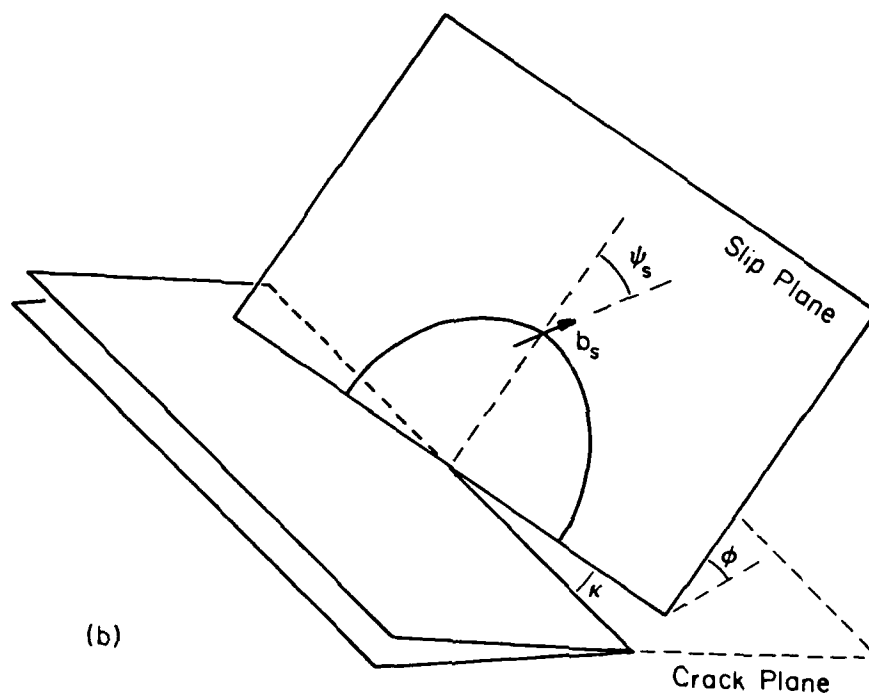
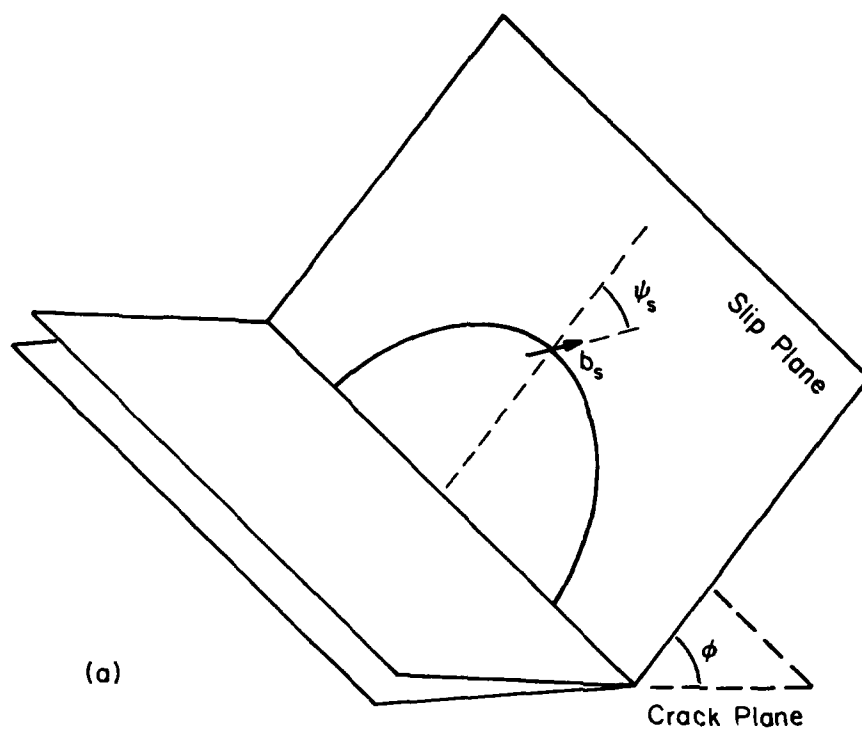


Fig. 6 a) Schematic diagram showing ideal crack/slip system geometry for dislocation emission models. b) Definition of the angle κ representing deviation from the ideal case.



Fig. 7 a) River markings on individual cleavage facets on the fracture surface of the bend specimen fractured at 439 K. b) River markings on individual cleavage facets on the fracture surface of the bend specimen fractured at 733 K. The notch is at the top of both fractographs.

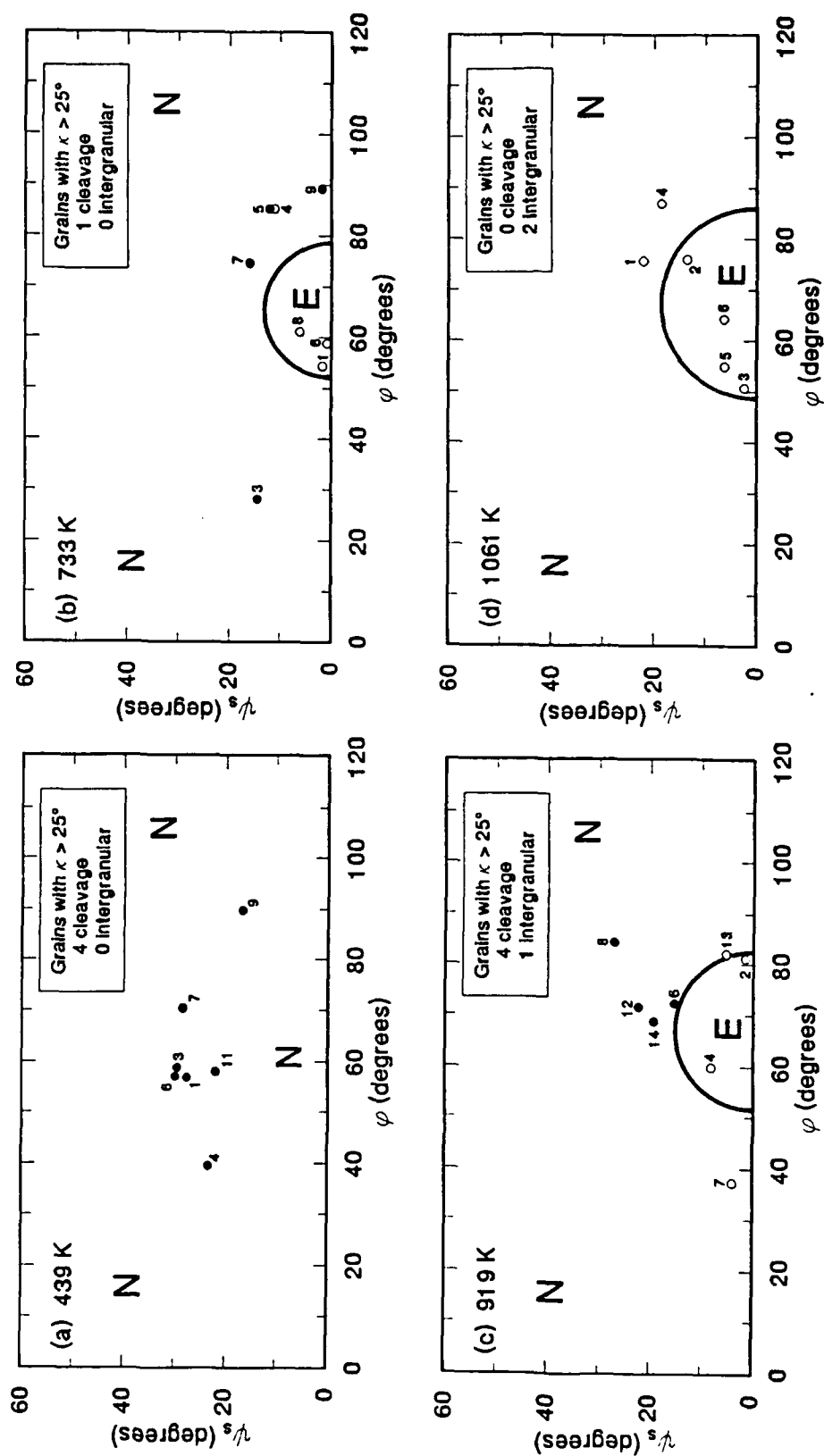


Fig. 8 The ϕ - ψ_s plane for 4 test temperatures showing DEM results and experimental fracture mode observations for individual grains. Open circles represent grains that cleaved and filled circles represent grains that failed by intergranular fracture; small numbers indicate the grain number. Regions labeled "E" represent ϕ - ψ_s combinations where spontaneous or thermally activated dislocation emission is favorable; emission is unfavorable in regions labeled "N".

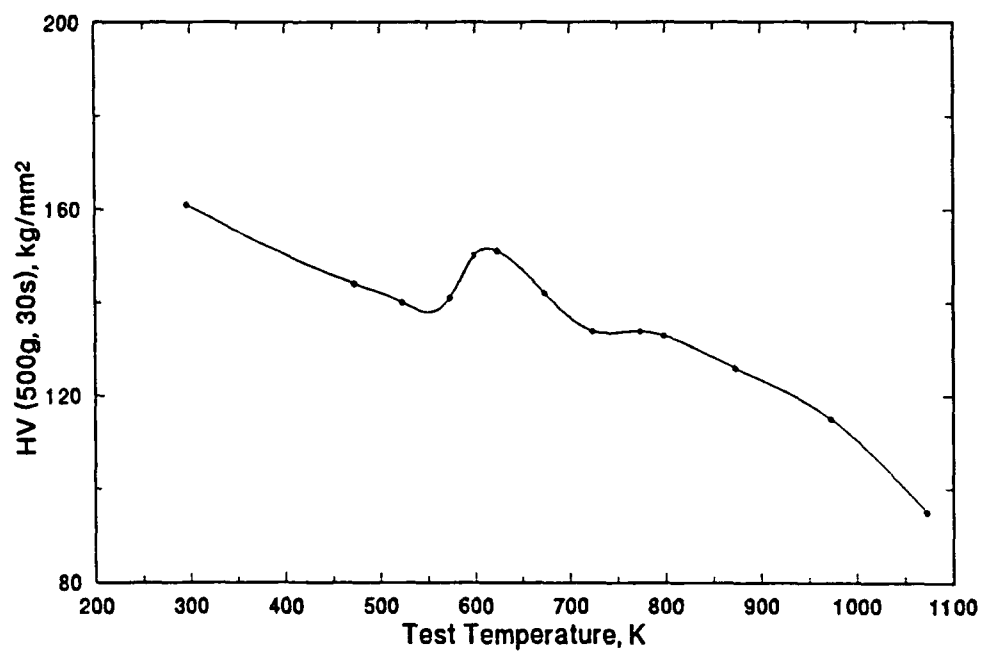


Fig. 9 Elevated temperature microhardness measurements for $\text{Al}_{67}\text{Cr}_8\text{Ti}_{25}$.

3. Creep of TiAl/Ti₃Al Alloys with Lamellar Microstructures

Summary: The research described in Section 3 was primarily motivated by preliminary creep results revealing that a two-phase TiAl/Ti₃Al alloy possessing a lamellar microstructure has a lower minimum creep rate than either of its constituent single phase alloys. The results of this investigation are presented in two parts:

- (1) The paper in Section 3.1 presents the results of a systematic series of creep tests on single-phase TiAl, single-phase Ti₃Al and the two-phase TiAl/Ti₃Al lamellar alloy.
- (2) The paper in Section 3.2 describes further experiments and theoretical analyses conducted to understand the superior creep resistance of the two-phase TiAl/Ti₃Al lamellar alloy.

The minimum creep rates of the two-phase TiAl/Ti₃Al lamellar alloy and the constituent TiAl and Ti₃Al single phase alloys were determined by compression creep tests for temperature and stress ranges of 980 K to 1130 K and 100 MPa to 700 MPa, respectively. For the temperature and stress ranges tested, all of the alloys within the scope of this study exhibit stress exponents commonly associated with power law creep. The experimentally determined values of stress exponent and activation energy for the single phase alloys agree well with the results of previous investigators. The two-phase TiAl/Ti₃Al lamellar alloy was found to possess a lower minimum creep rate over a large stress range than either of its two constituent single phase alloys. Additionally, compared with the two single-phase alloys, the two-phase TiAl/Ti₃Al lamellar alloy exhibits a very small primary creep strain. A low minimum creep rate and minimal primary creep strain are important engineering requirements for potential high-temperature materials.

Fiducial line experiments were conducted to determine the creep rates of the TiAl and Ti₃Al constituent phases within the two-phase TiAl/Ti₃Al lamellar microstructure. It was found that the creep rates of the constituent phases in the lamellar microstructure are more than an order of magnitude lower than the creep rate of the same phases tested as single-phase alloys. The lower creep rate of the two-phase TiAl/Ti₃Al lamellar alloy is attributed to enhanced strain hardening of the constituent phases within the lamellar microstructure. The fiducial line experiment also demonstrated that no

interfacial sliding of the phases in the two-phase TiAl/Ti₃Al lamellar alloy occurs during creep. Using the experimental results, a composite strength model has been formulated to predict the steady-state creep rate of the lamellar alloy. The model is based on principles analogous to those used by Kelly and Street in formulating a creep model for discontinuous fiber reinforcement, but the present model is adapted to the lamellar microstructure found in the TiAl/Ti₃Al alloy. The model shows that the lamellar reinforcement morphology benefits creep strength to a lesser degree than the discontinuous fiber reinforcement morphology. Application of the model yields very good correlation between predicted and experimentally observed minimum creep rates. Additionally, model predictions of the stress exponent and activation energy for creep of the two-phase TiAl/Ti₃Al lamellar alloy agree well with the experimentally determined values.

Accepted for publication in *Scripta. Metall. Mater.* (1993).

CREEP DEFORMATION OF A TWO-PHASE TiAl/Ti₃Al LAMELLAR ALLOY AND THE INDIVIDUAL TiAl AND Ti₃Al CONSTITUENT PHASES

MICHAEL F. BARTHOLOMEUSZ, QIBIN YANG* AND JOHN A. WERT

Department of Materials Science and Engineering
University of Virginia, Charlottesville, VA 22903

* Institute of Metals Research
Wenhua Rd., Shenyang 11001J, P.R. China

Introduction

Two-phase TiAl/Ti₃Al alloys in which the constituent phases form a lamellar microstructure are reported to possess good combinations of low-temperature fracture toughness, tensile strength and fatigue resistance [1, 2]. However, information about the high-temperature creep properties of the two-phase TiAl/Ti₃Al alloys with lamellar microstructures (referred to as *lamellar alloys* in the remainder of the paper) is limited. Based on a simple rule of mixtures model of strength, it would be expected that the creep rates of the lamellar alloy would be between the creep rates of TiAl and Ti₃Al. Composite strengthening models of greater sophistication could be applied; they also predict that the strength of a composite is between the strengths of the constituent phases [3].

In contrast to composite model predictions of strength, Polvani and coworkers [4] found that the minimum creep rates of two duplex alloys, a γ/γ' nickel-base superalloy and NiAl/Ni₂AlTi, were significantly lower than the minimum creep rates of either of the constituent phases. They also reported that most dislocations in the two-phase NiAl/Ni₂AlTi alloy were contained within the semi-coherent interfacial dislocation networks between the two phases. Based on this observation they proposed that the creep rate is controlled by the rate at which dislocations moving through both phases are emitted and absorbed by the interphase dislocation networks. It is not known if this phenomenon is a general characteristic of duplex alloys possessing semi-coherent interfaces.

Power-law creep can be regarded as a competition between recovery and work hardening [8]. When a balance is achieved between the rates of these two processes, the material exhibits steady-state creep. An increase in the strain hardening rate promotes a lower steady-state creep rate. Rao and Tangri [5] found that two-phase TiAl/Ti₃Al lamellar alloys have a greater strain hardening rate at ambient and elevated temperatures than either of the individual constituent phases. This superior strain hardening rate can be primarily attributed to two factors: TiAl/Ti₃Al interfaces have been observed to be rich sources of mobile dislocations emitted into the TiAl phase, and interstitial impurities in the alloy strongly segregate to the Ti₃Al phase [5-7]. The effect of interstitial segregation to Ti₃Al is two-fold. First, it is proposed that removal of interstitial elements from TiAl reduces the anisotropy of the Peierls stress in this phase. This significantly increases slip and twin activity in TiAl within the lamellar alloy, compared to single-phase TiAl [5-6]. Second, enrichment of impurities in Ti₃Al within the lamellar alloy appears to enhance slip in this phase; specifically, the basal plane is rendered more favorable for slip [7].

The greater strain hardening rate of the lamellar TiAl/Ti₃Al alloy suggests that it may exhibit lower steady-state creep rates than the individual constituent phases. The objective of the present study is to evaluate the creep properties of a TiAl/Ti₃Al lamellar alloy and of the individual constituent phases. In this paper, the results of this investigation will be presented and compared with previously published results for this alloy system.

Experimental

Three intermetallic alloys were evaluated in this investigation: single-phase TiAl (49 mol.% Al), single-phase Ti₃Al (34 mol.% Al), and the lamellar alloy (44 mol.% Al). The compositions of the Ti₃Al and TiAl phases within the lamellar microstructure, measured by EDS methods, were 35 mol.% Al and 48 mol.% Al respectively. The alloys used in this study were produced by arc melting of elemental Ti and Al granules. The ingots were vacuum homogenized at 1439 K for 80 hours and HIPped to remove residual porosity. Compression test specimens were cut from the ingots and machined into rectangular prisms 1.5 x 1.5 mm² x 2 mm in height. Larger specimens were also prepared and tested to verify that the results obtained from the smaller specimens were reproducible and not affected by specimen size. All specimens were mechanically polished prior to compression creep testing.

Testing was carried out with a constant load creep frame using a LVDT extensometer to continuously record displacement. Tests were performed in air at stresses ranging from 100 to 700 MPa at temperatures ranging from 980 K to 1130 K. The compression fixture consisted of Al_2O_3 plates between platens of Inconel 625. End effects were avoided by lubricating the specimen contact surfaces with boron nitride. Before loading, the specimens were held at the test temperature for 1 hour, and during the creep tests the temperature was controlled to within ± 2 K. Some of the tests were carried out at constant load (single-stress tests); in other tests the load on the specimen was incrementally increased after achieving the minimum creep rate (stress-change tests). Both types of tests were conducted for the two single-phase alloys, TiAl and Ti_3Al . For these alloys, measured minimum creep rates were the same in single-stress and stress-change tests, suggesting that the minimum creep rate was not sensitive to the prior deformation in stress change tests. In contrast, only single-stress tests were conducted for the lamellar alloy since the minimum creep rate in this alloy was found to be dependent on prior deformation. In compression, values of stress, strain and creep rate are negative; however, throughout the remainder of this paper only the absolute values of these quantities will be reported.

Results

The microstructures of the single-phase TiAl and Ti_3Al alloys consist of equiaxed grains with mean linear intercept diameters of 230 μm and 280 μm respectively. In contrast to the large grain diameters of the single-phase alloys, the mean linear intercept diameter of the lamellar packets is 70 μm . Figure 1a is an optical micrograph of the microstructure of the lamellar alloy. In the optical micrographs the dark lamellae are TiAl phase, which constitutes about 64 volume percent of the alloy, and the light lamellae are Ti_3Al phase. The average true center-to-center spacing of the individual TiAl lamellae is 5.1 μm . The lamellar alloy also contains about 3 volume percent of small equiaxed grains of single-phase TiAl, homogeneously distributed throughout the microstructure. The quantitative metallographic techniques used to obtain these values are described in references [9-10].

Figure 2 shows a typical set of creep curves for TiAl, Ti_3Al and the lamellar alloy at 1080 K and a true stress of 290 MPa. There are two identifiable regimes in these compression creep curves. Primary creep occurs upon initial loading and is characterized by a period of decreasing creep rate at the start of the test. Compared

with the two single-phase alloys, the lamellar alloy exhibits a very small primary creep strain. Similar behavior has been reported for the duplex NiAl/Ni₂AlTi alloy [4]. According to McLean [8], primary creep strain is inversely dependent on the strain hardening rate; therefore, the superior strain hardening rate of the lamellar alloy is one possible explanation for the small amount of primary creep in this alloy compared with the two single-phase alloys. Minimal primary creep strain is an important engineering requirement for potential high-temperature materials.

Secondary creep is frequently characterized as the regime in which the creep rate attains a minimum value and remains nearly constant with increasing strain. In contrast to the single-phase alloys, the creep rate of the lamellar alloy is not constant with strain in the secondary creep regime. Instead, the creep rate of the lamellar alloy increases with total strain, possibly as a consequence of microstructural changes occurring during high-temperature deformation. The creep rate of the lamellar alloy in the secondary creep regime is a minimum for true strains less than 0.05. Therefore, the values of minimum creep rate reported for the lamellar alloy in the present paper are for true strains less than 0.05.

Figure 3 shows minimum creep rates as a function of true stress for single-phase TiAl and Ti₃Al and for the lamellar alloy at four test temperatures. Since the creep tests were carried out under constant load conditions, the values of true stress and true creep rate represented in Figure 3 were calculated from the load-displacement curves assuming constancy of volume during creep deformation. This assumption appears to be reasonable since optical metallography of the crept specimens revealed no voids or cracks.

A general constitutive equation for strain rate is frequently written [11]:

$$\dot{\epsilon} = A \sigma^n e^{-Q/RT} \quad (1)$$

where A is a pre-exponential factor, n is the stress exponent, and Q is the activation energy for creep. From the test results it is possible to determine average values of n and Q for the alloys investigated; the values are listed in Table I. For the stress and temperature ranges tested, all of the alloys within the scope of this study exhibit stress exponents commonly associated with power law creep [12]. It is notable that the activation energy for creep of the lamellar alloy is between the values of activation

energy of the two constituent phases, TiAl and Ti_3Al , whereas the stress exponent of the lamellar alloy is essentially the same as that of the Ti_3Al alloy.

Discussion

Figure 3 demonstrates that the lamellar alloy exhibits a lower minimum creep rate over a large stress range than either of its constituent phases. In particular, at the critical value of true stress where both of the constituent phases have the same creep rate, the creep rate of the lamellar alloy is approximately an order of magnitude lower. Composite strengthening models cannot account for this observation unless the creep properties of the TiAl and Ti_3Al phases in the lamellar alloy differ significantly from the creep properties measured for the individual single-phase alloys.

The lamellar alloy investigated in this study has a large surface area per unit volume of semi-coherent interphase interfaces. Transmission electron microscopy results (to be published in a later paper) reveal interfaces with a high density of dislocations. Additionally, the Ti_3Al phase in the lamellar structure demonstrated a strong propensity for basal slip. These observations are consistent with the reports of previous investigators and clearly indicate the importance of the contribution of the interphase interface to the creep properties of the lamellar alloy [5, 7, 13-14].

The values listed in Table I for creep of the single-phase TiAl alloy are in good agreement with previously published results for Ti-50 mol.% Al alloys possessing large grain diameters ($n=7.9$ and $Q=427$ kJ/mol) [15-16]. The values of these parameters for TiAl alloys are reported to be quite sensitive to factors such as grain size, stoichiometry and total strain [15-16]. The activation energy for creep in TiAl alloys is substantially higher than the activation energy for lattice diffusion, suggesting that processes more complex than simple lattice diffusion control creep in this alloy [16].

Mendiratta and coworkers [17] separated their creep measurements for single-phase Ti_3Al into two stress exponent regimes. The stress exponent had a value of between 4.3 and 5.0 for stresses above 138 MPa, and between 2.3 and 2.5 for stresses below 138 MPa. The tests conducted on Ti_3Al in the present study belong to the higher stress regime, and the value of the stress exponent determined is in fair agreement with the previously reported value [17]. The value of activation energy for creep of Ti_3Al obtained in our experiments (352 kJ/mol) is larger than that reported

previously (206 kJ/mol) [17].

Figure 3 demonstrates that, within the stress and temperature ranges investigated in the present study, single-phase Ti_3Al exhibits higher minimum creep rates than single-phase TiAl . In contrast, the Ti_3Al alloy previously investigated appears to have comparable or lower minimum creep rates than the TiAl alloy in the present study [17]. The aluminum content of the Ti_3Al alloy tested by Mendiratta et al. (25 mol.% Al) is considerably lower than that of the Ti_3Al alloy tested in the present study. It is possible that the difference in alloy stoichiometry, in addition to unreported differences in impurity content, could account for the differences in creep rates. The composition of the Ti_3Al alloy used in the present study is essentially the same as the composition of the Ti_3Al phase in the lamellar alloy. Therefore, it is not unreasonable to expect that the creep behavior of the single-phase Ti_3Al alloy tested in the present study is more representative of the creep response of the Ti_3Al phase in the lamellar alloy than the creep behavior of the Ti_3Al alloy tested by Mendiratta and coworkers.

The enhanced steady-state creep resistance characteristic of the lamellar $\text{TiAl/Ti}_3\text{Al}$ microstructure is compromised by the sensitivity of this microstructure to thermo-mechanical exposure. Prior to creep testing, each lamellar packet contains straight, parallel plates of TiAl and Ti_3Al , the interphase interfaces are semi-coherent, and the packet boundaries are well-defined (see Figure 1a). After testing, however, the individual lamellar plates are seen to have undergone substantial shearing and bending, and Figure 1b shows that the lamellar microstructure has begun to spheroidize in the interpacket regions. For true strains larger than 0.05, spheroidization of the lamellar microstructure is thought to increase the minimum creep rate of the alloy, as depicted in Figure 2. Microstructural evolution of lamellar alloys during creep testing and its effect on creep properties are the topics of a forthcoming paper.

Summary

Over large stress and temperature ranges, the minimum creep rate of the two-phase $\text{TiAl/Ti}_3\text{Al}$ lamellar alloy is lower than the minimum creep rates of both the constituent phases. Composite strengthening models cannot account for this observation unless the creep properties of the TiAl and Ti_3Al phases in the lamellar alloy differ significantly from the creep properties measured for the individual single-phase alloys.

Acknowledgements

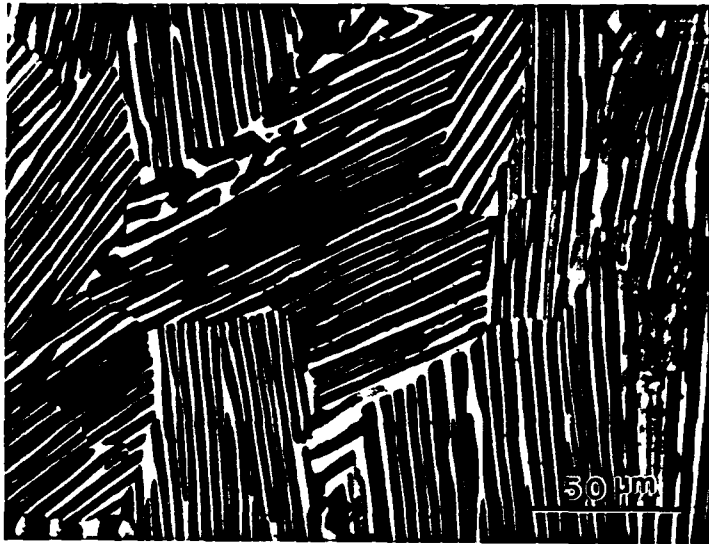
The authors are grateful to Prof. T. H. Courtney and Dr. K.S. Kumar for their insightful comments. We would also like to express our appreciation to S. Zambo, P. Ratnaparkhi and H. Koenigsmann for their technical assistance. This work was sponsored by AOFSR under contract number AFOSR-90-0143; Dr. A. Rosenstein was the contract monitor.

References

1. Y.W. Kim and D.M. Dimiduk, JOM, 43 no. 8 (1991) 40-47.
2. S. Mitao, S. Tsuyama and K. Minakawa, Mater. Sci. Eng., A143 (1991) 40-47.
3. A. Kelly and K.N. Street, Proc. Roy. Soc. Lond., A328 (1972) 283-293.
4. R.S. Polvani, W.-S. Tzeng and P.R. Strutt, Metall. Trans., 7A (1976) 33-40.
5. P. Prasad and Kris Tangri, Mater. Sci. Eng., A132 (1991) 49-59.
6. V.K. Vasudevan, M.A. Stucke, S.A. Court and H.L. Fraser, Philos. Mag. Let., 59 (1989) 299-307.
7. S.A. Court, J.P.A. Lofvander, M.H. Loretto and H.L. Fraser, Philos. Mag., 61 (1990) 109-139.
8. D. McLean, Progress in Physics, 29 (1966) 1-33.
9. G.E. Pellissier, M.F. Hawkes, W.A. Johnson and R.F. Mehl, Trans ASM, 30 (1942) 1049-1086.
10. E. Underwood, in *Metals Handbook*, vol. 8 (ASM, Metals Park, Ohio, 1973), 37-47.
11. A.K. Mukherjee, J.E. Bird and J.E. Dorn, Trans. A.S.M., 62 (1969) 155-179.
12. H.J. Frost and M.F. Ashby, *Deformation-Mechanism Maps*, (Pergamon Press Ltd, Oxford, 1982), 11-12.
13. C.R. Feng, D.J. Michel and C.R. Crowe, Mater. Sci. Eng., A145 (1991) 257-264.
14. H.A. Lipsitt, D. Shechtman and R.E. Schafrik, Metall. Trans., 11A (1980) 1369-1375.
15. T. Takahashi, H. Nagai and H. Oikawa, Mater. Sci. Eng., A128 (1990) 195-200.
16. H. Oikawa, in *High Temperature Aluminides & Intermetallics*, edited by S.H. Wang, C.T. Liu, D.P. Pope and J.O. Stiegler (TMS, Warrendale, PA, 1989), 353-373.
17. M.G. Mendiratta and H.A. Lipsitt, J. Mater. Sci., 15 (1980) 2985-2990.

Table I
Experimentally determined values of the
stress exponent and activation energy for creep

Material	n	Q(kJ/mol)
TiAl	7.8	435
Ti ₃ Al	5.5	352
Lamellar	5.4	407



(a)



(b)

Figure 1. Optical microstructures of the lamellar alloy. (a) Prior to creep deformation.
(b) After creep testing at 1030 K to a true strain of 0.24.

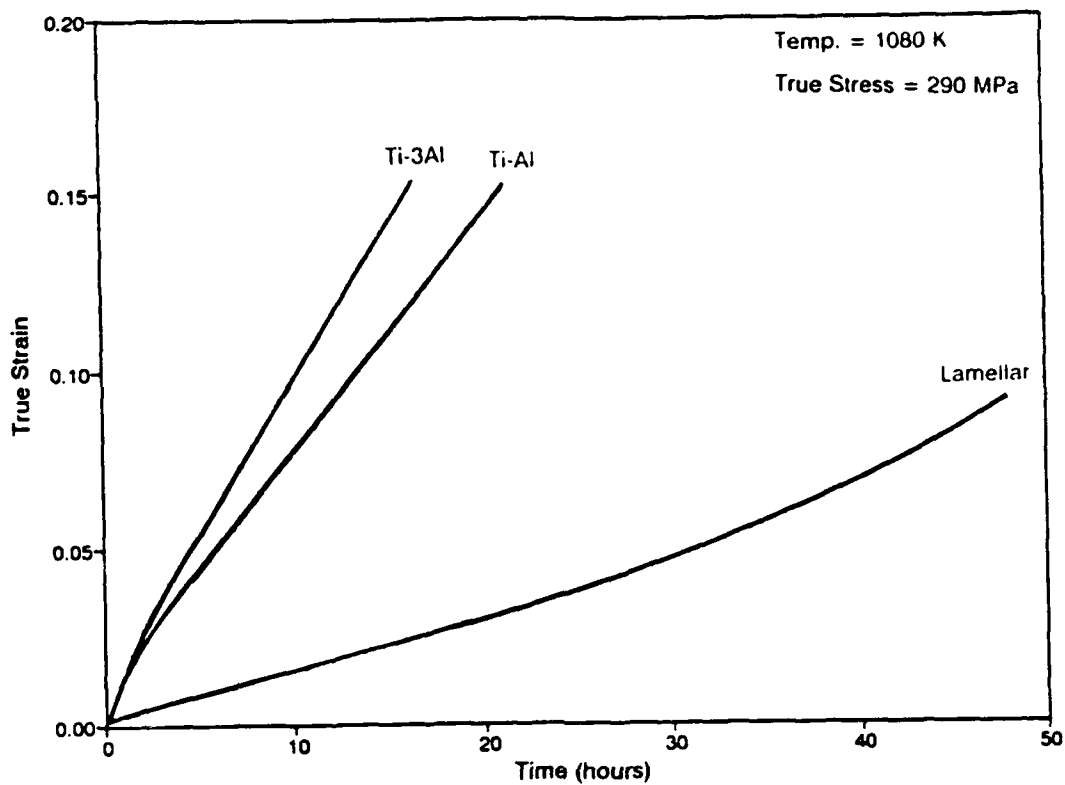
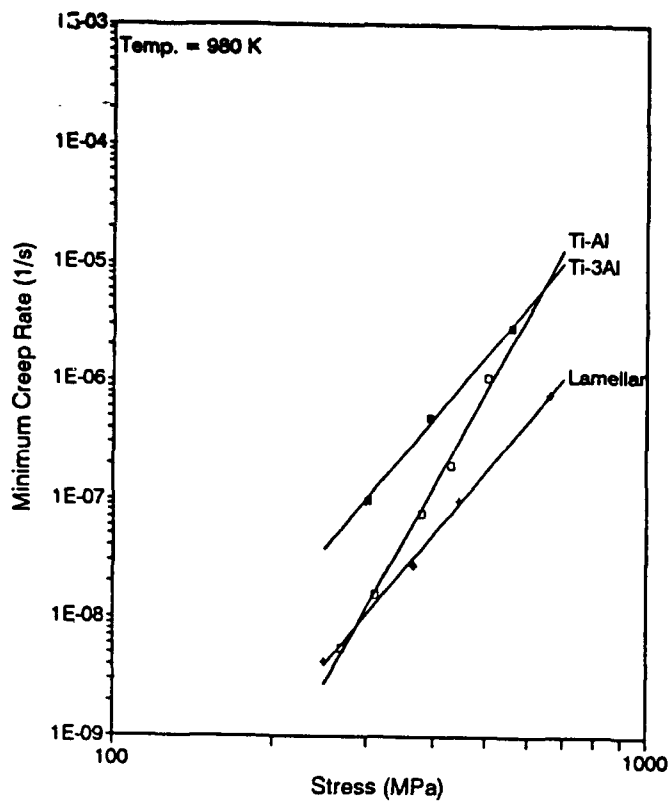
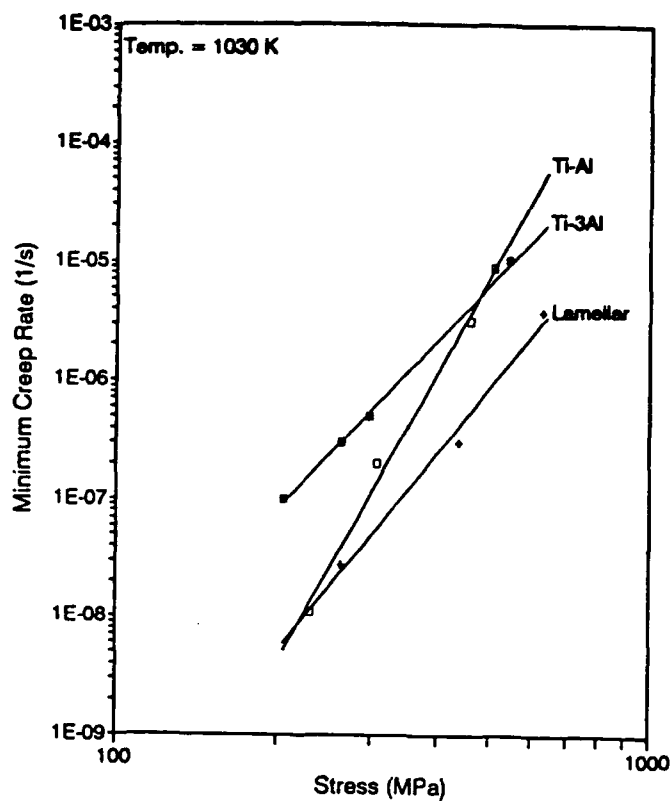


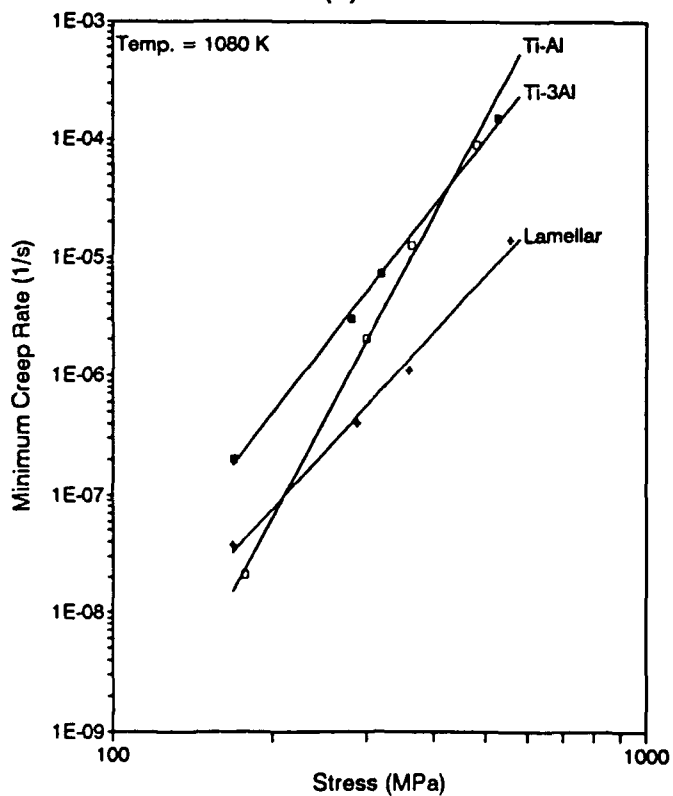
Figure 2. Creep curves for TiAl, Ti₃Al and the lamellar alloy.



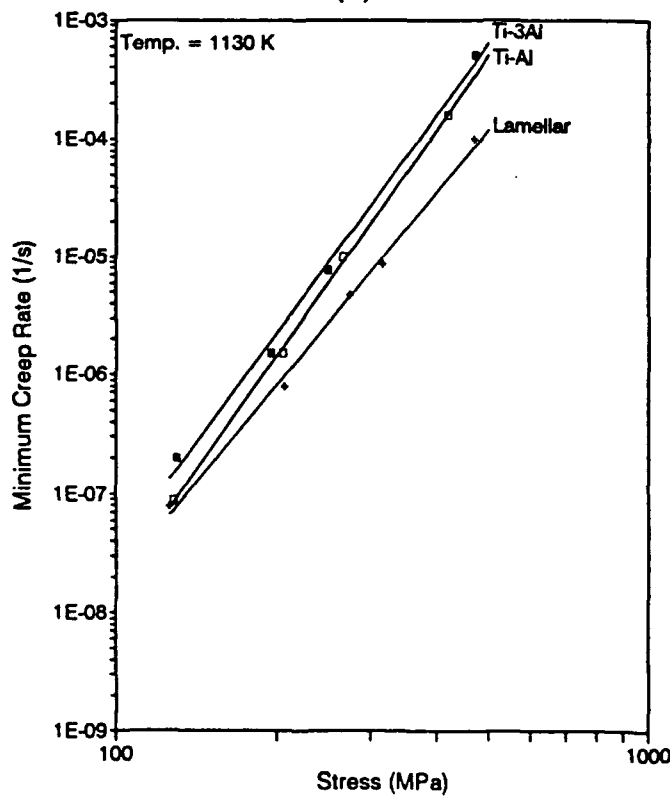
(a)



(b)



(c)



(d)

Figure 3. Minimum creep rate as a function of stress for the three alloys investigated.

(a) 980 K (b) 1030 K (c) 1080 K (d) 1130 K

Submitted to *Acta. Metall. Mater.* (1993)

MODELING CREEP DEFORMATION OF A TWO-PHASE
TiAl/Ti₃Al ALLOY WITH A LAMELLAR MICROSTRUCTURE

MICHAEL F. BARTHOLOMEUSZ AND JOHN A. WERT

Department of Materials Science and Engineering

University of Virginia, Charlottesville, VA 22903

Abstract

A two-phase TiAl/Ti₃Al alloy with a lamellar microstructure has been shown to exhibit a lower minimum creep rate than the minimum creep rates of the constituent TiAl and Ti₃Al single-phase alloys. Fiducial line experiments demonstrate that the creep rates of the constituent phases within the two-phase TiAl/Ti₃Al lamellar alloy tested in compression are more than an order of magnitude lower than the creep rates of single-phase TiAl and Ti₃Al alloys tested in compression at the same stress and temperature. Additionally, the fiducial line experiments show that no interfacial sliding of the phases in the TiAl/Ti₃Al lamellar alloy occurs during creep. The lower creep rate of the lamellar alloy is attributed to enhanced strain hardening of the constituent phases within the lamellar microstructure. A composite strength model has been formulated to predict the creep rate of the lamellar alloy, taking into account the lower creep rates of the constituent phases within the lamellar microstructure. Application of the model yields a very good correlation between predicted and experimentally observed minimum creep rates over moderate stress and temperature ranges. Model predictions of the stress exponent and activation energy for creep of the two-phase TiAl/Ti₃Al lamellar alloy agree well with the experimentally determined values.

1. Introduction

The low density and good oxidation resistance of TiAl and Ti₃Al ordered intermetallic alloys make them attractive candidate materials for high temperature engineering applications [1, 2]. However, these alloys possess poor ductility at low and intermediate temperatures and are susceptible to rapid fatigue crack growth [1]. It has been shown by previous investigators that two-phase TiAl/Ti₃Al lamellar alloys exhibit an appreciably improved toughness and fatigue resistance compared to the constituent TiAl and Ti₃Al single-phase alloys [1, 3]. Furthermore, Bartholomeusz, Yang and Wert (BYW) [4] demonstrated that the minimum creep rate of a two-phase TiAl/Ti₃Al lamellar alloy (referred to as *the lamellar alloy* in the present paper), is lower than the creep rates of the constituent phases. The creep behavior of the TiAl/Ti₃Al lamellar alloy is not unique; several duplex alloys have been reported to possess lower creep rates than their constituent phases, most notably NiAl/Ni₂AlTi and γ/γ' nickel-base superalloys [5-7]. It has been proposed that this phenomenon is a general one associated with duplex alloys possessing semicoherent interfaces [5].

Polvani *et al.* [5] suggested that the lower creep rate of the duplex NiAl/Ni₂AlTi alloy with respect to its constituent phases is due to the retardation of dislocation climb at semicoherent interfaces separating the two phases. It is possible that such a mechanism is occurring in the TiAl/Ti₃Al lamellar alloy, but alternate mechanisms could also account for the experimental observations. For example, the phases in the lamellar microstructure may possess lower steady-state creep rates than the corresponding constituent single-phase alloys as a result of enhanced work hardening. Power-law creep can be regarded as a competition between recovery and work hardening [8, 9]. When a balance is achieved between these two processes, the material exhibits steady-state creep. Therefore, an increase in the work hardening rate, or a reduction in the recovery rate, can have the effect of reducing the steady-state creep rate.

Transmission electron microscopy (TEM) studies (to be published) reveal that the dislocation densities in the TiAl and Ti₃Al phases within the deformed lamellar microstructure are larger than in deformed samples of single-phase TiAl and Ti₃Al. There are several potential explanations for the increase in the dislocation density in the TiAl and Ti₃Al phases within the lamellar microstructure. First, the stresses generated at interfaces by structural ledges can be large enough to emit mobile dislocations [10]. TiAl/Ti₃Al interfaces have been observed to be rich sources of dislocations [11].

Second, segregation of interstitial impurities from the TiAl phase to the Ti_3Al phase has been reported to significantly increase slip and twin activity in the TiAl phase [11]. Finally, enrichment of impurities in the Ti_3Al phase appears to enhance slip in this phase; specifically, the basal plane is rendered more favorable for slip [12]. Assuming that the recovery rate is less sensitive to the lamellar character of the microstructure than the work hardening rate, the increased density of dislocations and dislocation sources in the TiAl and Ti_3Al phases within the lamellar microstructure would cause the lamellar alloy to possess a lower creep rate than the individual constituent phases. This conjecture is consistent with Weertman's model [13] for power-law creep in which the steady-state creep rate is inversely proportional to the density of dislocation sources.

In the results reported by BYW, the grain sizes of the TiAl and Ti_3Al alloys tested were 230 and 280 μm , respectively. For these grain sizes and at low to intermediate values of applied stress, TiAl has a lower minimum creep rate than Ti_3Al at the same temperature and applied stress. Oikawa and coworkers [14, 15] conducted several creep tests on single-phase TiAl alloys possessing different grain diameters and found a strong dependence of minimum creep rate on grain size. Inspection of Oikawa's results reveals that TiAl alloys with 32 μm grain diameter always exhibit a higher minimum creep rate than the Ti_3Al alloy tested by BYW at the same temperature and applied stress. The average dimension of the TiAl phase within the lamellar microstructure is 37 μm . It is not known whether the grain size effect on the steady-state creep rate of TiAl carries through to the lamellar microstructure.

The preceding summary of prior observations demonstrates that the mechanism(s) underlying the superior creep properties of the TiAl/ Ti_3Al lamellar alloy are not understood. The objective of the present paper is to characterize the creep behavior of the TiAl and Ti_3Al phases within the lamellar microstructure, and to demonstrate that the steady-state creep rate of the lamellar alloy can be predicted using a composite strengthening model. Sections 2 through 4 are devoted to experimental determination of the creep behavior of the TiAl and Ti_3Al constituent phases within the lamellar microstructure. These experimental results are then used in a creep strength model developed in the remainder of this paper.

2. Experimental Methods

Details concerning preparation of the alloys used in this study have been previously reported [4]. To characterize the creep behavior of the constituent TiAl and Ti₃Al phases within the lamellar microstructure, the following experiments were conducted. One face of a compression creep specimen, measuring 1.5 x 1.5 mm² x 2 mm, was polished using 0.05 μ m alumina powder. By carefully touching the polished face of the specimen to a spinning polishing wheel containing 1 μ m alumina powder, an array of fine fiducial lines was scratched onto the surface. The scratched face was lightly etched to enable secondary electron imaging of the polished surface in the scanning electron microscope (SEM). Careful measurements were taken with respect to the initial orientations and positions of several of the fiducial lines. The sample was then crept in compression at 1080 K in a vacuum hot press under an average applied stress of 350 MPa for 7 hours. The total true strain of the sample at the end of the test was 0.044. The same preparation procedure was used for a second sample, which was crept in compression at 1080 K under an average applied stress of 380 MPa for 10.3 hours. The total true strain at the end of this test was 0.078. To prevent oxidation from obscuring the fiducial lines, these tests were conducted in a vacuum hot press, instead of the creep test fixture used to obtain the creep data presented by BYW. After testing, the orientations and positions of the fiducial lines were recorded using the SEM.

3. Experimental Results

Figure 1 is an optical micrograph of the lamellar alloy prior to testing. Each packet in the lamellar alloy consists of alternating TiAl and Ti₃Al lamellae. The darker lamellae are TiAl phase. The average packet diameter is 70 μ m and the true thickness of the TiAl lamellae is 3.3 μ m. Thus the average dimension of the TiAl phase is approximately 37 μ m. BYW reported that, over large stress and temperature ranges, the minimum creep rate of the two-phase TiAl/Ti₃Al lamellar alloy is lower than the minimum creep rates of either of the constituent single-phase alloys. Figure 2 illustrates the results of BYW for the creep tests at 1080 K. The grain sizes of the TiAl and Ti₃Al alloys represented in Figure 2 are 230 μ m and 280 μ m, respectively. The values of minimum creep rate for the lamellar alloy in Figure 2 were obtained at true strains less than 0.05.

Figure 3a is a SEM micrograph of a portion of the polished specimen face containing fiducial lines, prior to testing to a true strain of 0.044. The width of the fiducial lines is significantly smaller than the width of the TiAl and Ti₃Al lamellae, ensuring accurate observation of the deformation of the fiducial lines within the phases and at the interphase interfaces. Figure 3b is a SEM micrograph of the fiducial lines after compression creep testing to a true strain of 0.044. The darker and mottled phase in the SEM micrographs is the TiAl phase; its mottled appearance is an artifact of the etching process. The fiducial lines are clearly continuous across interphase interfaces and are also continuous across lamellar packet boundaries. The displacement of the fiducial lines within the constituent phases of the lamellar alloy tested to a true strain of 0.044 was very slight and quantitative determination of the local strains necessitated evaluation of the lamellar alloy crept to a true strain of 0.078.

Figure 4a is a SEM micrograph of a portion of the polished specimen face containing a fiducial line prior to testing to a true strain of 0.078. The fiducial line in Figure 4a is 58° from the compression axis and is straight along its entire length. Figure 4b depicts the same fiducial line, passing through the lamellar packet marked "a" in Figure 4a, after creep testing to a true strain of 0.078. The orientation of the fiducial line prior to testing is marked on Figure 4b. In the bottom left corner of Figure 4b, the two lines almost coincide. However, in the top right corner of Figure 4b there is a significant difference in the positions of the two lines and the orientation of the fiducial lines is noticeably different in the two phases. After testing, the fiducial lines are continuous across interphase interfaces.

Although the creep test was conducted in a vacuum hot press, the vacuum during the test was not better than 5 Pa. Furnace debris and some limited oxidation marred the surface of the sample tested to a true strain of 0.078 and permitted evaluation of only those lamellar packets for which the position of the fiducial line could be positively discerned. In all, five lamellar packets possessing lamellae orientations ranging from 0° to 60° with respect to the compression axis were evaluated. In the five lamellar packets evaluated, the angle between the compression axis and fiducial line in the TiAl phase was always greater than the same angle in the Ti₃Al phase. The average orientations of the fiducial lines in the TiAl and Ti₃Al phases with respect to the compression axis were 61.8° and 59.5° respectively. This result demonstrates that, during the creep test, the TiAl phase strained more, and therefore possessed a higher creep rate than the Ti₃Al phase.

4. Interpretation of Experimental Results

Evaluation of the orientations of the fiducial lines in the two phases within the lamellar microstructure demonstrates that, under the same external stress, the TiAl phase in the lamellar microstructure creeps more rapidly than the Ti₃Al phase in the lamellar microstructure. This conflicts with previously reported observations of creep rates of single-phase TiAl and Ti₃Al which show that coarse-grain TiAl creeps less rapidly than coarse-grain Ti₃Al at the same stress and temperature, for low to intermediate values of applied stress [4]. Several factors could account for this difference. For example, the effective dimensions of the phases in the lamellar alloy are much smaller than the grain sizes of the single-phase alloys. Oikawa *et al.* [14, 15] have shown that reducing the grain size of TiAl increases the steady-state creep rate in the temperature and stress regime used in the present study. However, if reduced grain size increases the creep rate of TiAl, it is even more difficult to understand the low creep rate of the lamellar alloy. The grain size dependence of creep rate for Ti₃Al has not been reported, so it is not possible to identify the role of grain size in this case. Figure 5a shows the minimum creep rate for the fine-grain TiAl alloy tested by Oikawa *et al.* (average grain diameter of 32 μm) compared with the minimum creep rates of the lamellar alloy and the Ti₃Al alloy tested by BYW.

Alloy stoichiometry is known to affect creep of TiAl and Ti₃Al [4, 14-17]. However, in the present study, the single-phase alloy compositions were selected to match closely the compositions of the two phases in the lamellar alloy. Therefore, it is unlikely that the low creep rates of the lamellar alloy can be accounted for by alloy stoichiometry.

Since considerations of grain size and phase stoichiometry are unable to explain the creep behavior of the lamellar alloy, further analysis of the fiducial line experiments is necessary. Assuming constant volume during creep deformation, the change in orientation of the fiducial lines can be related to the tensile strain by:

$$\epsilon = 1 - \left(\frac{\tan\theta_0}{\tan\theta} \right)^{2/3} \quad [1]$$

where θ_0 and θ represent the orientations of the fiducial line before and after testing. Previous results indicate that the lamellar alloy exhibits a negligible amount of primary

creep strain [4, 18]. Therefore, the assumption that most of the deformation during the present creep test of the lamellar alloy resulted from steady-state creep is reasonable. If the duration of the creep test is known, the strain rates for the constituent phases within the lamellar microstructure can be calculated from Eq. 1. Furthermore, the average strain rate of the lamellar alloy can be calculated by invoking a rule of mixtures argument to correctly account for the contribution of each constituent phase.

Table I presents the average strain rate of the lamellar alloy and the strain rates of the TiAl and Ti₃Al phases within the lamellar microstructure calculated using the fiducial line method, and the strain rates of the lamellar alloy and single-phase TiAl and Ti₃Al alloys obtained from compression creep tests. The average steady-state creep rates of the lamellar alloy measured using the two different techniques are in good agreement. The value calculated using the fiducial lines is slightly higher, probably due to the incorporation of a small amount of primary creep strain in the calculation. It is remarkable that the strain rate of the lamellar alloy calculated on the basis of creep in only five lamellar packets agrees so well with the macroscopic strain rate. The most significant result in Table I is that the creep rates of the constituent phases in the lamellar microstructure are more than an order of magnitude lower than the same phases tested as single-phase alloys.

Polvani and coworkers [5] reported that the overwhelming majority of dislocations in a NiAl/Ni₂AlTi duplex alloy were contained within interfacial networks. Very few dislocations were present within the single-phase regions. They consequently proposed that the lower creep rate of the NiAl/Ni₂AlTi duplex alloy relative to its constituent phases was due to the emission and absorption rates of dislocations moving through both phases by the interfacial dislocation networks. By acting as physical barriers to dislocation climb, the interfacial dislocation networks were proposed to endow the duplex alloy with a lower creep rate than its constituent phases. There are two observations which suggest that a different mechanism controls the lower creep rate of the TiAl/Ti₃Al lamellar alloy with respect to its constituent phases.

First, the average separation between interfacial dislocation networks in the lamellar alloy is 2.6 μm , more than an order of magnitude greater than the average interfacial network separation in the NiAl/Ni₂AlTi duplex alloy [5]. The average value of interfacial network separation in the lamellar alloy suggests that a significant fraction of climbing dislocations never encounter an interphase interface during creep. This result

indicates that the role of the interfacial networks in blocking dislocation climb is probably not as dominant an effect in the TiAl/Ti₃Al lamellar alloy as it is in the NiAl/Ni₂AlTi duplex alloy.

Second, in contrast to the observations made for the NiAl/Ni₂AlTi duplex alloy [5], the individual phases of the lamellar alloy possess significant dislocation densities, as demonstrated in the transmission electron micrograph in Figure 6. As discussed in the Introduction, the relatively high density of dislocations can be directly related to the lower steady-state creep rates of the constituent phases in the lamellar microstructure. Therefore, the superior creep resistance of the lamellar alloy in this investigation could result from enhanced strain hardening of the constituent phases when they are present in the lamellar microstructure.

These experimental results suggest that enhanced strain hardening of the constituent phases in the lamellar alloy dominates the creep response of the lamellar alloy, whereas in the NiAl/Ni₂AlTi duplex alloy [5] the reinforcing contribution of the interfacial networks appears to control the creep response. The creep rate of the duplex Ni₂AlTi alloy is three orders of magnitude smaller than the creep rates of its constituent phases. This is a substantially larger difference than that found between the lamellar alloy and its constituent phases. This comparison suggests that obstruction of climbing dislocations by interfaces produces a greater reduction in the creep rate than enhanced strain hardening of the constituent phases, provided that the interface spacing is sufficiently small. The natural extension of this proposal is that if the TiAl/Ti₃Al lamellar alloys can be fabricated to possess smaller interfacial separations, on the order of those in the NiAl/Ni₂AlTi alloy studied by Polvani and coworkers [5], the creep rate may be further reduced. Similarly, several investigators have demonstrated that microstructural refinement in metal matrix composites can lead to a significant reduction in the creep rate as a result of interactions between gliding dislocations and the reinforcing phase [19, 20].

In Figure 5b, the steady-state creep rate is shown as a function of stress for the constituent phases, modified to reflect the additional hardening associated with the

lamellar microstructure. In this figure:

$$\begin{aligned}\dot{\epsilon}_{\gamma}' &= \frac{\dot{\epsilon}_{\gamma}}{\chi_{\gamma}}, \\ \dot{\epsilon}_{\alpha 2}' &= \frac{\dot{\epsilon}_{\alpha 2}}{\chi_{\alpha 2}}\end{aligned}\quad [2]$$

where $\dot{\epsilon}_{\gamma}'$ and $\dot{\epsilon}_{\alpha 2}'$ represent the creep rates of the TiAl and Ti₃Al phases within the lamellar microstructure determined from the fiducial line experiments, and $\dot{\epsilon}_{\gamma}$ and $\dot{\epsilon}_{\alpha 2}$ are the creep rates of single-phase TiAl and Ti₃Al alloys determined from compression creep tests. χ_{γ} and $\chi_{\alpha 2}$ are the strain hardening factors having values of 20 and 25 for the TiAl and Ti₃Al phases in the lamellar alloy. These hardening factors were determined by taking the ratios of the creep rates found for the single-phase alloys using conventional creep experiments, and the creep rates found for the individual phases in the lamellar alloy using the fiducial line experiment. Figure 5b clearly shows that, by accounting for the enhanced hardening effect, the creep rate of the lamellar alloy lies between the creep rates of its constituent phases. This result implies that creep of the lamellar alloy may be modeled by a constitutive relationship of the type frequently used for composite materials. In the remainder of this paper, a composite strengthening model will be developed to predict the steady-state creep response of the lamellar alloy.

5. Model

Kelly and Street (KS) [21] modeled steady-state creep deformation of a composite containing uniaxially aligned discontinuous fibers. The basic premise of the KS model is that bonding at the matrix/reinforcement interface results in the retardation of creep in the matrix phase adjacent to the interphase interface. The lower creep rate of the matrix adjacent to the interface produces a shear stress across the interface, resulting in load transfer from the matrix to the reinforcements. Sliding of the interface is also taken into account in the KS model. Application of the KS model to several metal matrix composite systems revealed good agreement between model predictions of composite creep properties and experimental results [21-24].

Each packet in the TiAl/Ti₃Al lamellar alloy consists of alternating plates, or lamellae, of TiAl and Ti₃Al, a geometry different from that modeled by KS. In the present

paper, the KS analysis is presented in modified form to specifically address steady-state creep of a lamellar microstructure consisting of randomly oriented lamellar packets. In a lamellar microstructure with similar volume fractions of the two phases, the morphologies of the reinforcing and matrix phases are virtually identical. For model development, it is convenient to use the terms *matrix* and *reinforcement*, even though the concept of a continuous matrix phase is not applicable to the lamellar microstructure. The effect of the reinforcing phase on retardation of flow in the matrix is a maximum for lamellae oriented parallel to the applied stress. In contrast, when the lamellae are oriented normal to the applied stress, the reinforcing phase does not significantly constrain flow of the matrix phase. Therefore, lamellar packets oriented parallel and perpendicular to the applied stress represent the upper and lower creep strength bounds for the lamellar alloy [25, 26]. In the remainder of Section 5 of the present paper, the KS model is adapted for use with the lamellar phase morphology. The two limiting cases are considered first, followed by the general case. Figure 7 depicts the two limiting cases; $\dot{\epsilon}_m$ and $\dot{\epsilon}_r$ represent displacement rates in the matrix and reinforcing phases respectively. In Figure 7a, the combined effect of the reinforcement displacement rate and the interfacial sliding velocity, $\dot{\epsilon}_s$, is represented by $\dot{\epsilon}_i$.

5.1 Discontinuous lamellae oriented parallel to the uniaxial stress.

The strength of the lamellar composite, σ_c , can be expressed in terms of the average strength of the discontinuous reinforcing lamellae, $\bar{\sigma}_r$, the strength of the matrix phase, σ_m , and the volume fractions of the respective phases, V_r and V_m :

$$\sigma_c = \bar{\sigma}_r V_r + \sigma_m V_m . \quad [3]$$

In the context of creep deformation, strength signifies the stress required to maintain a steady-state strain rate at a given temperature. Evaluation of the term describing the average stress in the discontinuous reinforcing lamellae is fairly involved. The original Kelly and Street [21] model outlines a procedure for evaluating this stress in the case of uniaxially aligned discontinuous fibers. In the following paragraphs, the salient steps of a similar derivation for the case of uniaxially aligned discontinuous lamellae are described.

As in the original KS analysis, the difference in displacement rate of the matrix at the interphase interface and at a distance h from the interface is:

$$\Delta v = \dot{u}_m - \dot{u}_i \quad [4]$$

where

$$\dot{u}_m = \dot{\epsilon}_m z$$

$$\dot{u}_i = \dot{u}_r + \dot{u}_s$$

$$\dot{u}_s = \eta(\dot{u}_m - \dot{u}_r)$$

and z is distance measured parallel to the interface (see Figure 7a). The factor η varies between 0 and 1, depending on whether the bonding at the interface is perfect or nonexistent. The experimental results described in Section 3 of the present paper show that no detectable interfacial sliding occurs in the lamellar alloy for the true strains tested. Therefore, we take $\eta = 0$. The displacement rate gradient in the matrix results in a shearing rate adjacent to the interface, given by:

$$\dot{\gamma} = \frac{\Delta v}{h} = \frac{\dot{\epsilon}_m z - \dot{u}_r}{h} \quad [5]$$

where we now set h equal to one half the spacing between reinforcing lamellae. The parameter h can be expressed as:

$$h = \frac{t}{2} \frac{(1 - V_r)}{V_r} \quad [6]$$

where t is the thickness of the reinforcing lamellae. In Eq. 6, h is inversely proportional to the volume fraction of the reinforcing phase, whereas in the original KS model h is inversely proportional to the square root of the volume fraction of the reinforcing phase. Since V_r is a fractional quantity, for the same volume fraction of reinforcing phase, the displacement rate gradient in the matrix of a fiber-reinforced composite is greater than that in a lamellar composite. The relationship between tensile stress and creep rate for

the matrix phase is [21]:

$$\sigma_m = \sigma_{mo} \left(\frac{\dot{\epsilon}_m}{\dot{\epsilon}_{mo}} \right)^{1/m} \quad [7]$$

where m is the stress exponent of the matrix phase, and σ_{mo} and $\dot{\epsilon}_{mo}$ are constants. Using the relations $\sigma_m = 2\tau$, where τ is the local shear stress, and $\dot{\epsilon}_m = (2/3)\dot{\gamma}$ [21], the shear stress dependence on shear strain rate can be expressed as:

$$\dot{\gamma} = \frac{3}{2} \dot{\epsilon}_{mo} \left(\frac{2\tau}{\sigma_{mo}} \right)^m \quad [8]$$

Combining Eq. 5 through 8 yields:

$$\tau = \beta' \sigma_{mo} (\dot{\epsilon}_{mo})^{-1/m} (\dot{\epsilon}_m z - u_r)^{1/m} \quad [9]$$

where

$$\beta' = \frac{1}{2} \left(\frac{4}{3} \right)^{1/m} \left(\frac{V_r}{1 - V_r} \right)^{1/m}$$

Eq. 9 is the constitutive equation that represents the shear stress acting on any part of the reinforcing lamellae surface.

Figure 8 summarizes several approximations made in determining the creep rate of the reinforcing lamellae. The length of the lamellae is defined by the parameter L . Away from the ends of the reinforcing lamellae, $z < z_c$, the reinforcement and matrix phases are constrained to have the same strain rate, $\dot{\epsilon}_r = \dot{\epsilon}_m$. Creep of the reinforcing phase occurs slowly near the ends, $z > z_c$, because load transfer across the interface is insufficient to develop the required stress at the lamellae ends. The parameter z_c represents the critical length for maximum load transfer to the reinforcing lamellae. Kelly and Street [21] demonstrated that the transition between these two creep regimes is very steep for a reinforcing phase stress exponent, n , greater than 4. This is the case for the reinforcing phase in the TiAl/Ti₃Al lamellar alloy, which indicates that treating the transition in creep rate of the reinforcing phase as a step function is reasonable.

Substituting $\dot{u}_r = \dot{\epsilon}_m z$ for $z < z_c$ and $\dot{u}_r = \dot{\epsilon}_m z_c$ for $z > z_c$ into Eq. 9 results in the following:

$$\tau = 0 \quad (z < z_c) \quad [10a]$$

$$\tau = \beta' \sigma_{mo} \left(\frac{\dot{\epsilon}_m}{\dot{\epsilon}_{mo}} \right)^{1/m} \left(\frac{z - z_c}{d} \right)^{1/m} \quad (z > z_c). \quad [10b]$$

For $z > z_c$, a force balance allows the relationship between the shear and tensile stresses to be developed, as shown in Figure 9:

$$wt\delta\sigma_r = 2\tau(w + t)\delta z. \quad [11]$$

The width of the reinforcing lamellae is defined by the parameter w . If the factor $\delta\sigma_r$ for reinforcing lamellae ($w \gg t$) is compared with the corresponding expression for reinforcing fibers of diameter t [21], it can be shown that the tensile stresses developed in the lamellae are approximately a factor of two less than those developed in the fibers. The expressions given in Eq. 6 and Eq. 11 demonstrate that stress transfer to reinforcing lamellae is not as effective as stress transfer to reinforcing fibers [21]. This is a direct consequence of the greater surface to volume ratio associated with the fiber geometry.

Integrating σ_r for the case of τ given by Eq. 10b yields:

$$\sigma_r = -2 \int_{L/2}^z \tau \left(\frac{1}{t} + \frac{1}{w} \right) dz \quad [12]$$

$$= 2\beta' \frac{m}{m+1} \sigma_{mo} \left(\frac{\dot{\epsilon}_m}{\dot{\epsilon}_{mo}} \right)^{1/m} \left[1 + \frac{t}{w} \right] \left[\left(\frac{L'}{t} \right)^{(m+1)/m} - \left(\frac{z - z_c}{t} \right)^{(m+1)/m} \right]$$

where

$$\frac{L'}{t} = \frac{L}{2t} - \frac{z_c}{t}.$$

Evaluating Eq. 12 at $z = z_c$ yields the maximum value of σ_r , σ_r' , which represents the

tensile stress in the reinforcing lamellae for $z < z_c$:

$$\sigma_r' = 2\beta' \frac{m}{m+1} \sigma_{mo} \left(\frac{\dot{\epsilon}_m}{\dot{\epsilon}_{mo}} \right)^{1/m} \left(1 + \frac{t}{w} \right) \left(\frac{L'}{t} \right)^{(m+1)/m} \quad (z < z_c). \quad [13]$$

For $z > z_c$, σ_r monotonically decreases from its maximum value at $z = z_c$ to 0 at the reinforcing plate end. Therefore, the average value of σ_r in the interval z_c to $L/2$, σ_r'' , can be calculated by integrating the expression for σ_r given by Eq. 12:

$$\sigma_r'' = \int_{z_c}^{L/2} \left(\frac{L}{2} - z_c \right)^{-1} \sigma_r dz. \quad [14]$$

Evaluating this integral results in the following expression for σ_r'' :

$$\sigma_r'' = 2\beta' \frac{m}{2m+1} \sigma_{mo} \left(\frac{\dot{\epsilon}_m}{\dot{\epsilon}_{mo}} \right)^{1/m} \left(1 + \frac{t}{w} \right) \left(\frac{L'}{t} \right)^{(m+1)/m} \quad (z > z_c). \quad [15]$$

The aggregate average tensile stress on the entire reinforcing lamellae can be determined by combining Eq. 13 and Eq. 15 and taking into account the fraction of the lamellae length each stress acts on:

$$\bar{\sigma}_r = \frac{2z_c}{L} \sigma_r' + \frac{1-2z_c}{L} \sigma_r''. \quad [16]$$

The only parameter left to determine in this equation is z_c . As described previously, $\sigma_r = \sigma_r'$ at $z = z_c$. In an expression similar to Eq. 7, the creep rate of the reinforcing phase can be described by:

$$\sigma_r = \sigma_{ro} \left(\frac{\dot{\epsilon}_r}{\dot{\epsilon}_{ro}} \right)^{1/n}. \quad [17]$$

Combining Eq. 13 and Eq. 17 yields:

$$z_c = \left(\frac{L}{2} \right) - \phi t (\dot{\epsilon}_m^{1/n - 1/m})^{m/(m+1)} \quad [18]$$

where

$$\phi = \left(\frac{1}{2\beta'} \frac{m+1}{m} \frac{\sigma_{ro}}{\sigma_{mo}} \left(\frac{\dot{\epsilon}_{mo}}{\dot{\epsilon}_{ro}} \right)^{1/m} \frac{w}{w+t} \right)^{m/(m+1)}.$$

Thus, expanding Eq. 16 results in the final expression for the average tensile stress on the reinforcing plate.

Substituting the expression for the average tensile stress on the reinforcing plate into Eq. 3 results in a general constitutive relationship for the strength of a uniaxially aligned discontinuous lamellar composite:

$$\sigma_c = \sigma_{mo} \left(\frac{\dot{\epsilon}_m}{\dot{\epsilon}_{mo}} \right)^{1/m} \frac{2t}{L} \left(1 + \frac{t}{L} \right) \left[\phi 2^{1/m} \left(\frac{L'}{t} \right)^{(2m+1)/m} + 2\beta' \frac{m}{m+1} \left(\frac{L'}{t} \right)^{(m+1)/m} \left(\frac{L}{2t} - \frac{L'}{t} \right) \right] V_r + \sigma_{mo} \left(\frac{\dot{\epsilon}_m}{\dot{\epsilon}_{mo}} \right)^{1/m} (1 - V_r) \quad [19]$$

where

$$\phi = \left(\frac{2}{3} \right)^{1/m} \frac{m}{2m+1} \left(\frac{V_r}{1-V_r} \right)^{1/m}.$$

The composite strength, σ_c , is dependent on the matrix creep rate, $\dot{\epsilon}_m$, which is modified by the presence of the reinforcing phase. Therefore, σ_c represents the stress required to deform the composite at a creep rate given by $\dot{\epsilon}_m$. As in the original KS analyses, the length-to-thickness ratio of the reinforcing lamellae cannot be too small since load transfer to the lamellae by way of tensile stresses across their ends is assumed to be negligible.

5.2 Discontinuous lamellae oriented perpendicular to the uniaxial stress.

In a composite where the reinforcing lamellae are oriented perpendicular to the applied stress (Figure 7b), the composite creep rate is given by the isostress condition:

$$\dot{\epsilon}_c = \dot{\epsilon}_r V_r + \dot{\epsilon}_m V_m. \quad [20]$$

5.3 Discontinuous lamellae randomly oriented with respect to the uniaxial stress.

Since the two cases described in the previous two sections represent the upper and lower bounds of the composite creep strength, a composite possessing randomly oriented plates should exhibit a value of strength somewhere between these two limiting cases. McLean [25] has developed an analytical expression describing composite

creep for the general case of fiber orientation, but only elastically deforming fibers are considered. In this section, we show that the upper and lower bound stresses are similar for the particular case of the TiAl/Ti₃Al lamellar alloy, which obviates the need to find a solution for the general case.

The fiducial line results show that TiAl creeps more rapidly than Ti₃Al in the lamellar alloy. It is therefore appropriate to designate TiAl as the matrix phase and Ti₃Al as the reinforcing phase. The quantities $\dot{\epsilon}_m$ and $\dot{\epsilon}_r$ in the constitutive equations are equivalent to $\dot{\epsilon}_\gamma'$ and $\dot{\epsilon}_{\alpha_2}'$ defined in Eq. 2. The various geometric parameters required for the modified KS model were determined metallographically from samples of the lamellar alloy. The length of the Ti₃Al reinforcing plates was assumed to be equivalent to the average lamellar packet diameter of 70 μm . The average true thickness and volume fraction of the Ti₃Al reinforcing lamellae were measured to be 1.8 μm and 0.36 respectively [4]. The creep rate and values of stress exponent for the TiAl and Ti₃Al single-phase alloys were obtained from results published by Oikawa [14] and BYW, respectively.

Based on these experimentally determined values, the constitutive equations representing the upper and lower bound cases can be evaluated. Figure 10 is a graph of composite creep rate versus composite strength for the two cases. The modest difference in strength, for a fixed creep rate, between the matrix and reinforcing phases reflects a small difference in the upper and lower bounds of the composite strength. This would not necessarily be the case for typical metal matrix and polymer matrix composites where the strength of the reinforcing phase is significantly greater than that of the matrix phase [25, 26]. Given the small difference in upper and lower bound strengths of the lamellar composite, it is a reasonable approximation to take the average of these two values as representative of the strength of the TiAl/Ti₃Al composite possessing packets of plates aligned randomly with respect to the stress axis.

6. Results

The enhanced strain hardening factors described in Section 4 of this paper were experimentally determined for each constituent phase from creep tests conducted at 1080 K under an average applied stress of 380 MPa. The value of this factor for each phase is assumed to be constant for creep tests conducted at moderately different stresses and temperatures. The predictions of the modified KS model, with the

enhanced hardening of the constituent phases accounted for, at four different temperatures and a range of stresses, are plotted in Figure 11; also included are the experimentally determined creep rates for single-phase TiAl and Ti_3Al and the lamellar alloy [4, 14].

From the model results represented in Figure 11, the stress exponent and activation energy for creep of the lamellar alloy can be evaluated. In Table II, the average stress exponent and activation energy for creep in the lamellar alloy determined using the model are compared with the experimentally reported values [4]. Excellent agreement is obtained between the experimentally determined parameters and those obtained from the model.

7. Discussion of Model Results

At 980 K, 1030 K and 1080 K, the agreement between the model predictions and the experimentally determined creep rates for the lamellar alloy is very good. At 1130 K, the predicted creep rates of the lamellar alloy are a little lower than the experimentally determined creep rates. This comparison demonstrates that the creep behavior of the lamellar alloy can be represented by a constitutive equation based on composite strengthening mechanisms. The applicability of composite strengthening concepts was not initially apparent because the enhanced hardening of the constituent phases is not present when they are tested as single-phase alloys.

The observation that a single value of the hardening factor for each phase adequately explains the observed behavior over moderate temperature and stress ranges suggests that the mechanisms responsible for enhanced strain hardening in the lamellar alloy are insensitive to the conditions of the creep test. At 1130 K, the model predicts that the creep rates of the lamellar alloy are approximately a factor of two lower than the experimentally determined rates. Fiducial line experiments could be conducted for lamellar samples crept at 1130 K to determine if the strain hardening factors are indeed lower at this temperature. If the strain hardening factors are lower at 1130 K, it would not be immediately apparent whether this is due to a lower work hardening rate or to a higher recovery rate. In this context, it is important to consider that the strain hardening factor encompasses both the work hardening and recovery phenomena. As discussed previously, the work hardening effect in the lamellar alloy can be attributed to an increase in dislocation source density at the interphase interface, and to

considerations of interstitial impurity segregation. It is reasonable to consider that the effect of the interfaces on dislocation generation is less temperature dependent than recovery processes. Therefore, a decrease in the strain hardening factor at 1130 K most likely reflects an increase in the recovery rate of the constituent phases in the lamellar alloy.

In addition to effects of the recovery rate on the strain hardening factor, several other factors could contribute to the discrepancy between the model and the experimental results at 1130 K. For example, thermal effects at the interface may be sufficient to promote interfacial sliding at 1130 K. The resulting inefficiency of stress transfer to the reinforcing phase would result in a higher creep rate of the composite.

Rao and Tangri [27] reported that the work hardening rate of two-phase TiAl/Ti₃Al lamellar alloys was greater than the work hardening rates of single-phase TiAl and Ti₃Al. Evaluation of their data revealed that the work hardening rate was approximately an order of magnitude greater than those of the constituent phase alloys. This result is in excellent agreement with the values of strain hardening factor determined from the fiducial line experiments in the present investigation, even though the stoichiometry of the TiAl alloy tested by Rao and Tangri was different from that of the TiAl alloy used in the present investigation. Additionally, Rao and Tangri conducted constant strain rate tests, as opposed to the constant stress creep tests of the current investigation. These differences do not detract from the agreement in experimental results between the two investigations.

In the present study, the difference in creep response of TiAl and Ti₃Al tested as single-phase alloys and tested in the lamellar microstructure was only quantified in terms of the strain hardening factor. Any differences in activation energy for creep between the constituent phases in the lamellar microstructure and the corresponding single-phase alloys were not taken into account. It was assumed that the values of activation energy for creep of the phases were not significantly affected in the lamellar microstructure. This assumption appears justified when comparing the predicted and experimentally determined activation energies for the lamellar alloy listed in Table II.

8. Conclusions

- (1) During the creep deformation of the two-phase TiAl/Ti₃Al lamellar alloy investigated in this study, the TiAl phase within the lamellar microstructure was observed to creep at a higher rate than the Ti₃Al phase within the lamellar microstructure.
- (2) For true strains up to 0.08 at 1080 K, interfacial sliding was undetectable in the lamellar alloy crept in compression.
- (3) The creep rates of the constituent TiAl and Ti₃Al phases within the lamellar microstructure tested in compression are approximately a factor of twenty and twenty five, respectively, lower than the creep rates of single-phase TiAl and Ti₃Al tested in compression at the same stress and temperature.
- (4) With the enhanced hardening of the constituent phases within the lamellar microstructure accounted for, the creep rate of the lamellar alloy can be represented by a constitutive equation based on composite creep strengthening mechanisms. Application of the constitutive equation yields a very good correlation between predicted and experimentally observed minimum creep rates over moderate temperature and stress ranges. Values of stress exponent and activation energy for creep of the lamellar alloy calculated from the model agree well with the experimentally determined values.

9. Acknowledgements

We would like to express our gratitude to colleagues who have assisted with various aspects of this work: Mr. D. Gundel for helping with the vacuum hot press experiments; Mr. S. Yu for his help and advice concerning the fiducial line experiment; Mr. M. Cantrell for his assistance on the TEM; and Ms. S. Zambo for conducting some of the metallographic measurements. We would also like to acknowledge Prof. E.F. Bartholomeusz, Ms. F. Smith, Prof. T. Kozmac and Prof. T. Courtney for their thoughtful and insightful discussions. This work was sponsored by AOFSR under contract number AOFSR-90-0143; Dr. A. Rosenstein was the contract monitor.

10. References

1. Y.W. Kim and D.M. Dimiduk, JOM, 43 no. 8 (1991) 40.
2. H.A. Lipsitt, D. Shechtman and R.E. Schafrik, Metall. Trans., 11A (1980) 1369.
3. S. Mitao, S. Tsuyama and K. Minakawa, Mater. Sci. Eng., A143 (1991) 40.
4. M.F. Bartholomeusz, Q. Yang and J.A. Wert, "Creep Deformation of a Two-Phase TiAl/Ti₃Al Lamellar Alloy and the Individual TiAl and Ti₃Al Constituent Phases," accepted for publication in Scripta Metall. Mater. (1993).
5. R.S. Polvani, W.-S. Tzeng and P.R. Strutt, Metall. Trans., 7A (1976) 33.
6. P.R. Strutt and B.H. Kear in *High-Temperature Ordered Intermetallic Alloys*, edited by C.C. Koch, C.T. Liu and N.S. Stoloff (MRS, Pittsburgh, PA, 1985), 279.
7. M.V. Nathal, J.O. Diaz and R.V. Miner in *High-Temperature Ordered Intermetallic Alloys III*, edited by C.T. Liu, A.I. Taub, N.S. Stoloff and C.C. Koch (MRS, Pittsburgh, PA, 1985), 269.
8. D. McLean, Progress in Physics, 29 (1966) 1.
9. J.P. Poirier, *Creep of Crystals*, (Cambridge University Press, 1985), p. 108.
10. J.H. Van Der Merwe, G.J. Shiflet and P.M. Stoop, Metall. Trans., 22A (1991) 1165.
11. V.K. Vasudevan, M.A. Stucke, S.A. Court and H.L. Fraser, Philos. Mag. Lett., 59 (1989) 299.
12. S.A. Court, J.P.A. Lofvander, M.H. Loretto and H.L. Fraser, Philos. Mag., 61 (1990) 109.
13. J. Weertman, Trans. A.S.M., 61 (1968) 681.
14. H. Oikawa, in *High Temperature Aluminides & Intermetallics*, edited by S.H. Wang, C.T. Liu, D.P. Pope and J.O. Stiegler (TMS, Warrendale, PA, 1989), 353.
15. T. Takahashi, H. Nagai and H. Oikawa, Mater. Sci. Eng., A128 (1990) 195.
16. M.G. Mendiratta and H.A. Lipsitt, J. Mater. Sci., 15 (1980) 2985.

17. H. Nagai, T. Takahashi and H. Oikawa, J. Mater. Sci., 25 (1990) 629.
18. S.C. Huang and D.S. Shih, in *Microstructure/Property Relationships in Titanium Aluminides and Alloys*, edited by Y.W. Kim and R.R. Boyer (TMS, Warrendale, PA, 1990), 105.
19. L.M. Brown and R.K. Ham, in *Strengthening Methods in Crystals*, edited by A. Kelly and R.B. Nicholson (Wiley, New York, 1971), 12.
20. M. McLean, Acta Metall. Mater., 33 (1985) 545.
21. A. Kelly and K.N. Street, Proc. Roy. Soc. Lond., A328 (1972) 283.
22. A. Kelly and W.R. Tyson, J. Mech. Phys. Solids, 14 (1966) 177.
23. I. Miura and H. Honma, J. Jap. Inst. Met., 31 (1967) 607.
24. A. Kelly and K.N. Street, Proc. Roy. Soc. Lond., A328 (1972) 267.
25. M. McLean, in *Proc. 5th Int. Conf. on Composite Materials*, edited by W.C. Harrigan, J. Strife and A.K. Dhingra (TMS, Warrendale, PA, 1985), 37.
26. A.F. Johnson, Mech. Phys. Solids, 25 (1977) 117.
27. P.P. Rao and Kris Tangri, Mater. Sci. Eng., A132 (1991) 49.

Table I

Creep rates of lamellar alloy and constituent phases determined from compression creep tests and fiducial line experiments at 1080 K under an applied stress of 380 MPa.

Material	$\dot{\epsilon}$ [creep tests] (1/s)	$\dot{\epsilon}$ [fiducial line results] (1/s)
lamellar alloy	1.8×10^{-6}	2.2×10^{-6}
TiAl *	6.2×10^{-5}	3.0×10^{-6}
Ti ₃ Al	2×10^{-5}	8.0×10^{-7}

* Creep data for fine-grain TiAl obtained from Ref. [14]. Creep data for Ti₃Al and lamellar alloy obtained from Ref. [4].

Table II

Comparison between experimentally determined values of activation energy for creep and stress exponent in the lamellar alloy with model predictions.

Material	Q (kJ/mol)	n
Lamellar alloy [expt.]	407	5.4
Lamellar alloy [model]	415	6.2

List of Figures

Figure 1. Optical micrograph of undeformed lamellar microstructure. The dark lamellae are the TiAl phase and the light lamellae are the Ti_3Al phase.

Figure 2. Minimum creep rates as a function of stress for the lamellar alloy and the constituent single phase alloys tested at 1080 K by BYW [4].

Figure 3. SEM micrographs of fiducial lines on a surface of the lamellar alloy. (a) Prior to compression creep testing. (b) After compression creep testing at 1080 K under an applied compressive stress of 350 MPa to a true strain of 0.044. The darker phase is the TiAl phase. Its mottled appearance is an artifact of the etching process.

Figure 4. (a) SEM micrographs of fiducial lines on a surface of the lamellar alloy prior to compression creep testing. (b) Region "a" in micrograph (a) after compression creep testing at 1080 K under an applied compressive stress of 380 MPa to a true strain of 0.078. The arrows indicate the compression axis. The heavy dark line represents the orientation of the fiducial line prior to compression creep testing.

Figure 5. (a) Minimum creep rates as a function of stress for TiAl [14], Ti_3Al [4] and the lamellar alloy [4] at 1080 K in the absence of the enhanced hardening effect. (b) Same creep curves as represented in (a) with the enhanced hardening of the constituent phases within the lamellar microstructure accounted for.

Figure 6. TEM micrograph of lamellar sample deformed in compression at 1130 K to a true strain of 0.087.

Figure 7. (a) represents the velocity of the different phases and the interface in the case where the plates are aligned parallel to the applied stress (z axis). (b) represents the velocity of the different phases when the plates are aligned perpendicular to the applied stress.

Figure 8. Creep rate of a reinforcing lamellar plate as a function of position on the plate. The plate is being viewed edge on.

Figure 9. For a small increment in the length of a reinforcing lamellar, δz , the increase in plate stress is obtained by the force balance: $w t \delta \sigma_r = 2 \tau w \delta z + 2 \tau t \delta z$.

Figure 10. Model results of minimum creep rate as a function of stress at 1080 K when the reinforcing lamellae are aligned perpendicular and parallel to the applied stress.

Figure 11. Model predictions compared with the experimentally determined compressive creep rates for the lamellar alloy [4] and the two constituent single phase alloys, TiAl [14] and Ti_3Al [4] at: (a) 980 K. (b) 1030 K. (c) 1080 K. (d) 1130 K.



Figure 1. Optical micrograph of undeformed lamellar microstructure. The dark lamellae are the TiAl phase and the light lamellae are the Ti₃Al phase.

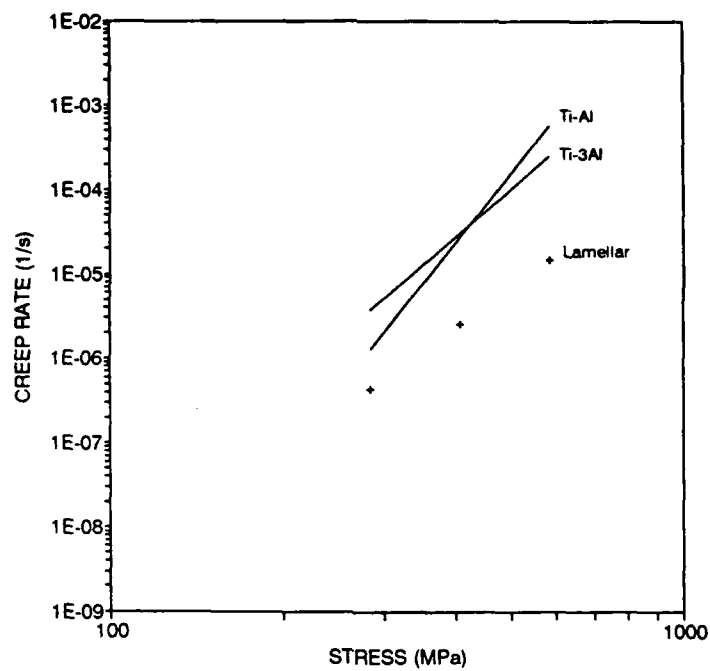
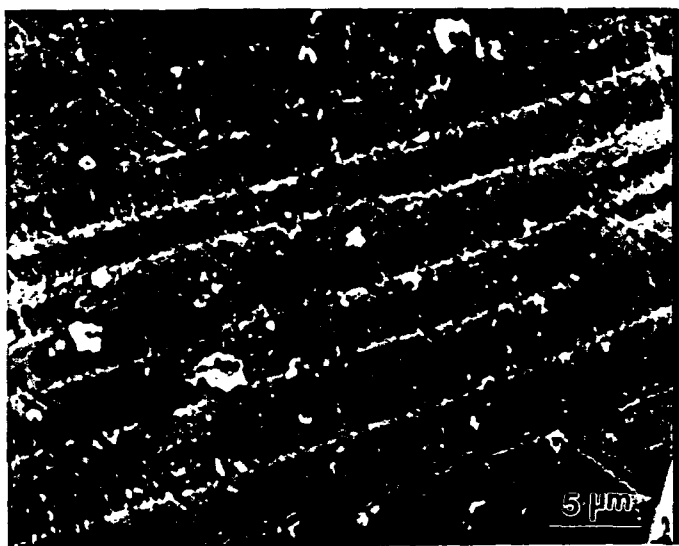
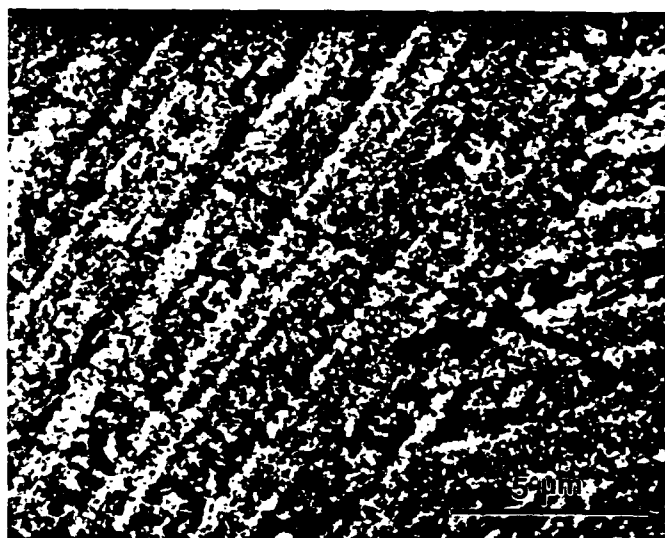


Figure 2. Minimum creep rates as a function of stress for the lamellar alloy and the constituent single phase alloys tested at 1080 K by BYW [4].



(a)

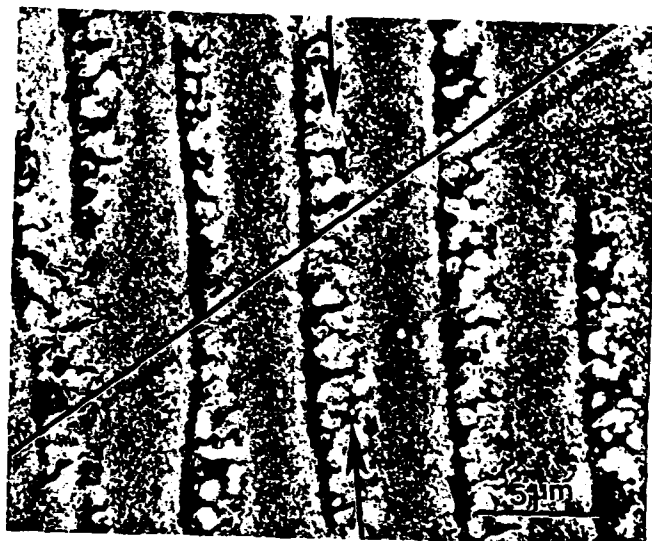


(b)

Figure 3. SEM micrographs of fiducial lines on a surface of the lamellar alloy. (a) Prior to compression creep testing. (b) After compression creep testing at 1080 K under an applied compressive stress of 350 MPa to a true strain of 0.044. The darker phase is the TiAl phase. Its mottled appearance is an artifact of the etching process.

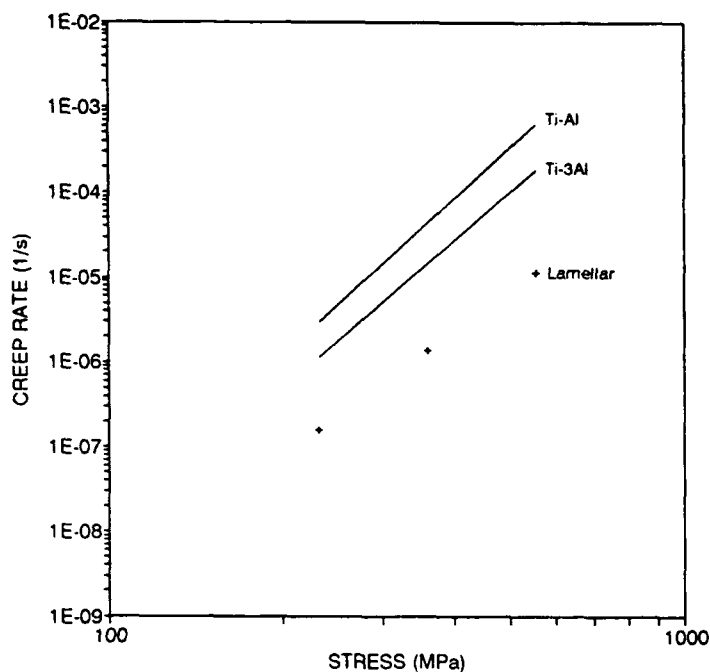


(a)

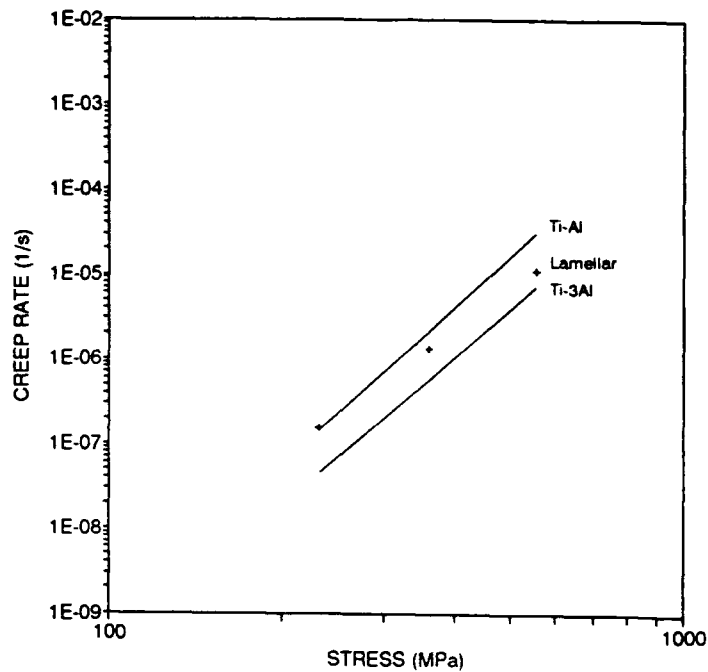


(b)

Figure 4. (a) SEM micrographs of fiducial lines on a surface of the lamellar alloy prior to compression creep testing. (b) Region "a" in micrograph (a) after compression creep testing at 1080 K under an applied compressive stress of 380 MPa to a true strain of 0.078. The arrows indicate the compression axis. The heavy dark line represents the orientation of the fiducial line prior to compression creep testing.



(a)

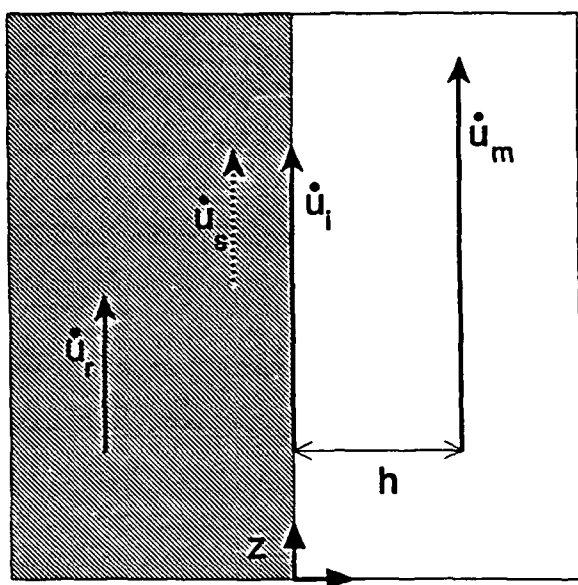


(b)

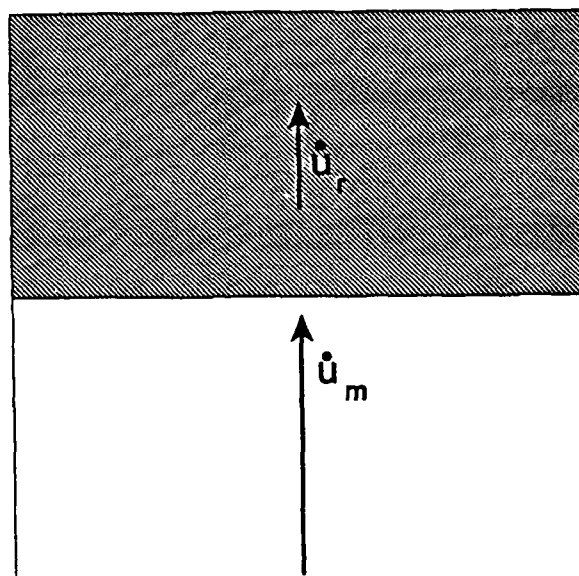
Figure 5. (a) Minimum creep rates as a function of stress for TiAl [14], Ti_3Al [4] and the lamellar alloy [4] at 1080 K in the absence of the enhanced hardening effect. (b) Same creep curves as represented in (a) with the enhanced hardening of the constituent phases within the lamellar microstructure accounted for.



Figure 6. TEM micrograph of lamellar sample deformed in compression at 1130 K to a true strain of 0.087.



(a)



(b)

Figure 7. (a) represents the velocity of the different phases and the interface in the case where the plates are aligned parallel to the applied stress (z axis). (b) represents the velocity of the different phases when the plates are aligned perpendicular to the applied stress.

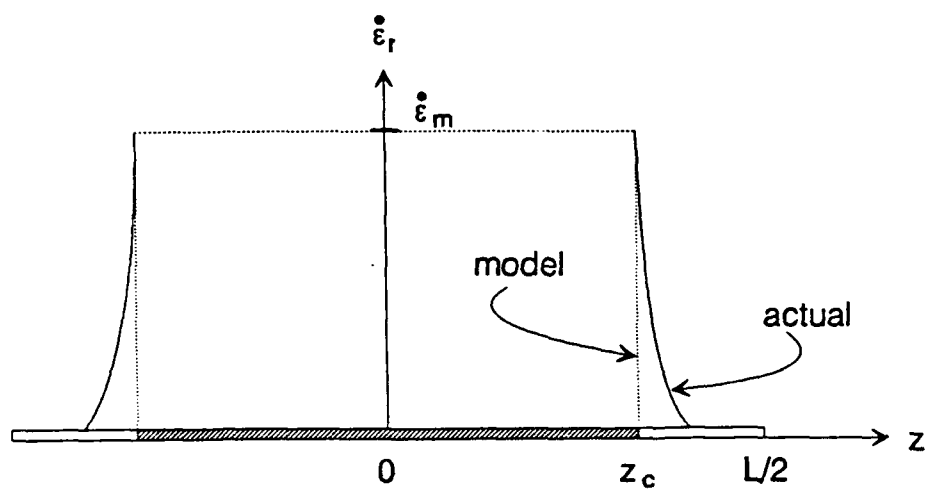


Figure 8. Creep rate of a reinforcing lamellar plate as a function of position on the plate. The plate is being viewed edge on.

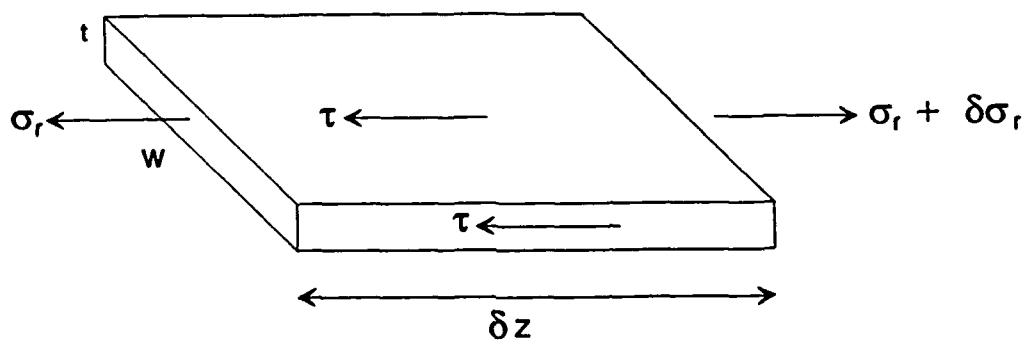


Figure 9. For a small increment in the length of a reinforcing lamellar, δz , the increase in plate stress is obtained by the force balance: $w t \delta \sigma_r = 2 \tau w \delta z + 2 \tau t \delta z$.

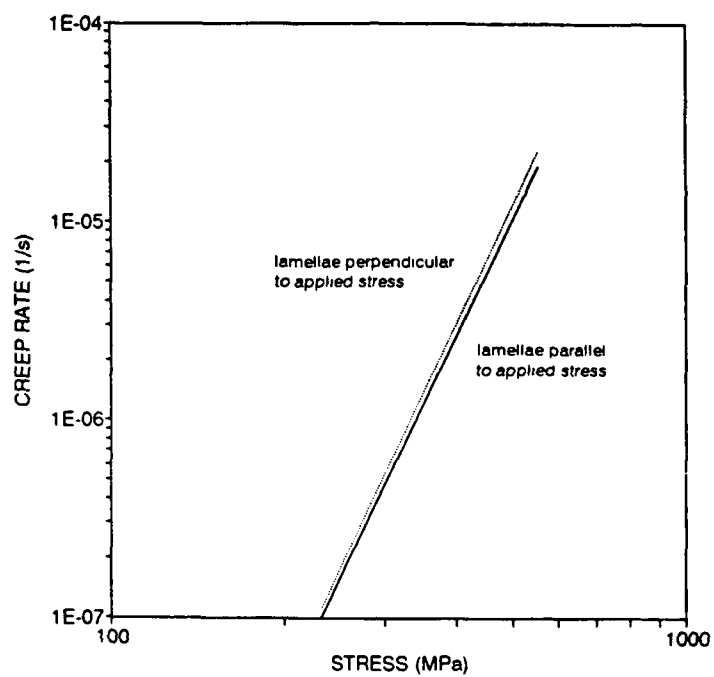
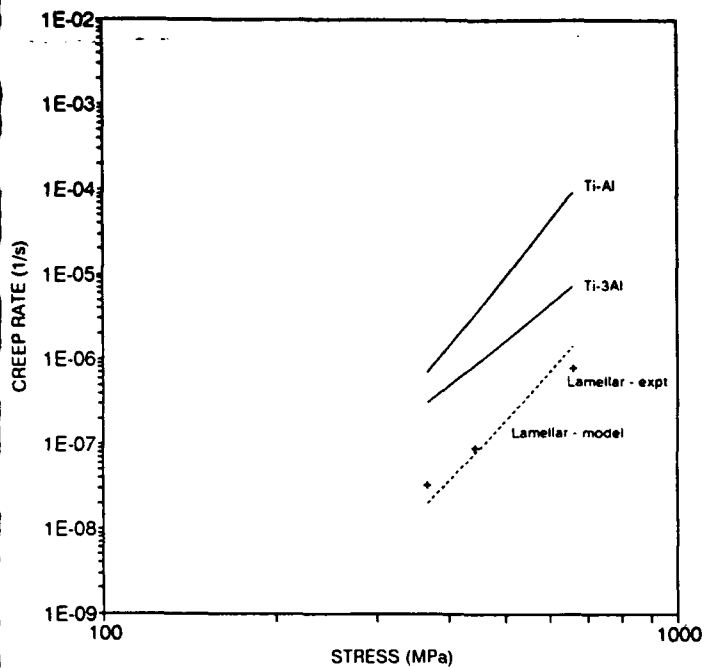
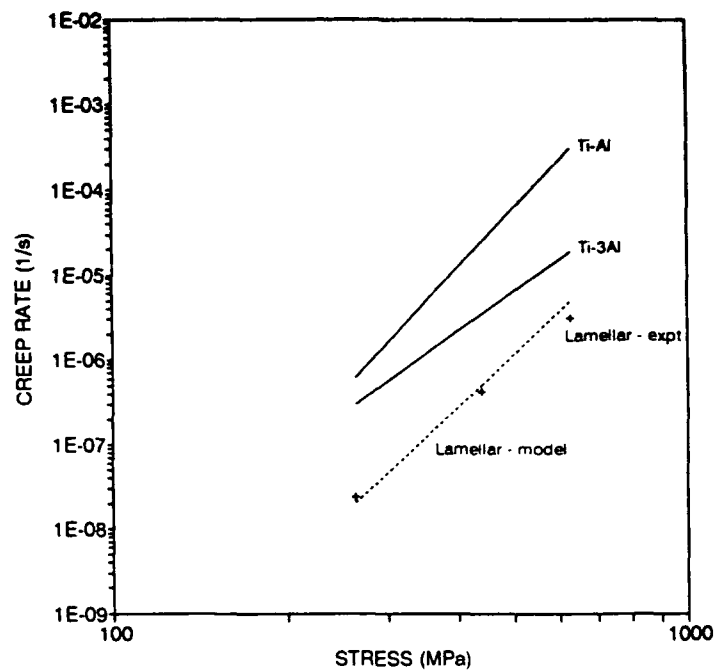


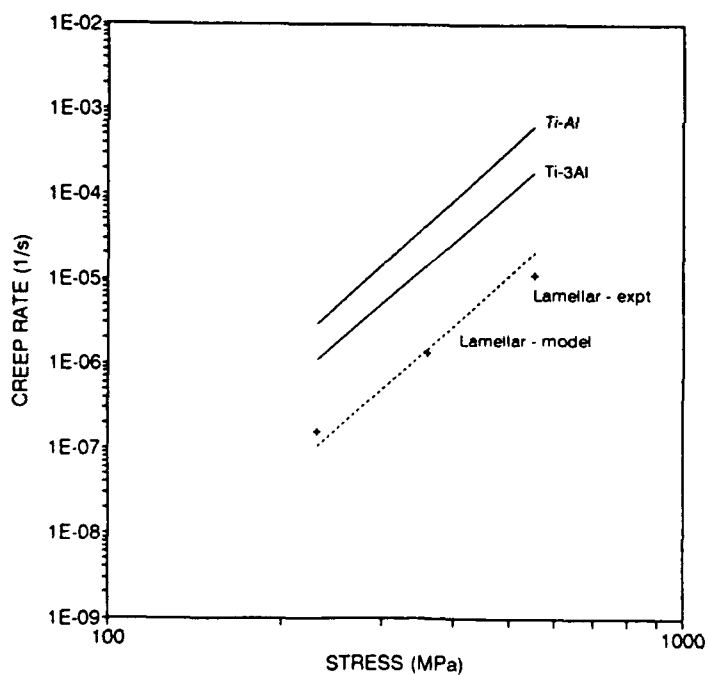
Figure 10. Model results of minimum creep rate as a function of stress at 1080 K when the reinforcing lamellae are aligned perpendicular and parallel to the applied stress.



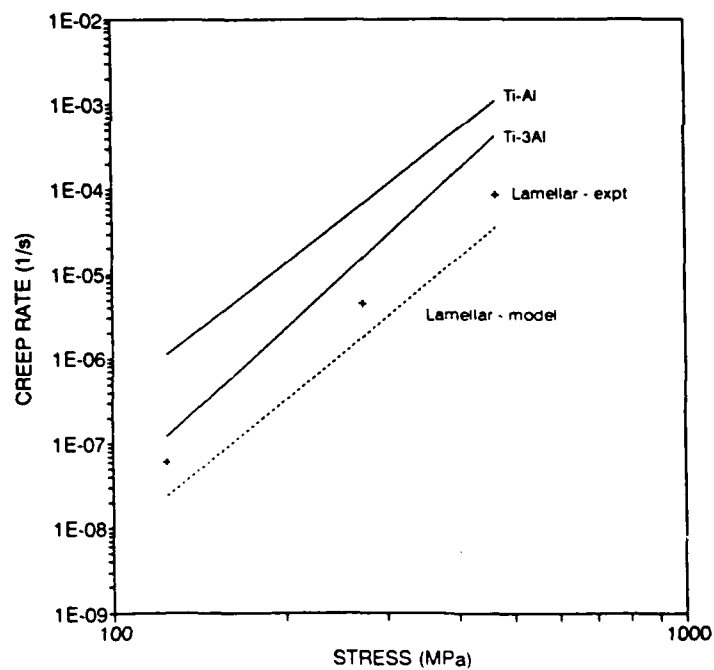
(a)



(b)



(c)



(d)

Figure 11. Model predictions compared with the experimentally determined compressive creep rates for the lamellar alloy [4] and the two constituent single phase alloys, TiAl [14] and Ti_3Al [4] at: (a) 980 K. (b) 1030 K. (c) 1080 K. (d) 1130 K.

4. Publications and Presentations

Publications

M.F. Bartholomeusz and J.A. Wert, "Effect of Dislocation Dissociation on Crack Tip Plasticity in $L1_2$ Intermetallic Alloys", *Acta Metallurgica et Materialia*, Vol. 40, 1992, pp. 673-682.

M.F. Bartholomeusz and J.A. Wert, "Modeling of Crack Tip Dislocation Emission in B2 Intermetallic Alloys", *Journal of Materials Research*, Vol. 7, 1992, pp. 919-925.

M.F. Bartholomeusz, W.G. Meng and J.A. Wert, "The Effect of Dislocation Dissociation on Crack Tip Plasticity in $L1_2$ and B2 Intermetallic Alloys", in *High-Temperature Ordered Intermetallic Alloys V*, MRS, Pittsburgh, 1993, pp. 537-542.

M.F. Bartholomeusz, Q. Yang and J.A. Wert, "Creep Deformation of a Two-Phase TiAl/Ti₃Al Lamellar Alloy and the Individual TiAl and Ti₃Al Constituent Phases", accepted for publication in *Scripta Metallurgica et Materialia*, 1993.

J.A. Wert, "Ordered Intermetallic Alloys for Elevated Temperature Applications", accepted for publication in *Monograph on Flight Vehicle Materials, Structures and Dynamics Technologies - Assessment and Future Directions*, 1993.

M.F. Bartholomeusz and J.A. Wert, "Modeling Creep Deformation of a Two-Phase TiAl/Ti₃Al Alloy with a Lamellar Microstructure", submitted to *Acta Metallurgica et Materialia*, 1993.

W.G. Meng, M.D. Vaudin, M.F. Bartholomeusz and J.A. Wert, "Experimental Assessment of Crack Tip Dislocation Emission Models for an Al₆₇Cr₈Ti₂₅ Intermetallic Alloy", submitted to *Metallurgical Transactions A*, 1993.

M.F. Bartholomeusz and J.A. Wert, "Microstructural Evolution in TiAl/Ti₃Al Alloys During Creep and Annealing", in preparation.

Presentations

W.O. Powers and J.A. Wert, "Characterization of (100) Faults in $\text{Al}_{67}\text{Ni}_8\text{Ti}_{25}$ " TMS Fall Meeting, Indianapolis, October 3, 1989.

J.A. Wert, "Overview of Microstructure, Deformation and Fracture Characteristics of $(\text{Al},\text{X})_3\text{Ti}$ Intermetallic Alloys", TMS Fall Meeting, Indianapolis, October 4, 1989.

J.A. Wert, "Microstructure, Deformation and Fracture of $\text{Al}_{67}\text{Ni}_8\text{Ti}_{25}$ and Related $(\text{Al},\text{X})_3\text{Ti}$ Intermetallic Alloys", General Dynamics, Fort Worth, Aug. 22, 1990.

M.F. Bartholomeusz and J.A. Wert, "Effect of Dislocation Dissociation on Crack Tip Plasticity in L1_2 Ordered Intermetallic Alloys", TMS Annual Meeting, New Orleans, February 20, 1991

M.F. Bartholomeusz, W.G. Meng and J.A. Wert, "The Effect of Dislocation Dissociation on Crack Tip Plasticity in L1_2 and B2 Intermetallic Alloys", MRS Meeting, Boston, December 1, 1992.

DISTRIBUTION LIST

1 - 6

Air Force Office of Scientific Research
Building 410
Bolling Air Force Base
Washington, DC 20332

Attention: Dr. Alan H. Rosenstein/NE
Directorate of Chemistry and Materials Science

7 - 8

E. H. Pancake, Clark Hall

9

J. A. Wert

10

W. A. Jesser

*

SEAS Postaward Research Administration

11

SEAS Preaward Research Administration

*Cover Letter

JO#5154:ph